Aeroradiometric Measurements in the Framework of the Swiss Exercise ARM22

Gernot Butterweck, Alberto Stabilini, Benno Bucher, David Breitenmoser,
Ladislaus Rybach, Cristina Poretti, Stéphane Maillard, Adrian Hess,
Malgorzata Kasprzak, Gerald Scharding, Sabine Mayer

PSI Bericht Nr. 23-01
March 2023
ISSN 1019-0643

DOI: https://doi.org/10.55402/psi:51194

Aeroradiometric Measurements in the Framework of the Swiss Exercise ARM22

Gernot Butterweck[1], Alberto Stabilini[1], Benno Bucher[2], David Breitenmoser[1],
Ladislaus Rybach[3], Cristina Poretti[4], Stéphane Maillard[5], Adrian Hess[4],
Malgorzata Kasprzak[1], Gerald Scharding[4], Sabine Mayer[1]

1 Department of Radiation Safety and Security, Logistics Division, Paul Scherrer Institute (PSI), Forschungsstrasse 111, 5232 Villigen PSI, Switzerland
2 Swiss Federal Nuclear Safety Inspectorate (ENSI), Industriestrasse 19, 5201 Brugg, Switzerland
3 Institute of Geophysics, Swiss Federal Institute of Technology Zürich (ETHZ), 8092 Zürich, Switzerland
4 Swiss National Emergency Operations Center (NEOC), 3003 Bern, Switzerland
5 NBC-EOD Centre of Competence (Nuclear Biological Chemical Defense and Explosive Ordnance Disposal), 3700 Spiez, Switzerland

Paul Scherrer Institut (PSI)
5232 Villigen PSI, Switzerland
Tel. +41 56 310 21 11
Fax +41 56 310 21 99
www.psi.ch

PSI Bericht Nr. 23-01
March 2023
ISSN 1019-0643

Abstract

The flights of the civil (ARM22c) and military (ARM22m) parts of the exercise were performed between June 13th and 17th and between September 5th and September 9th, respectively.

Both parts of the exercise included the measurement of altitude profiles. Two profiles were measured during ARM22c over Lake Thun and one profile during ARM22m over Lake Neuchâtel with sufficient altitude range to determine the slope of the altitude-dependent cosmic correction. The altitude profile over Lake Neuchâtel showed a clear deviation from the expected profile, suggesting a massive influence of airborne radon progeny on the result.

According to the alternating schedule of the annual ARM exercises, the environs of the nuclear power plants Beznau (KKB) and Leibstadt (KKL), the Paul Scherrer Institute (PSI) and the intermediate storage facility (ZWILAG) were surveyed with an extension of the measuring area into German territory, following a request of German authorities. The site of the former Lucens reactor was measured and found unobtrusive in the measured data.

Background flights were performed over several Swiss cities, regions and valleys. Besides attenuation effects of water bodies, variations of natural radionuclide content could be observed. Remains of the Chernobyl deposition were detected near the French border and in southern Switzerland.

Contents

List of Figures

List of Tables

1 Introduction

Swiss airborne gamma spectrometry measurements started in 1986. The methodology and software for calibration, data acquisition and mapping were developed at the Institute of Geophysics of the Swiss Federal Institute of Technology Zurich (ETHZ). Between 1989 and 1993 the environs of Swiss nuclear installations were measured annually on behalf of the Swiss Federal Nuclear Safety Inspectorate (ENSI) during exercises performed as system check and drill for the operators. This schedule was changed to biennial inspections in 1994, together with an organizational inclusion of the airborne gamma-spectrometric system (ARM) into the Emergency Organization Radioactivity (EOR) of the Federal Office for Civil Protection (FOCP). The deployment of the airborne gamma-spectrometric system is organized by the National Emergency Operations Centre (NEOC). NEOC is also responsible for the recruitment and instruction of the measurement team and for the operational readiness of the system. Aerial operations are coordinated and performed by the Swiss Air Force with Super Puma helicopters. Identical gamma-spectrometric pieces of equipment are stationed at the military airfields of Dübendorf and Payerne and can be fully operative and airborne within four hours. Responsibility for scientific support, development and maintenance of the aeroradiometric measurement equipment passed from ETHZ to the Radiation Metrology Section of the Paul Scherrer Institute (PSI) in 2003, in cooperation with ENSI. General scientific coordination and planning of the annual measuring flights is provided by the Expert Group for Aeroradiometrics (FAR) which consists of experts from all Swiss institutions concerned with aeroradiometry. FAR, formerly a working group of the Swiss Federal Commission for NBC protection (ComNBC), was re-organized as an expert group of NEOC in 2008. Additional information can be found at `https://far.ensi.ch/`.

In 2018 the ARM measuring system used by NEOC in past exercises was replaced with the RLL (Radiometrie Land-Luft) system owned by the Swiss armed forces. The maintenance of the RLL systems is performed by the manufacturer according to a service agreement with the Swiss armed forces. Of the four systems available, under normal circumstances two systems are operated by staff of the NBC-EOD Centre of Competence (NBC-EOD) for measurement tasks with military character and two systems are assigned to NEOC for the deployment in case of civil emergencies with a radiological component. Since 2018, the scientific report includes, in addition to the measuring flights of NEOC (ARM22c), flights performed by NBC-EOD (ARM22m).

This report focuses on methodological aspects and thus complements the respective short reports available at `https://www.naz.ch` (ARM22c) and `https://www.vtg.admin.ch/de/organisation/kdo-ausb/lvb-g-rttg-abc/komp-zen-abc-kamir.html` (ARM22m).

1.1 Measuring system RLL

The measuring system RLL (Radiometrie Land-Luft) used both for civil and military measurements consists of a radiation detector featuring four NaI(Tl) scintillation crystals having a total volume of 16.8 litres with their associated photo-multipliers and multichannel analysers (MCA) for low level measurements, and one Geiger-Müller tube and associated electronics for high dose-rate measurements. The spectroscopic measuring chain provides a linear energy calibration of the MCA up to 3 MeV divided into 1024 channels. NaI detectors, Geiger-Müller tube and associated electronics are installed in an aluminium case with thermal insulation foam. The detection container is mounted in the cargo bay below the centre of the helicopter. The RLL system uses position, air pressure, air temperature and radar altitude data provided by the helicopter via the internal ARINC bus. Figure 1 shows the complete system packaged for storage. The equipment control, data acquisition and storage are performed with a rugged computer working as a data server. Two further rugged redundant client computers are used as operator interface for real-time evaluation, data mapping and communication. All computers are installed in an equipment rack including a battery backed-up power supply. Both operators can operate the system with their associated client computer, display, keyboard and trackball. The additional third central display of the operator's console is mirrored on a screen in the cockpit located between both pilots and is used for information exchange with the pilots and general radiological situation awareness (Figure 2). The measuring system RLL is mounted in an Aerospatiale AS 332 Super Puma helicopter (TH 06) of the Swiss Air Forces (Figure 3). This helicopter has excellent navigation properties and allows emergency operations during bad weather conditions and night time.

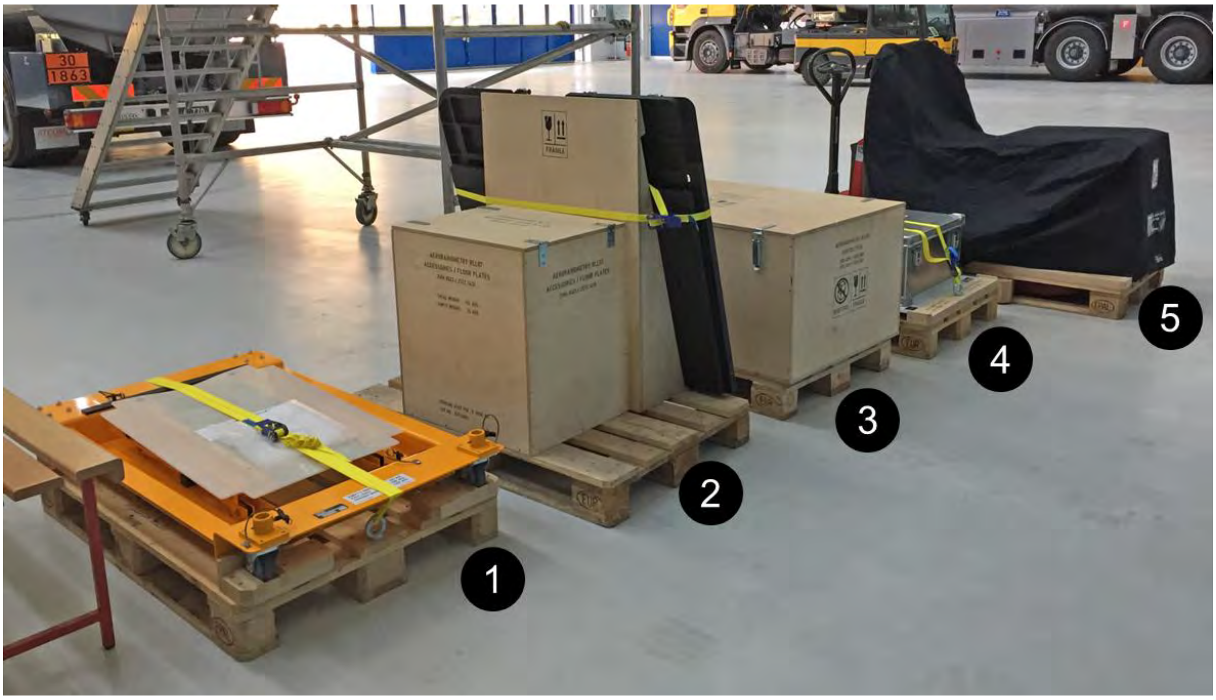

Figure 1: Components of the RLL system. 1. Lifting platform for the installation of the detection container. 2. Floor plates and accessories case. 3. Monitors and operator console. 4. Detection container. 5. Operator seats and equipment rack.

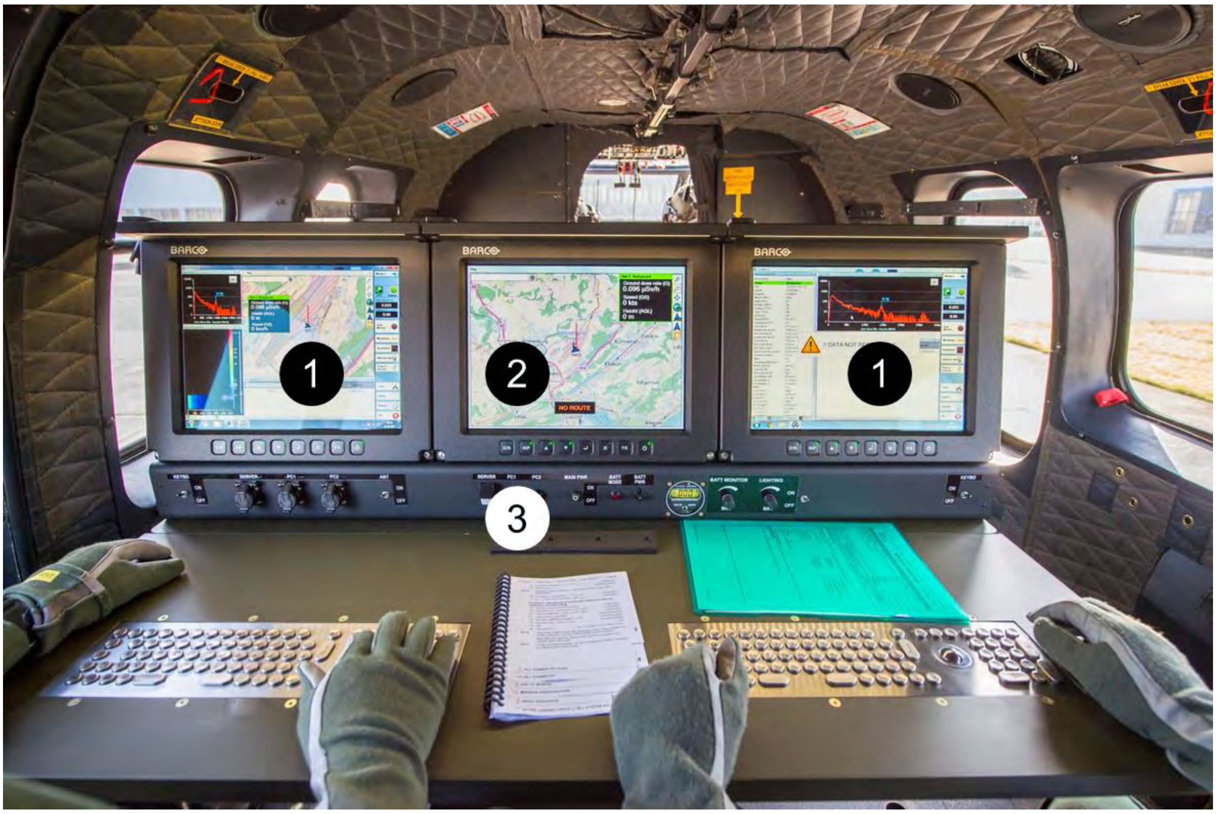

Figure 2: Operator console of the RLL system. 1. Displays of the client computers. 2. Common display (mirrored in the cockpit). 3. Control panel with switches for power, lighting and communication and USB ports for file exchange.

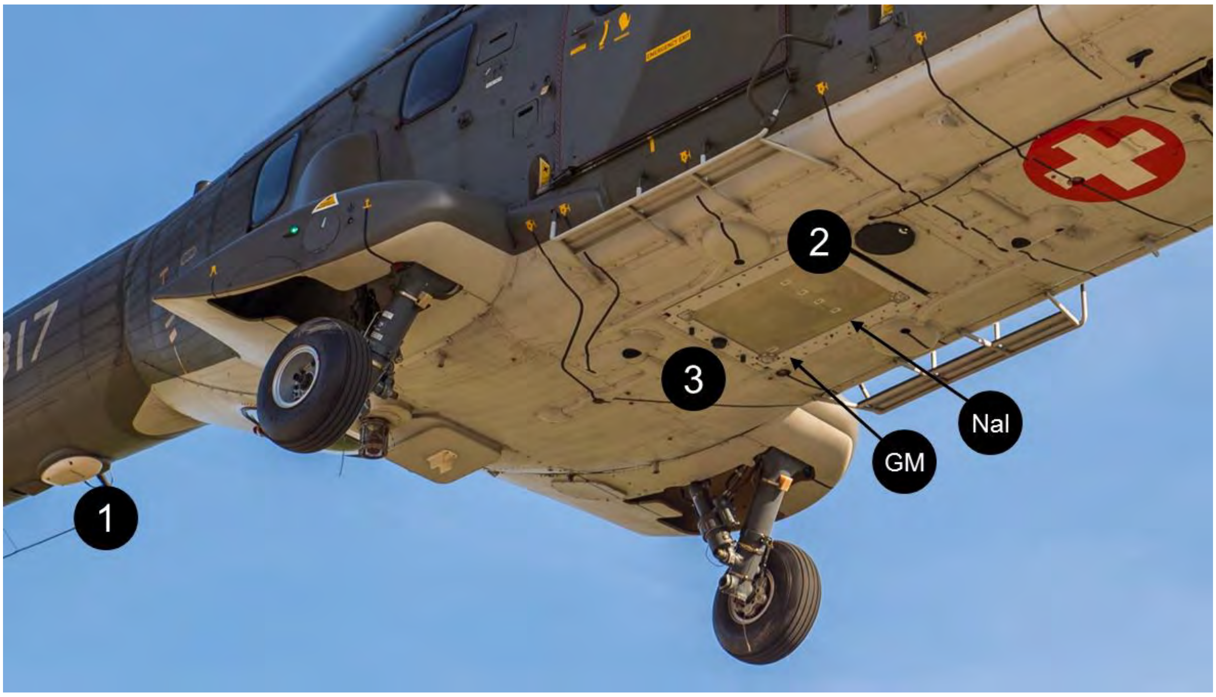

Figure 3: RLL detector mounted in the cargo bay of a Super Puma helicopter. 1. Radar altimeter. 2. Detection container marked with detector reference points. 3. UMTS antenna for data upload.

1.2 Measuring flights

The advantage of aeroradiometric measurements lies in the high velocity of measurements in a large area, even over rough terrain. Uniform radiological information of an area is obtained from a regular grid of measuring points. This grid is composed from parallel flight lines which are 100 m to 1000 m apart, depending on the scope of the measurement. The flight altitude above ground is aspired to be constant during the measuring flight. Typical values lie between 50 m and 150 m above ground. The spectra are recorded in regular time intervals of typically one second, yielding an integration over 28 m of the flight line considering a speed of 100 km/h.

1.3 Data evaluation

The proprietary software for data acquisition and evaluation provided by the manufacturer of the RLL system was tested sufficient for supplying data to support decisions in radiological emergencies. An outline of the algorithms used can be found in Butterweck et al. (2018). An additional off-line data evaluation software (named AGS_CH) following the methodology developed at ETHZ described in Schwarz (1991) and Bucher (2001) is used to produce the results presented throughout the PSI reports since 2020. The measured spectra are evaluated using energy windows for relevant radionuclides and the spectrum dose index (SDI) to determine dose rates.

1.3.1 Background and cosmic correction

The civil part of the exercise (ARM22c) included two altitude profiles over Lake Thun in the morning and afternoon of June 16^{th}. An altitude profile over Lake Neuchâtel was measured during the military part (ARM22m) of the exercise. Figures 4 and 5 show the altitude above sea level along the respective flight paths. All altitude profiles, spanning more than 2000 m between lowest and highest altitude, were used to determine the slope of the cosmic correction using Deming regression with δ limited to values above 1 (Table 1) as described in Butterweck et al. (2021).

Although the slopes derived over Lake Thun are consistent with former measurements, the slopes for the Uranium and Caesium energy windows derived from measurements over Lake Neuchâtel have unexpectedly negative values of -0.02 and -1.7 (Figure 6). Both energy windows are influenced by emissions of the radon decay product ^{214}Bi with energies of 1765 keV and 609 keV, respectively. This leads to the conclusion that the altitude profile over Lake Neuchâtel was massively disturbed by photon emissions of airborne radon progeny. To test this hypothesis, the count rate in the energy window between 100 keV and 400 keV is plotted as function of the altitude above sea level in Figures 7 and 8. The low energy window between 100 keV and 400 keV can be assumed to be influenced by photon emissions of the radon decay product ^{214}Pb with energies of 242 keV, 295 keV and 352 keV. Due to the higher attenuation of low energy photons in air, the influence of airborne ^{214}Pb near the helicopter can be assumed even larger compared to photons with higher energy produced by ^{214}Bi. The measured altitude profile over Lake Thun in Figure 7 shows an expected increase of count rate with elevated altitude. In contrast, the measured altitude profile over Lake Neuchâtel (Figure 8) depicts a pattern clearly different from the expected increase with altitude, for which the influence of the concentration profile of airborne radon progeny overwhelming the additional counts produced by cosmic radiation is the most likely cause. Baldocini et al. (2017) reported a similar influence of airborne radon progeny over the Mediterranean Sea. Assuming that the radon concentration profile (Figure 9) does always influence to a variable extent the determination of the cosmic stripping correction with the experimental method described in Schwarz (1991), this approach has to be reconsidered.

Until a better approach is developed, the slope averaged over the seven altitude profiles with sufficient altitude range without the altitude profile over Lake Neuchâtel of ARM22m is used in a second step to calculate the background count rates listed in Table 2 for each energy window. The use of unified slopes for all altitude profiles reduces the variation of background count rates. Due to statistical and systematic uncertainties, small negative background count rates can occur. The background count rates are determined for the individual detector-helicopter combination of each exercise from flights over extended water bodies near the main measuring areas. The background and slope used for the data evaluation of the current exercise are stored under identifiers ISWB_winname and ISWC_-winname in the header section of all ERS 2.0 files (Section 6) generated for ARM22 data.

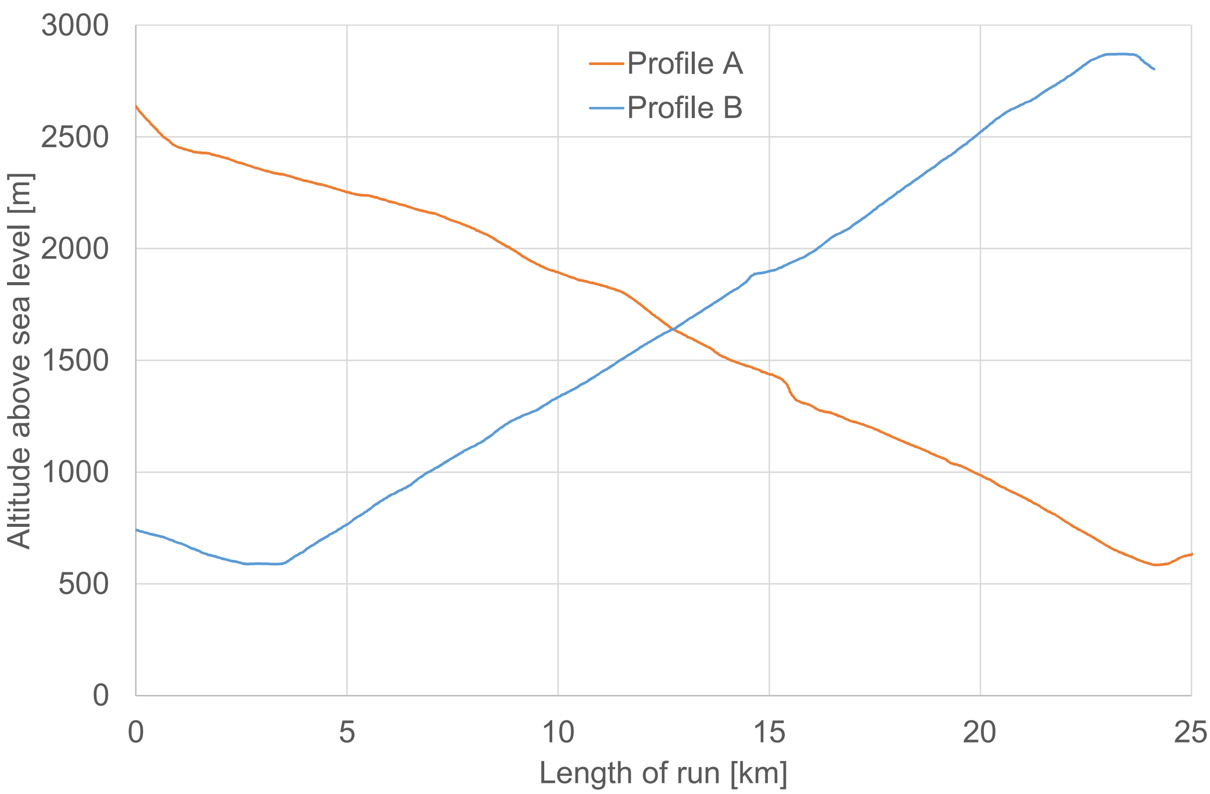

Figure 4: Altitude profiles over Lake Thun measured during ARM22c. Length of run is the length of the flight path projected to the lake surface including turns.

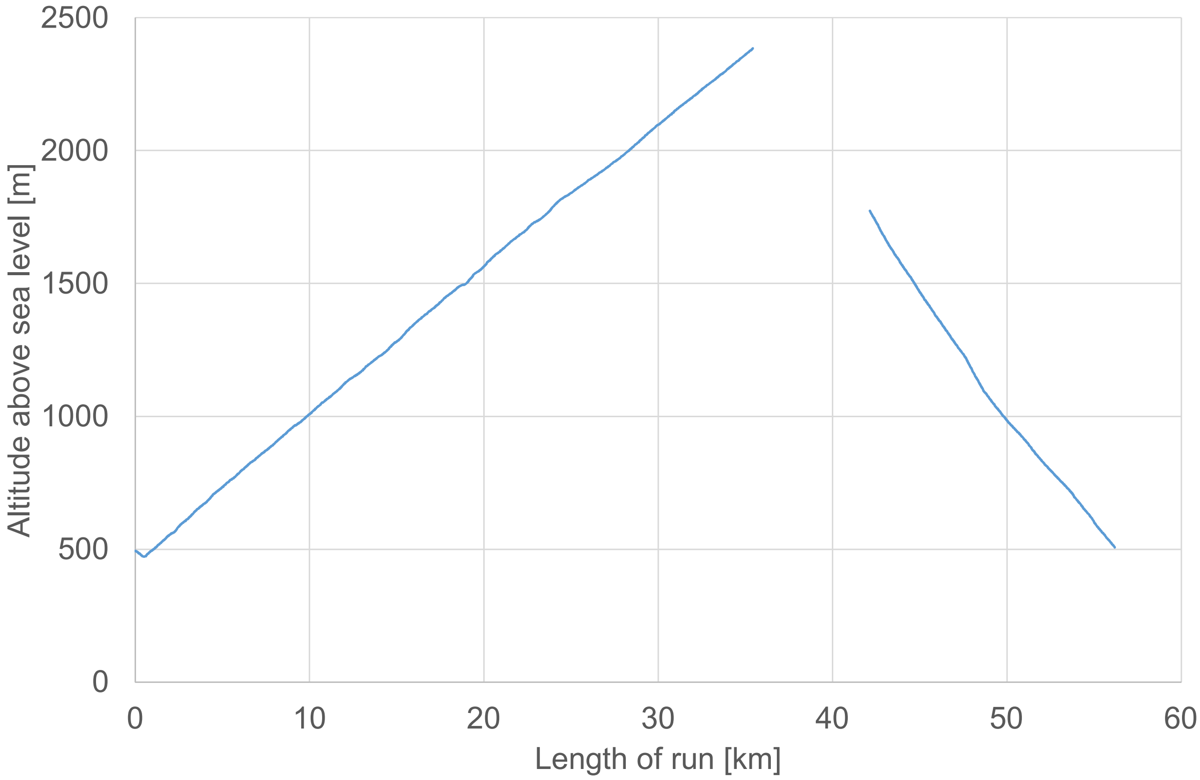

Figure 5: Altitude profile over Lake Neuchâtel measured during ARM22m. Length of run is the length of the flight path projected to the lake surface including turns. The gap indicates a turn over the lakeshore.

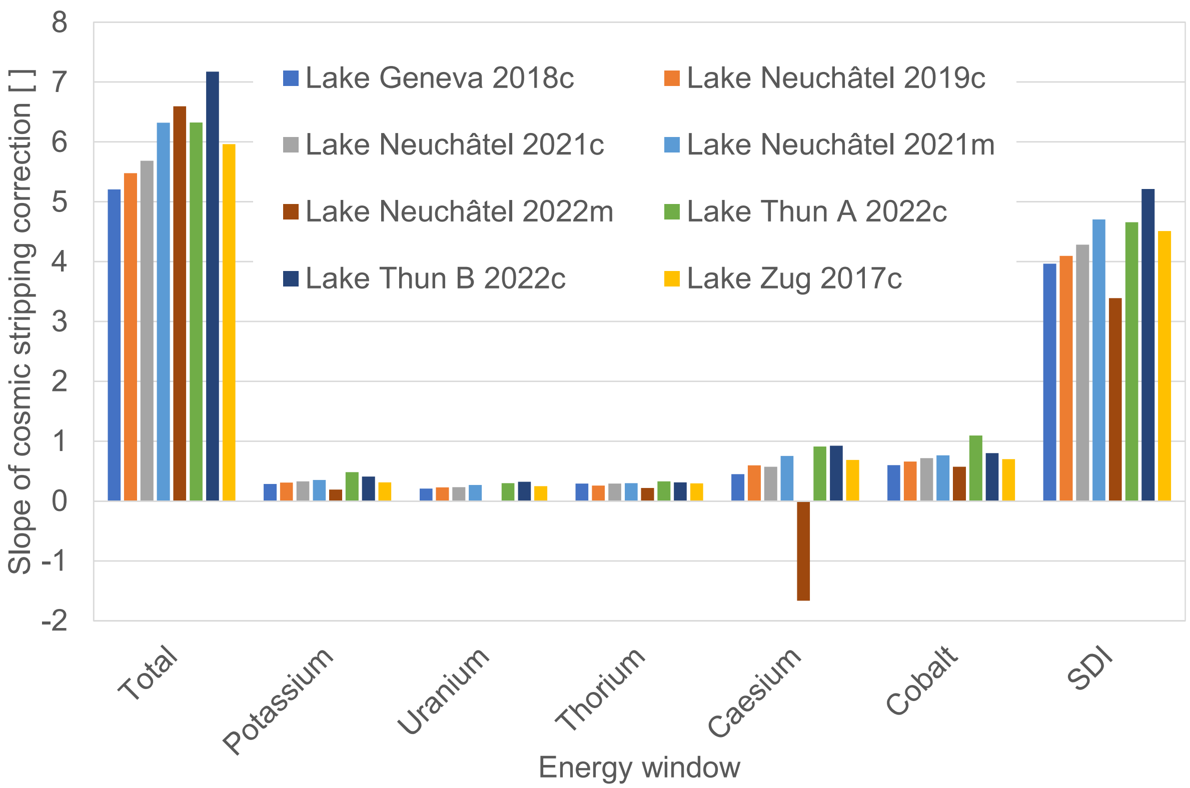

Figure 6: Slope of cosmic correction determined from altitude profiles.

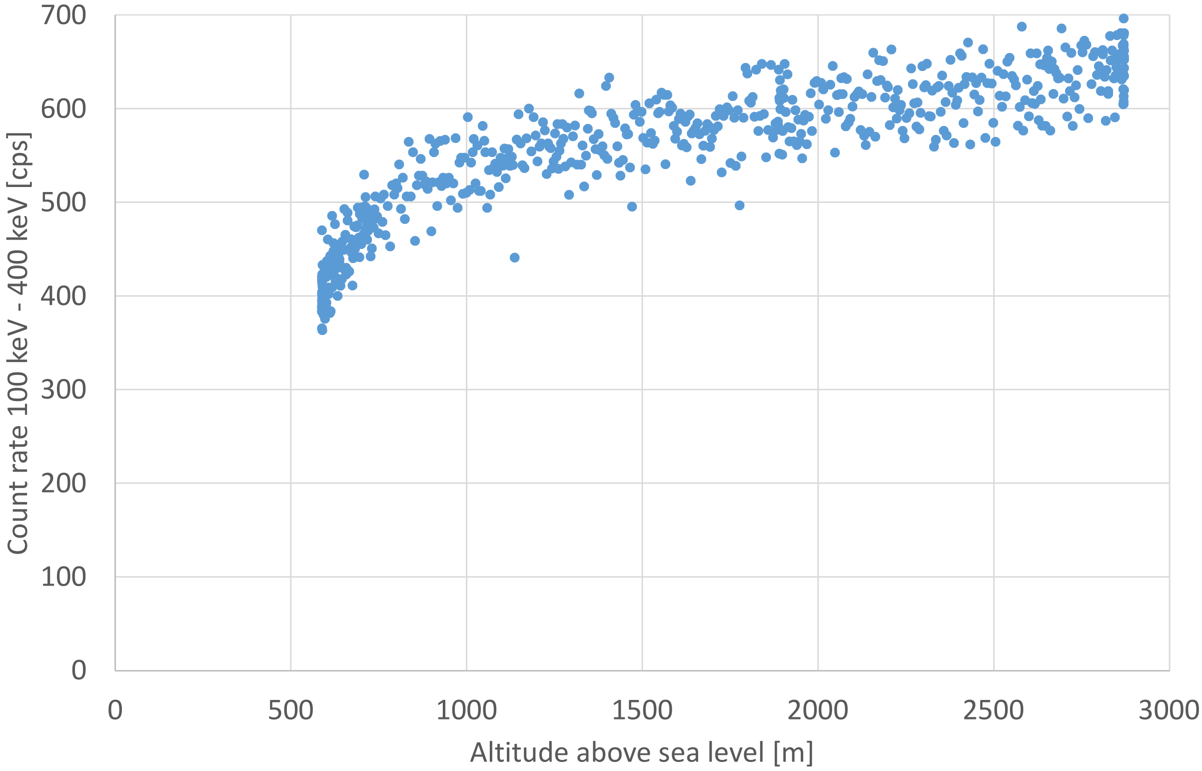

Figure 7: Count rate in the energy window between 100 keV and 400 keV for the altitude profile B over Lake Thun.

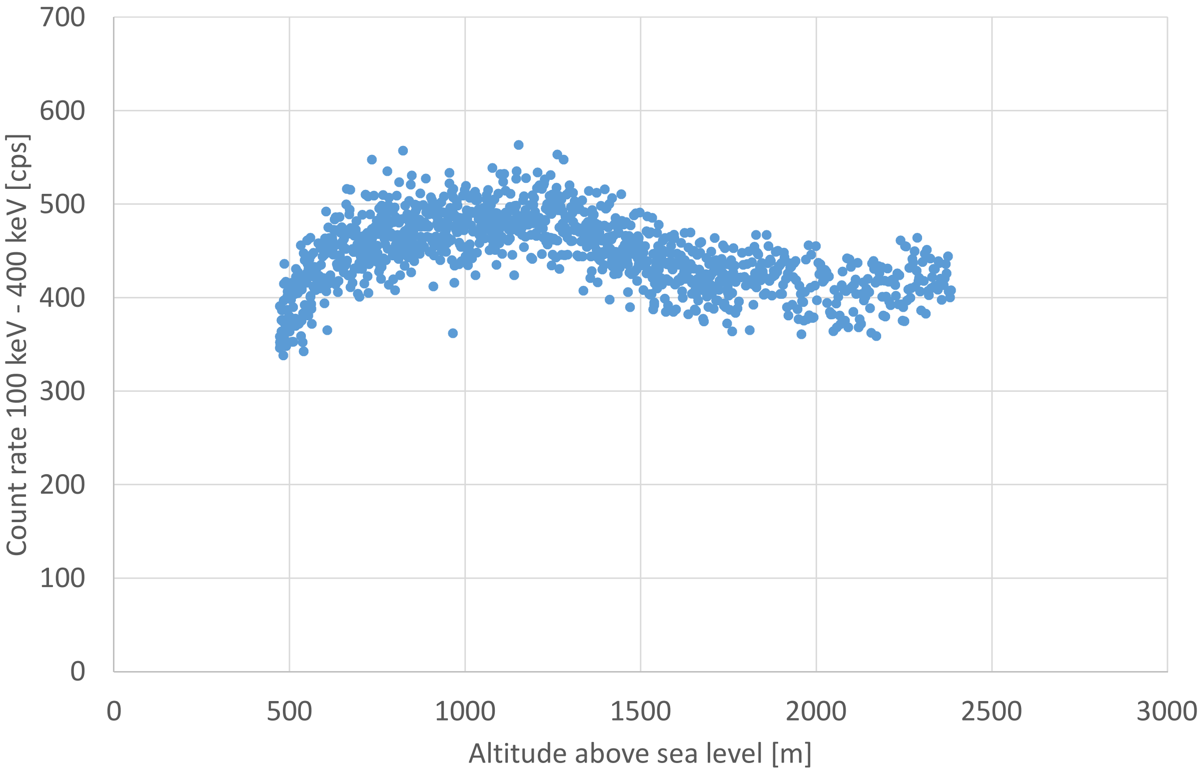

Figure 8: Count rate in the energy window between 100 keV and 400 keV for an altitude profile over Lake Neuâtel.

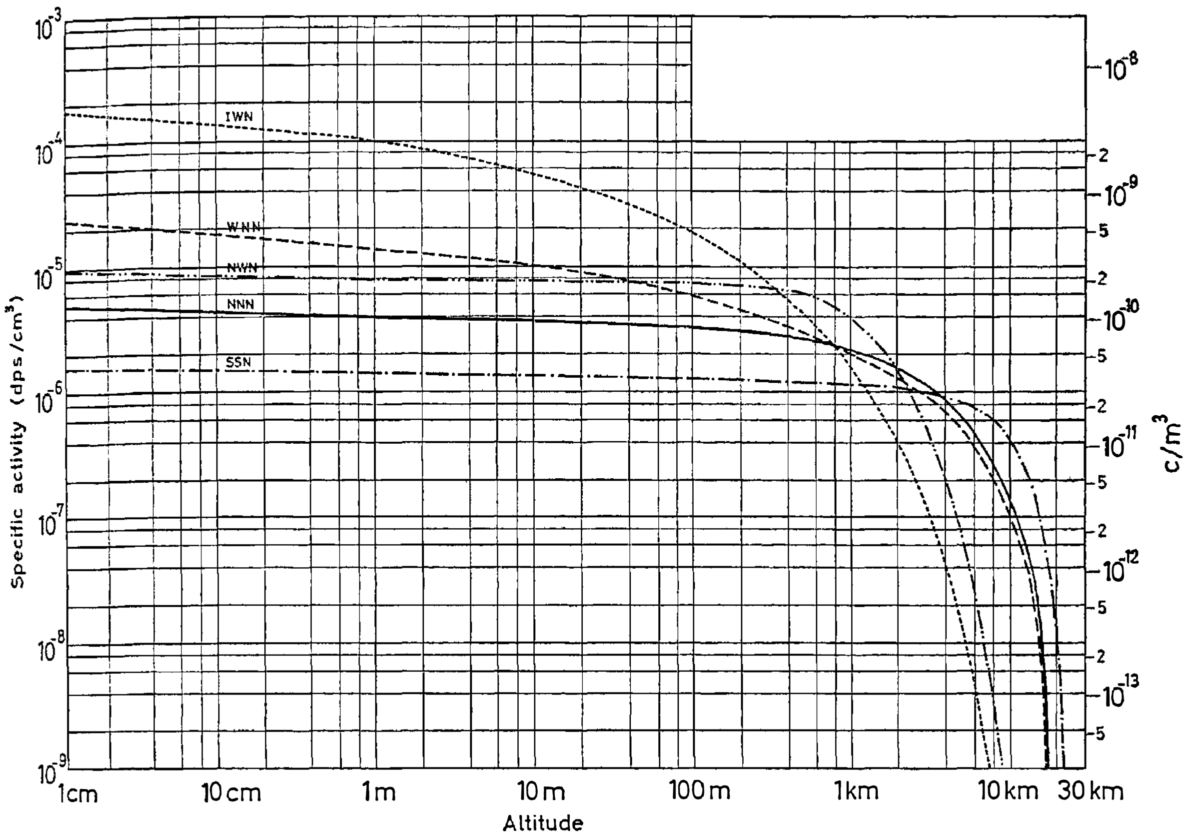

Figure 9: Radon profiles for different atmospheric conditions according to Jacobi and André, 1963.

	Slope of cosmic correction [ ]						
Energy Window	Total	Potassium	Uranium	Thorium	Caesium	Cobalt	SDI
Lake Geneva 2018	5.20	0.28	0.21	0.29	0.45	0.60	3.96
Lake Neuchâtel 2019	5.48	0.31	0.23	0.26	0.60	0.66	4.09
Lake Neuchâtel 2021c	5.68	0.33	0.23	0.29	0.57	0.72	4.28
Lake Neuchâtel 2021m	5.92	0.30	0.24	0.27	0.59	0.60	4.43
Lake Thun A 2022c	6.32	0.48	0.30	0.33	0.91	1.09	4.66
Lake Thun B 2022c	7.17	0.41	0.32	0.31	0.92	0.80	5.21
Lake Zug 2017	5.96	0.31	0.25	0.29	0.61	0.69	4.31
Average	6.02	0.35	0.26	0.30	0.70	0.76	4.49
Standard deviation	0.66	0.07	0.04	0.02	0.18	0.16	0.42

Table 1: Determination of the average slope for cosmic correction from seven altitude profiles with sufficient altitude range.

	Background count rate [cps]						
Energy Window	Total	Potassium	Uranium	Thorium	Caesium	Cobalt	SDI
Lake Geneva 2018	141	9	7	0.3	21	14	97
Lake Neuchâtel 2016	123	7	5	1.2	19	9	84
Lake Neuchâtel 2019	97	8	5	-1.0	14	9	65
Lake Neuchâtel 2021c	114	8	7	0.1	16	9	79
Lake Neuchâtel 2021m	138	9	7	0.4	21	12	93
Lake Neuchâtel 2022m	105	7	5	-0.7	17	9	70
Lake Thun A 2020c	68	5	3	-0.3	10	5	45
Lake Thun B 2020c	67	5	3	-0.4	10	5	45
Lake Thun A 2022c	128	8	6	0.0	20	12	87
Lake Thun B 2022c	151	9	7	0.6	23	14	104
Lake Zug 2017	50	4	2	-0.2	7	2	34

Table 2: Determination of the background count rate using the average slope of cosmic stripping from Table 1

.

1.3.2 Characterisation of spectral cross-talk

Photons emitted from the soil are scattered due to the Compton effect in the soil itself, in buildings, in vegetation, in the air between surface and helicopter, in the helicopter and in the detector. The associated energy loss may lead to a registration of the photon in a lower photon energy window. Further contributions to cross-talk effects come from the limited energy resolution of a NaI(Tl)-detector compared to modern solid-state detectors causing the possibility that photons with energies near the energy limits of a photon energy window are registered in the adjacent energy window. Additionally, as natural uranium and thorium are the entry point of a complete decay series, multiple photons are emitted throughout the whole energy spectrum. The spectral counts in the various energy windows associated with these photon emissions have to be corrected. The counts, which have to be subtracted in the respective energy window, can be determined with measurements of radioactive point sources near the detector, which are then corrected for altitude and scattering in soil for the natural radionuclides (Schwarz et al., 1997). The according measurements were performed after the exercise for detector RLL003, used in exercise part ARM22m (Figure 10). As detector RLL001, used during ARM22c, was not modified since the last exercise, the stripping factors determined in 2020 were used. Table 3 gives an overview on the current stripping factors of the four Swiss systems. The values for Detector RLL002 and RLL004 were determined for three of the four NaI crystals due to quality issues. The results indicate that the individual stripping factors determined for each detector may be replaced with a generic set of factors, under the condition that all four systems perform inside their specifications. The stripping factors are stored under the ISWS identifier in the header of the ERS 2.0 data files (Section 6).

Figure 10: Detector RLL003 mounted in the laboratory for the determination of stripping factors.

Detector		RLL001	RLL002	RLL003	RLL004
Year		2020	2019	2022	2021
"‘from"’-window	"‘to"’-window	Stripping factor			
Uranium	Potassium	0.93	0.95	0.98	0.92
Thorium	Potassium	0.48	0.45	0.50	0.47
Cobalt	Potassium	0.07	0.00	0.05	0.04
Thorium	Uranium	0.36	0.36	0.34	0.34
Uranium	Thorium	0.05	0.06	0.06	0.05
Potassium	Caesium	0.45	0.46	0.48	0.37
Uranium	Caesium	3.16	3.30	3.18	2.78
Thorium	Caesium	1.65	1.65	1.64	1.44
Cobalt	Caesium	0.15	0.10	0.13	0.12
Potassium	Cobalt	0.76	0.76	0.79	0.66
Uranium	Cobalt	2.37	2.32	2.32	2.26
Thorium	Cobalt	0.68	0.61	0.63	0.65

Table 3: Stripping factors for relevant energy windows of the RLL detectors.

1.4 Data presentation

Brief reports of the measurement results are compiled by the respective measurement teams and published immediately after the end of the exercise on the homepage of NEOC and the homepage of NBC-EOD Centre of Competence. These reports are archived at `https://far.ensi.ch` under Publications (each year as Short Reports - NEOC). A combined detailed analysis of both parts of the exercise is published in the form of a PSI-report within the responsibility of the FAR. These reports are archived at `https://far.ensi.ch` (as Scientific Reports).

For all measuring areas, a map of the total dose rate (ambient dose equivalent rate dH*(10)/dt extrapolated to 1 m above ground) and the flight lines is presented together with a map of the Man-Made-Gross-Count (MMGC) ratio. The MMGC-ratio is the quotient between the count rate summed over the energy window (MMGC1) between 400 keV and 1400 keV and the count rate summed over the energy window between 1400 keV and 3000 keV (MMGC2). As most anthropogenic radionuclides emit photons below 1400 keV, the ratio will rise due to these additional photons, whereas natural radionuclides are registered in both energy windows, keeping the ratio relatively constant. Unusual low counts in the MMGC2 energy window due to limited counting statistics can also lead to increased MMGC-ratios.

A map of the ^{232}Th activity concentration (measuring quantity activity per wet mass) provides information on the quality of the measurements, as it can be expected that this quantity is constant over time. As an additional quality measure, an appendix with the basic parameters of the data evaluation is added to simplify a re-evaluation of the data in the future. If the dose rate or the MMGC-ratio indicates elevated values, maps of individual radionuclides (like e.g. ^{40}K or ^{137}Cs activity concentrations) are added based on the average photon spectrum over the affected area. In the case of large changes of topography in the measured area, a map of the terrestrial dose rate consisting of the total dose rate reduced by the altitude dependent cosmic component is included. In the case of measuring flights with the main purpose of mapping natural radionuclide concentrations, a supplementary map of the ^{40}K activity concentration (measuring quantity activity per wet mass) may also be presented.

A discrete colour scale was defined by the Swiss Expert Group for Aeroradiometrics (FAR) in 2019. The colours and their representation as red, green and blue (RGB) values are listed in Table 4 together with the represented ranges of measured values. The unit of ambient dose-equivalent rates used in previous reports, [nSv/h], was changed with the new representation to [μSv/h], the unit used to store ambient dose-equivalent rate values in the ERS 2.0 format (Butterweck et al. (2018)).

Colour	Red	Green	Blue	Dose rate [μSv/h]	MMGC-ratio [ ]	Activity per mass [Bq/kg] ^{40}K	Activity per mass [Bq/kg] ^{238}U, ^{232}Th, ^{137}Cs	Activity per area [kBq/m^2] ^{137}Cs (β=9.5 g/cm^2)
	153	0	153	> 10	> 100	> 10000	> 5000	> 1000
	204	0	102	5 - 10	50 - 100	5000 - 10000	1000 - 5000	200 - 1000
	204	0	0	2 - 5	15 - 50	2000 - 5000	500 - 1000	100 - 200
	255	0	0	0.5 - 2	9 - 15	1500 - 2000	250 - 500	50 - 100
	255	176	51	0.3 - 0.5	8 - 9	1000 - 1500	200 - 250	40 - 50
	255	235	51	0.2 - 0.3	7 - 8	800 - 1000	150 - 200	30 - 40
	230	255	128	0.15 - 0.2	unused	600 - 800	100 - 150	20 - 30
	173	255	153	0.1 - 0.15	unused	400 - 600	75 - 100	15 - 20
	073	255	106	0.08 - 0.1	6 - 7	200 - 400	50 - 75	10 - 15
	102	255	255	0.06 - 0.08	5 - 6	100 - 200	25 - 50	5 - 10
	77	148	255	0.04 - 0.06	unused	50 - 100	12.5 - 25	2.5 - 5
	51	102	179	< 0.04	< 5	< 50	< 12.5	< 2.5

Table 4: Quantification of the colour scale.

2 Results of the exercise ARM22

The flights of the civil (ARM22c) and military (ARM22m) parts of the exercise were performed between June 13th and 17th and between September 5th and September 9th, respectively.
Flight velocity of the Super Puma helicopters of the Swiss Air Force was around 30 m/s with a target ground clearance of 90 m for all measuring flights. The sampling interval of the spectra was one second.
Personnel of the military units Stab BR NAZ and ABC Abwehr Einsatzkompanie performed the measurements supported by experts from ENSI, PSI, ETHZ, NBC-EOD Centre of Competence and NEOC.
Flight parameters of the measuring flights are listed in Table 5 and an overview of the according flight lines is shown in Figure 11.

Location	Flight identification	Measuring time [s]	Length of run [km]	Area [km^2]
Altitude profiles over lakes				
Lake Thun A	Heli 1_20220616 0735	770		
Lake Thun B	Heli 1_20220616 1504	601		
Lake Neuchâtel	Heli 3_20220905 1605	1473		
Recurrent measuring areas over nuclear installations				
KKB, KKL, PSI and Zwilag	Heli 1_20220613 0952 Heli 1_20220613 1353	14653	727	172
Background measurements over cities, towns and regions				
Zürcher Unterland	Heli 1_20220615 0830 Heli 1_20220615 1352 Heli 1_20220615 1514 Heli 1_20220615 1608	18785	791	213
Chur	Heli 1_20220614 1351	2475	117	24
Zollikerberg	Heli 1_20220614 1458	3324	144	33
District Jura-Nord vaudois	Heli 3_20220905 0915 Heli 3_20220905 1350	16192	655	156
Districts Riviera and Gruyère	Heli 3_20220906 0845 Heli 3_20220906 1350 Heli 3_20220907 1520 Heli 3_20220909 0855 Heli 3_20220909 1045	29706	1255	273
Districts Broye et Glâne	Heli 3_20220907 1335 Heli 3_20220907 1425 Heli 3_20220908 0850	16492	700	144
Val de Travers	Heli 3_20220906 1050 Heli 3_20220908 1347 Heli 3_20220908 1525	10470	411	74
Measurements over alpine valleys				
Rheinwald, Misox and Val Calanca	Heli 1_20220614 0931	7251	277	50
Weisstannental	Heli 1_20220614 0909	652	21	2

Table 5: Flight data of ARM22.

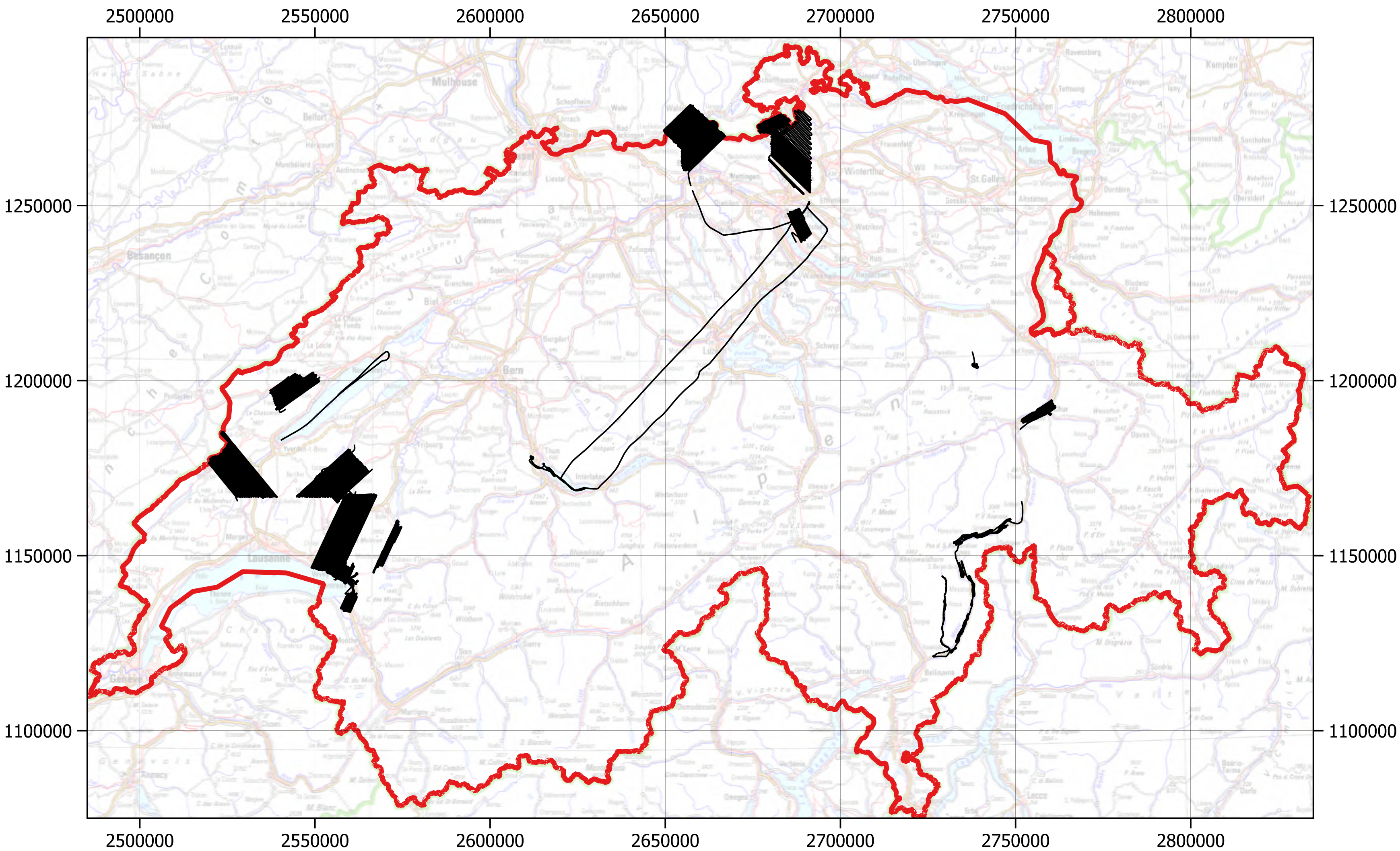

Figure 11: Overview of the measurement areas of ARM22. Geodaten©swisstopo.

2.1 Recurrent measurement area KKB, KKL, PSI and Zwilag

According to a biennial sequence of routine measurements, the environs of the nuclear power plants Beznau (KKB) and Leibstadt (KKL), the nuclear facilities at the Paul Scherrer Institute and the intermediate storage facility Zwilag were inspected in 2022. Following a request of German authorities, the measuring area was extended beyond the Rhine river into German territory.

The dose rate map (Figure 13) shows variations due to different concentrations of natural radionuclides and the attenuating water layers of Rhine and Aare rivers. The nuclear power plant Leibstadt (KKL) was out of operation due to the annual maintenance. Thus, the photon radiation of ^{16}N detected in previous years was not present. The man-made gross-count (MMGC) ratio, an indicator for the presence of man-made radionuclides, displays slightly elevated readings in the east of PSI and at the Rhine river north of Full-Reuenthal (Figure 14). An analysis of the measured spectra at the elevated point near PSI indicates, as already observed in past years, the 511 keV annihilation peak associated with radionuclides emitted from the stack of the PSI West facility. A slight low energy asymmetry of the 511 keV peak indicates an additional signal, which could be attributed to the photon emission of ^{24}Ne with an energy of 472 keV (Figure 12). The short-lived noble gas isotope ^{24}Ne is also emitted from the stack of the PSI West facility. All of these emissions are permitted and continuously monitored.

The elevated value near Full-Reuenthal is located at the Rhine river bank and could be attributed to an unusual low signal of natural radionuclides in the high energy range, which is a common cause for artefacts in the MMGC-ratio.

The activity concentration of the natural radionuclide ^{232}Th (Figure 15) shows slightly elevated values over the Rotbergegg due to an increased natural Thorium content already observed in the past.

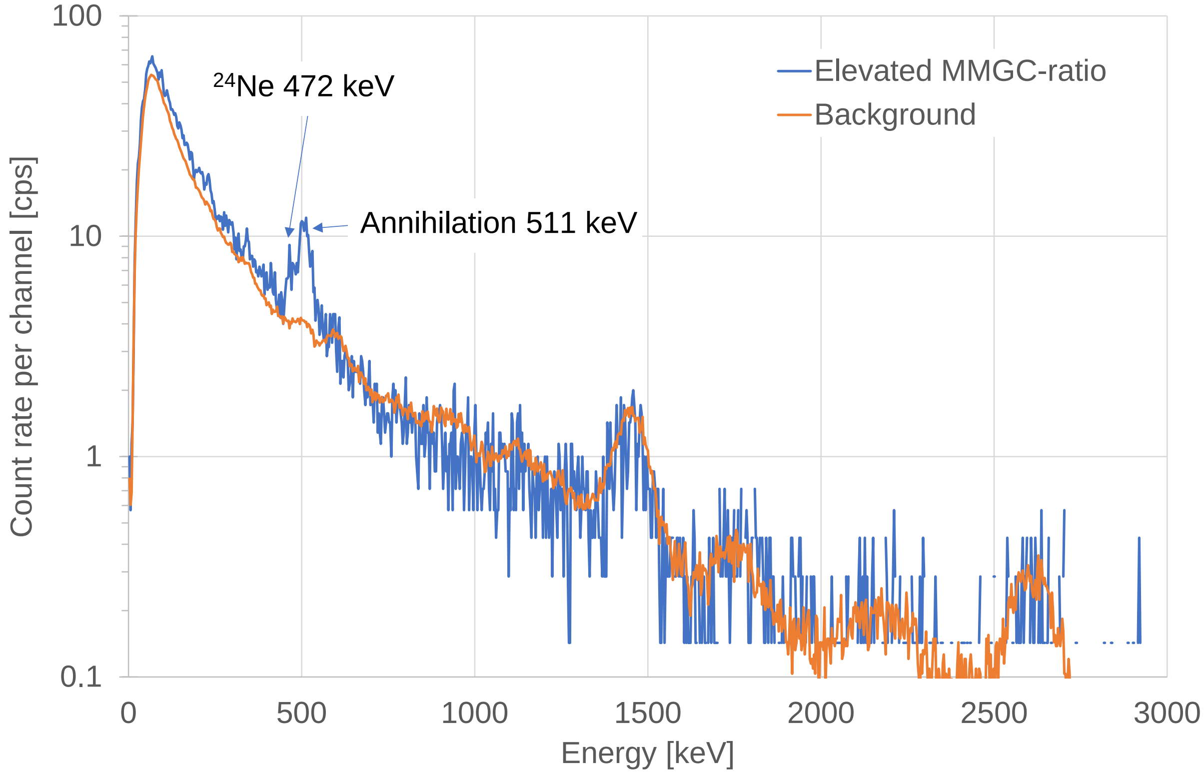

Figure 12: Spectrum over the point with an elevated MMGC-ratio compared to a background spectrum in the vicinity.

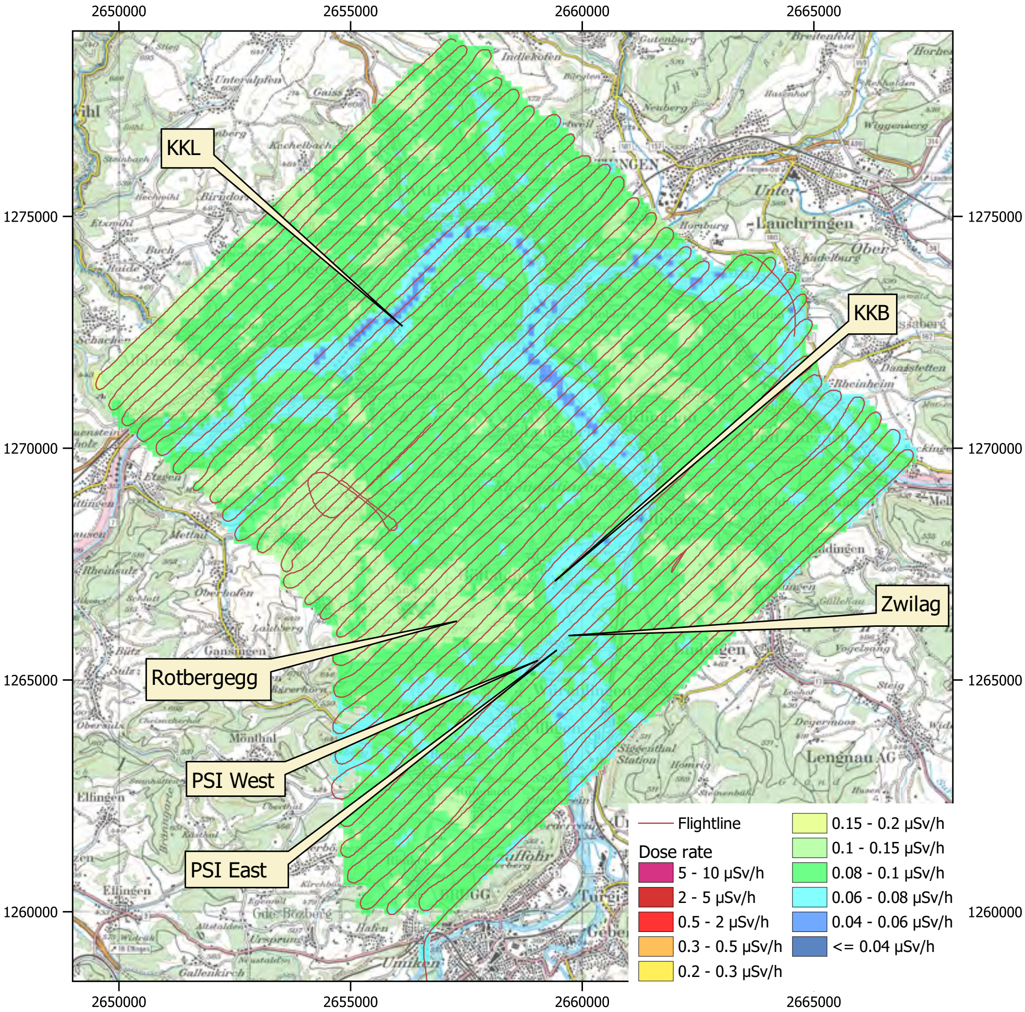

Figure 13: Dose rate in the measurement area KKB, KKL, PSI and Zwilag. Geodaten©swisstopo.

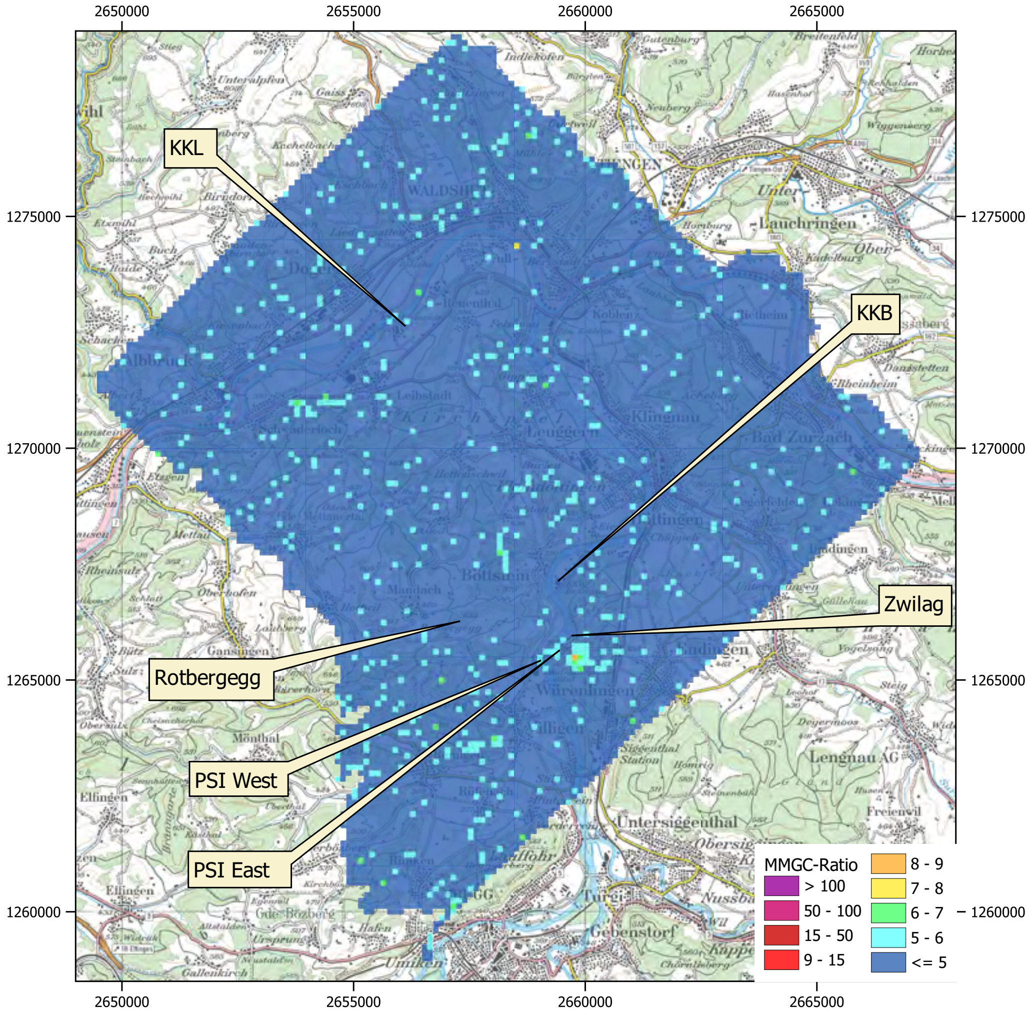

Figure 14: MMGC-ratio in the measurement area KKB, KKL, PSI and Zwilag. Geodaten©swisstopo.

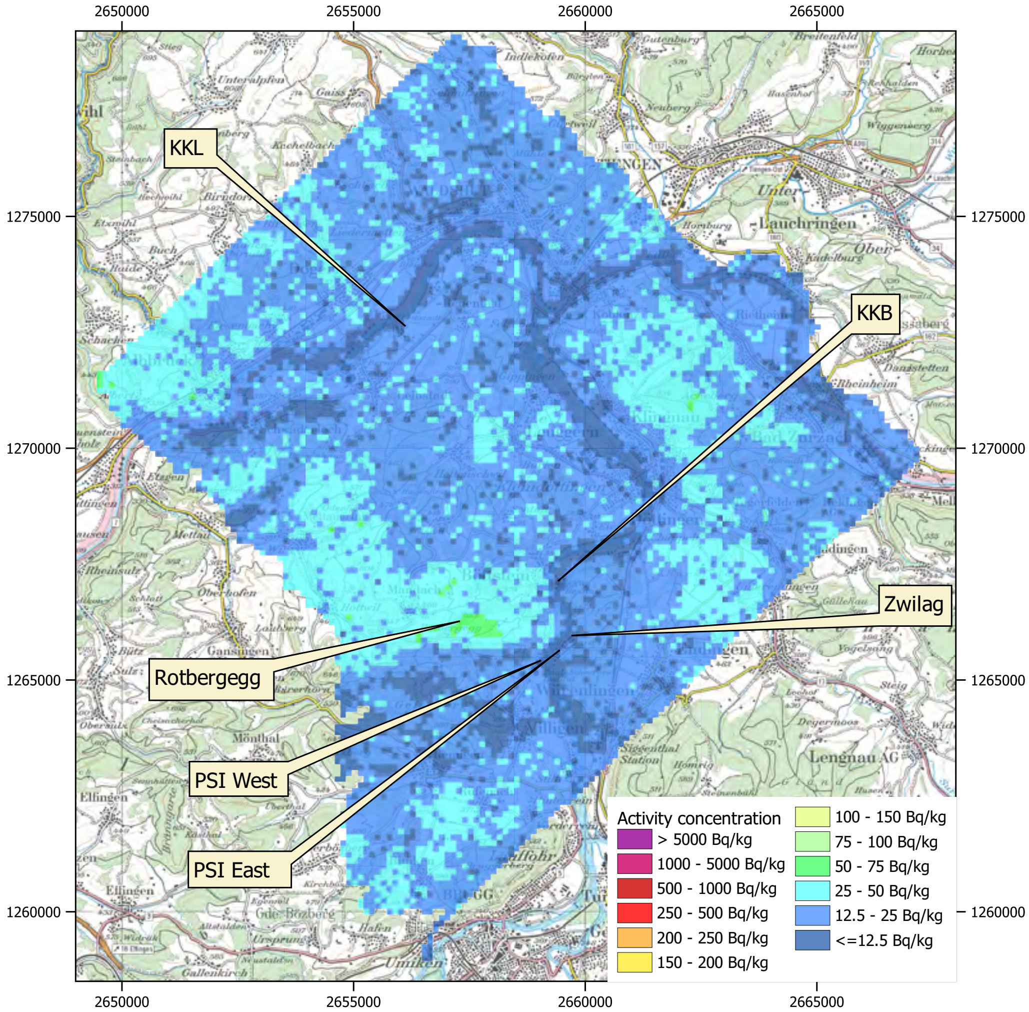

Figure 15: ^{232}Th activity concentration in the vicinity KKB, KKL, PSI and Zwilag. Geodaten©swisstopo.

2.2 Zürcher Unterland

Part of the region Zürcher Unterland (Zurich lowlands) located to the north of Zurich was measured during ARM22c. The map of the dose rate over the measured region shows typical background values (Figure 16). The map of the man-made gross count (MMGC) ratio as an indicator for the presence of man-made radionuclides displays a few points with elevated readings (Figure 17). The summed count rates in the MMGC1 and MMGC2 energy windows for the ten measuring points with the largest MMGC-ratios were compared to the average over the whole measurement area. In all cases, count rates well below average in the MMGC2 energy window could be determined as the cause of the elevated MMGC-ratios. The map of the ^{232}Th activity concentration (Figure 18) shows low values with a slight increase in the northern part of the measuring area, which are associated with granitic sands and sandstone located in this area.

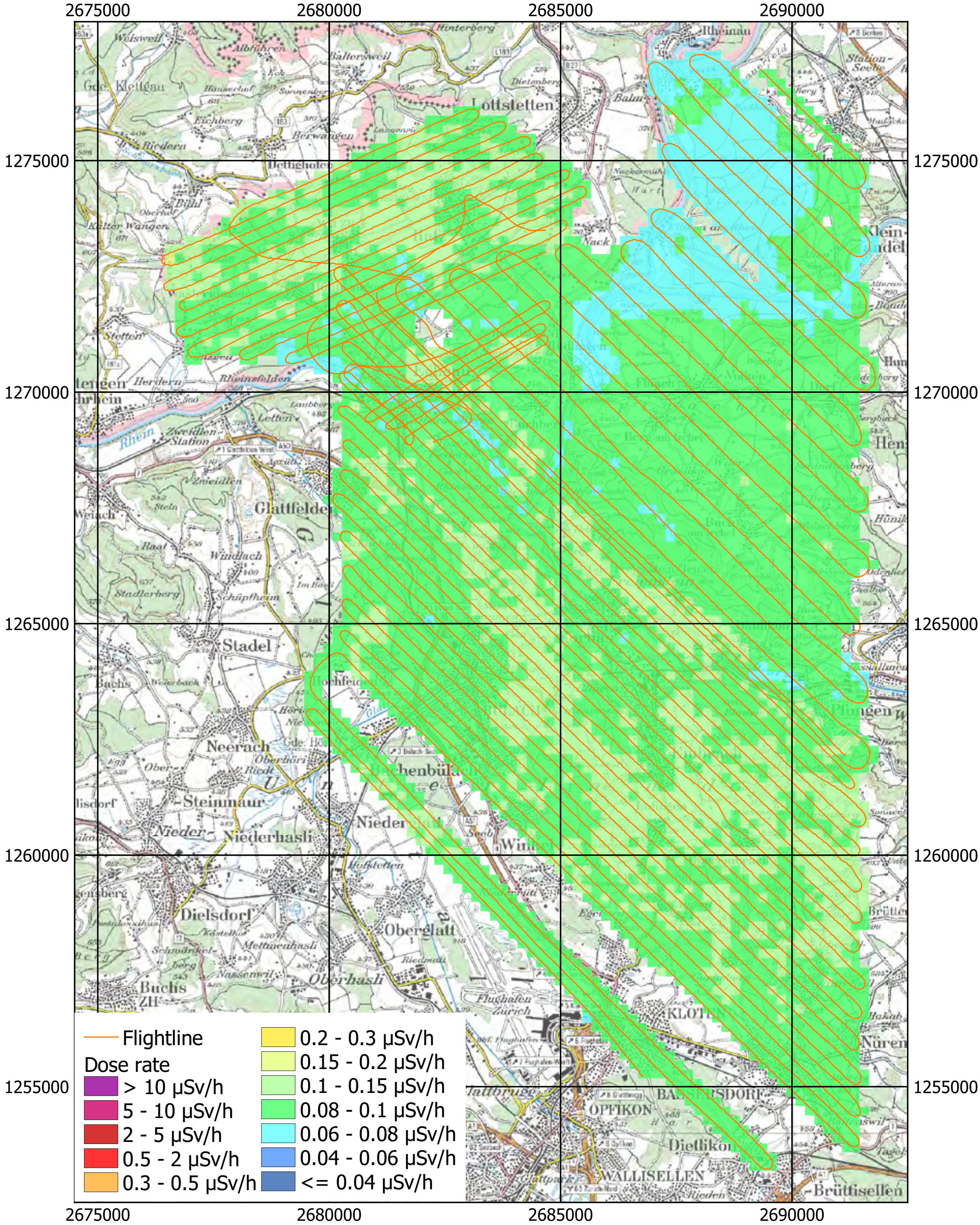

Figure 16: Dose rate over the Zürcher Unterland. Geodaten©swisstopo.

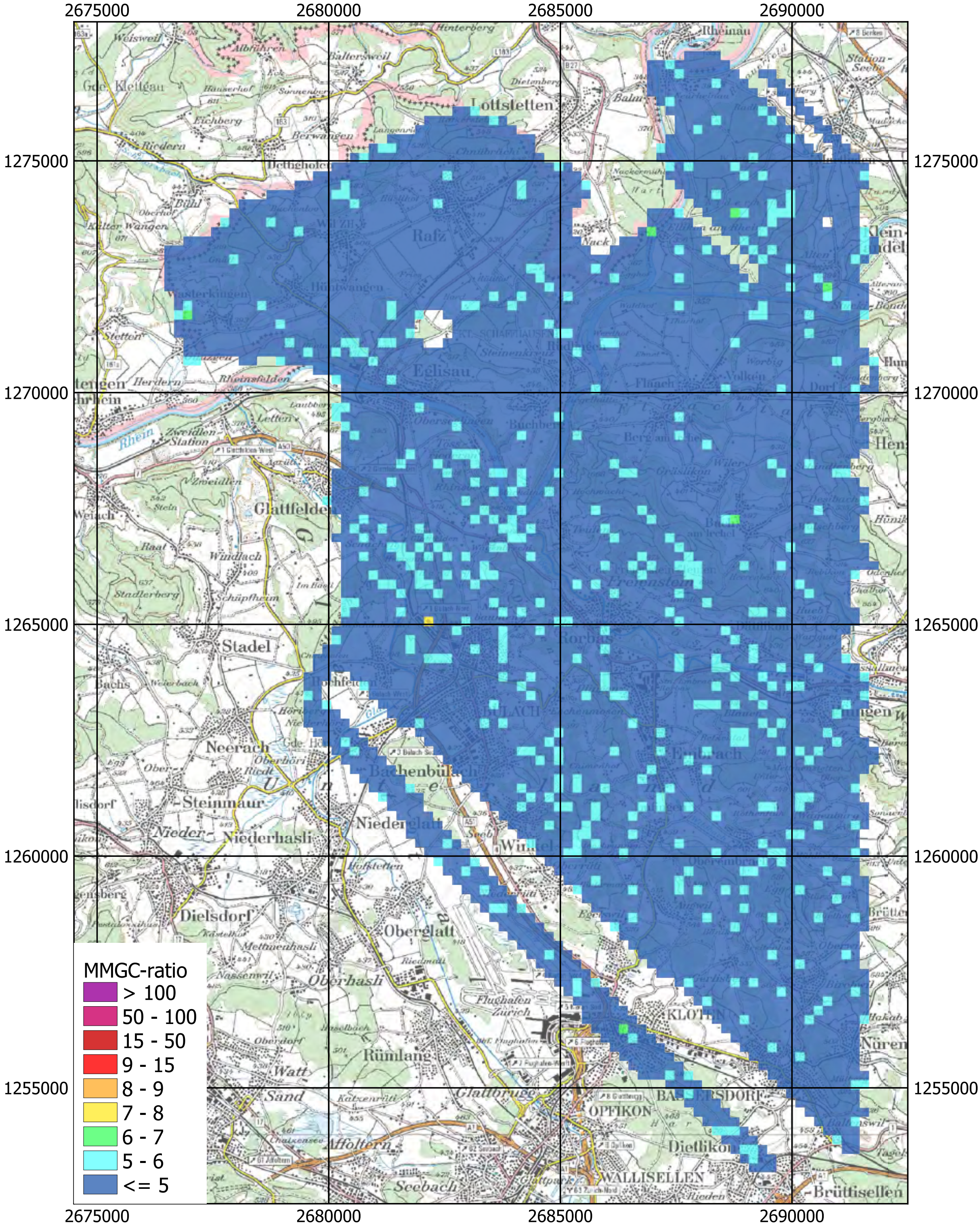

Figure 17: MMGC-ratio over the Zürcher Unterland. Geodaten©swisstopo.

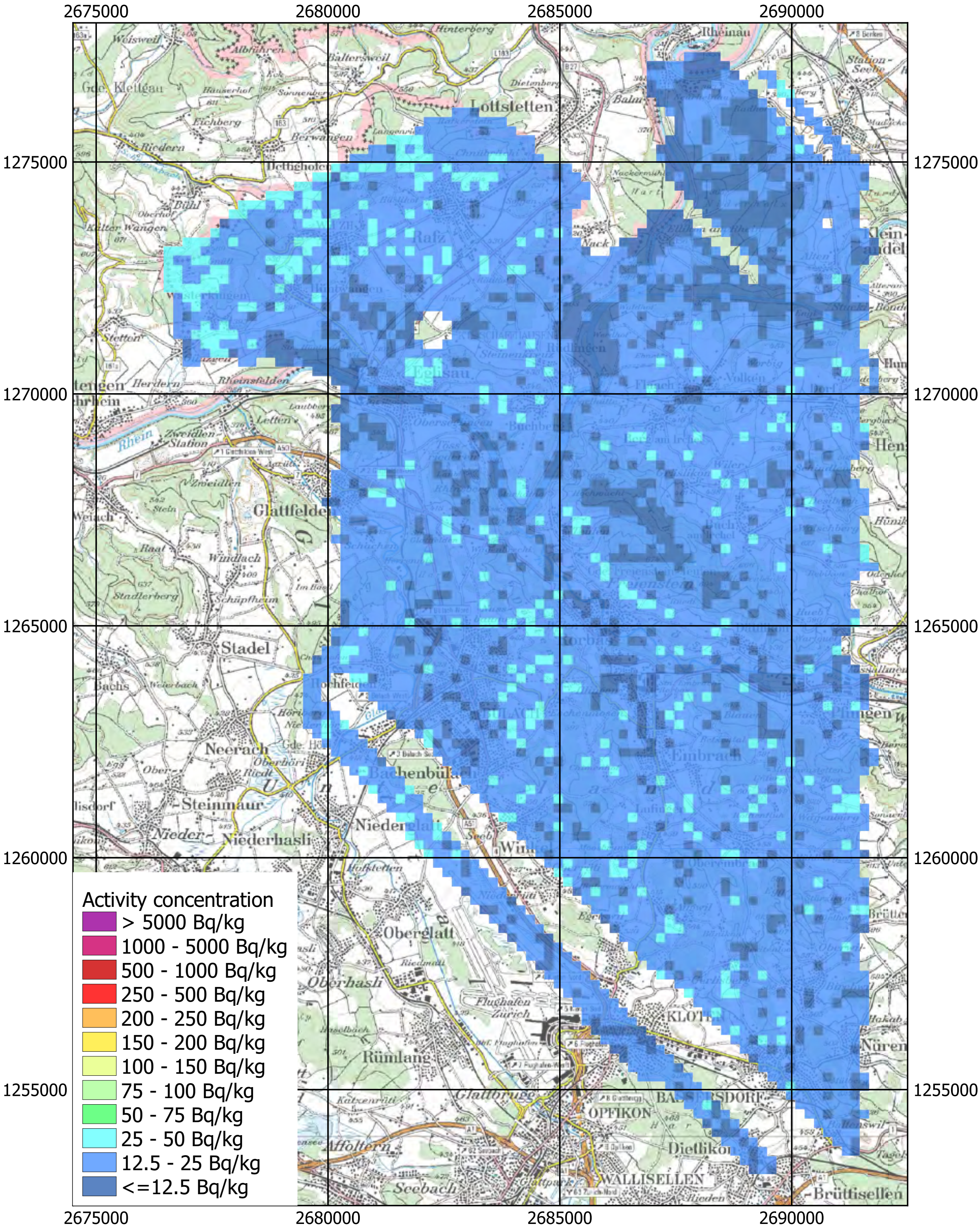

Figure 18: ^{232}Th activity concentration over the Zürcher Unterland. Geodaten©swisstopo.

2.3 Chur

The dose rate map in the area of Chur, Domat/Ems and Felsberg (Figure 19) shows typical background values occurring in Switzerland, ranging between 0.08 μSv h^{-1} in urban areas to 0.15 μSv h^{-1} in rural areas. The lower dose rate values registered in a confined region in the north of Felsberg are attributed to a terrain with exposed rock and gravel, left by a recent mountain slide.

Figure 20 shows no significant man-made radioactivity over the entire screened area. Further investigations on the green point visible in the Felsberg region, representing a slightly increased MMCG-ratio value, have attributed its origin to a MMCG-ratio computation artefact, occurring when the background is particularly low. As can be inferred from Figure 21, no elevated activity concentration of naturally occurring ^{232}Th in the area of Chur was detected.

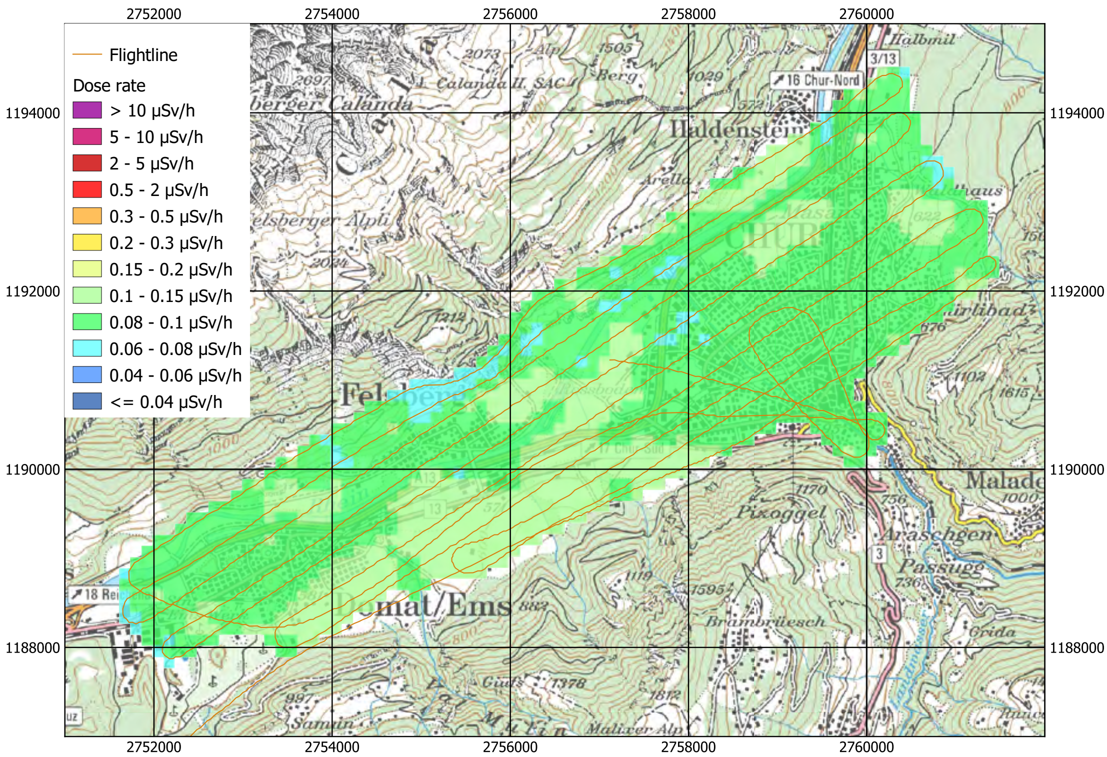

Figure 19: Dose rate near Chur. Geodaten©swisstopo.

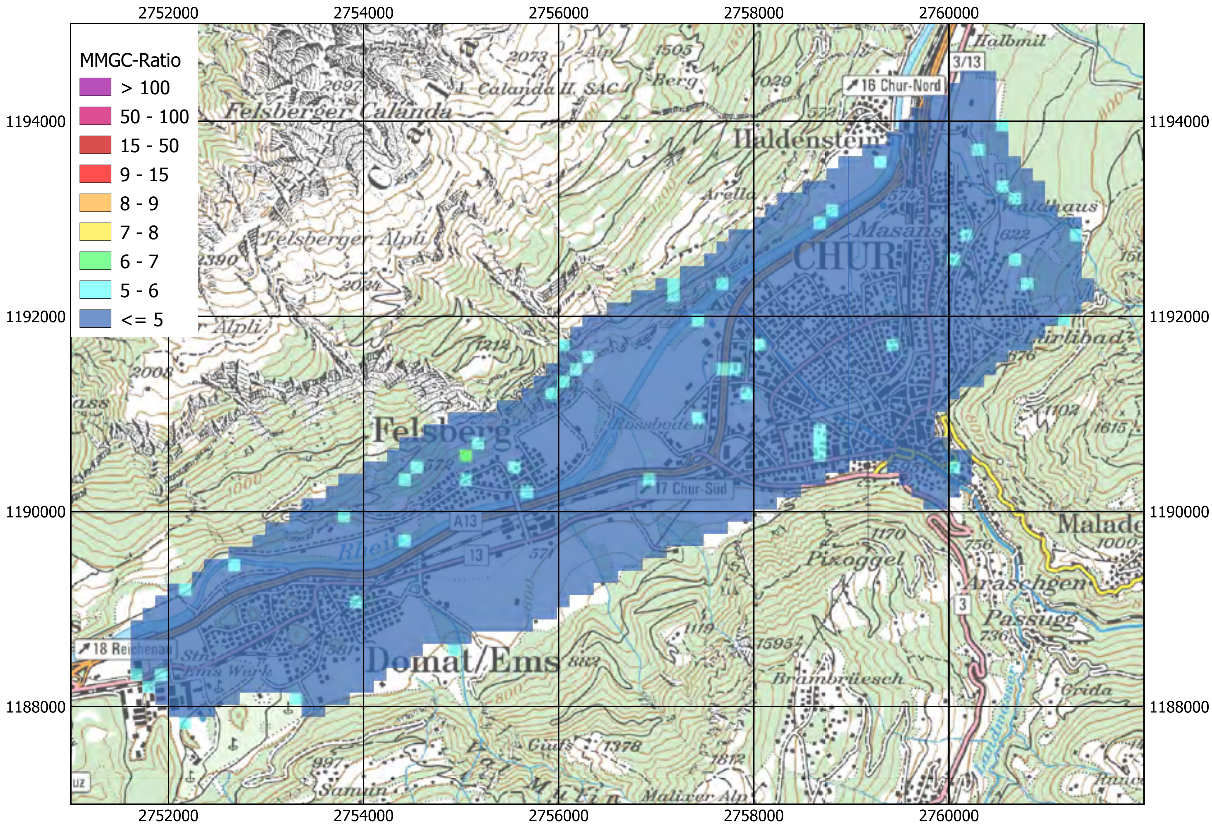

Figure 20: MMGC-ratio near Chur. Geodaten©swisstopo.

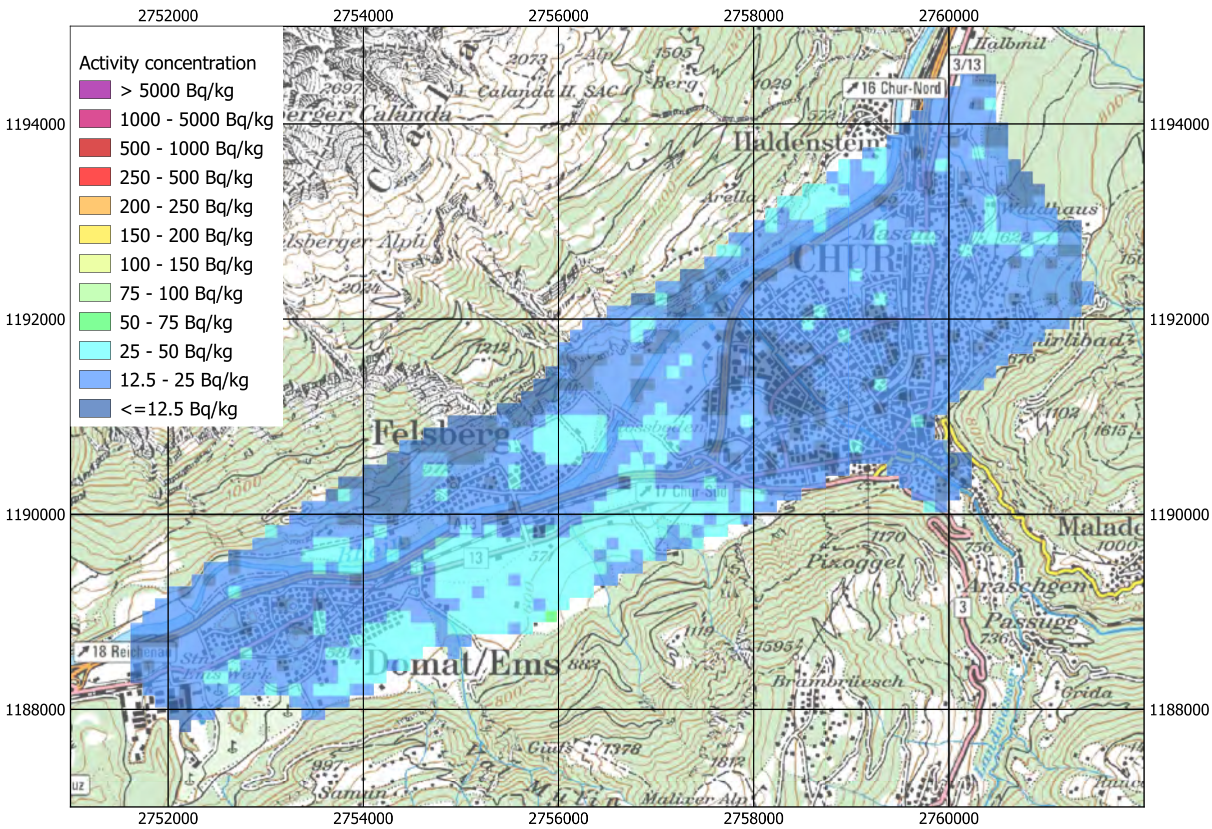

Figure 21: ^{232}Th activity concentration near Chur. Geodaten©swisstopo.

2.4 Zollikerberg

The data acquired over the region of the northern Pfannenstiel-Zürichberg chain (Figure 22) around Zollikerberg indicate a background dose-rate in line with the typical background values found in Switzerland. Small variations are attributed to the topography and degree of urbanisation.
Figure 23 shows no significant man-made radioactivity over the entire screened area. Additional analyses in the small regions of interest, centred on the green points visible on the MMGC-ratio, have confirmed that the slightly higher MMGC-ratio values detected were indeed artefacts, caused by the low background signal acquired, rather than a real indication of a presence of man-made radionuclides.
Figure 24 displays the ^{232}Th activity concentration on the area near Zollikon, characterised by a low and uniform distribution.

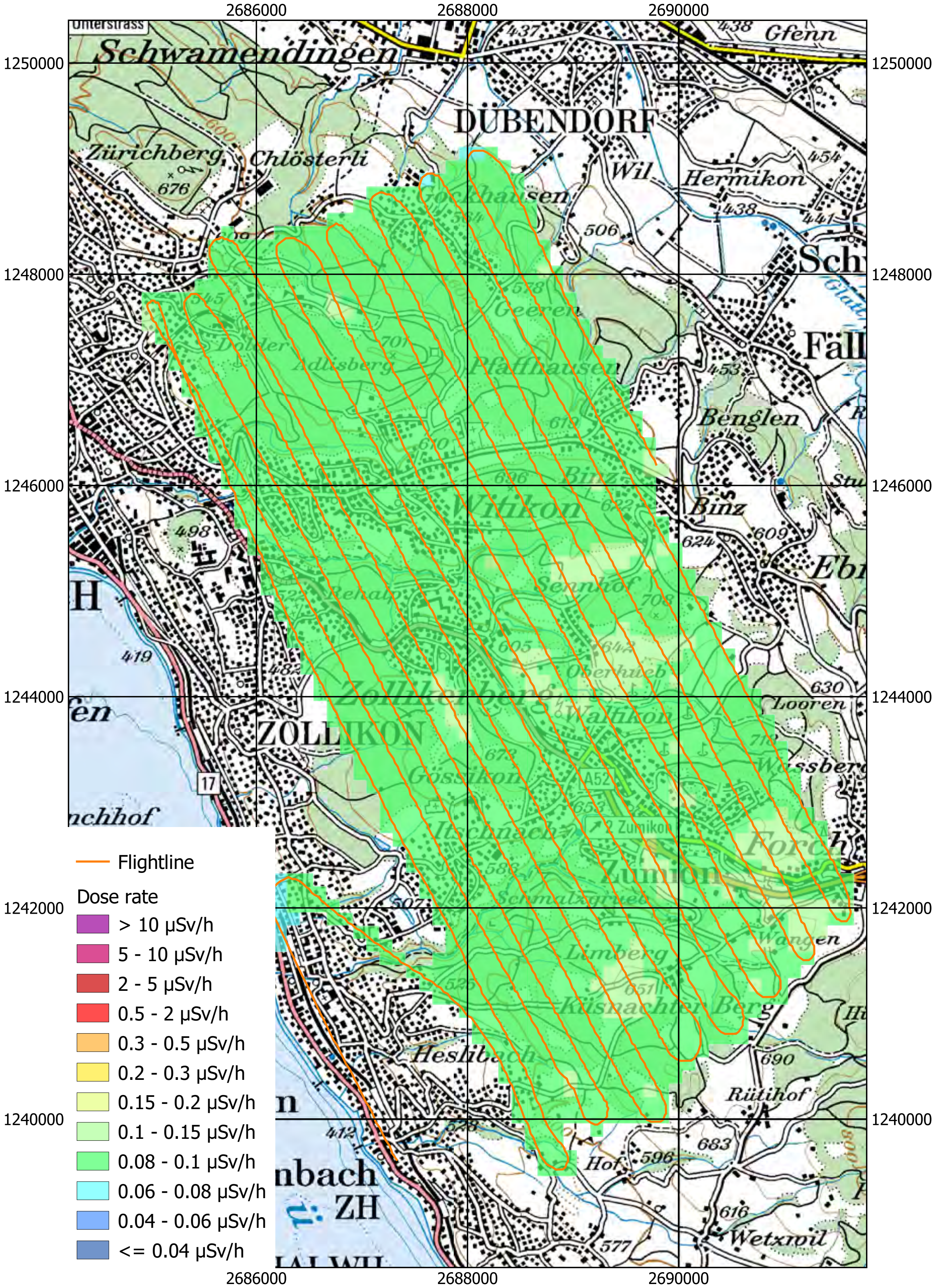

Figure 22: Dose rate near Pfannenstiel-Zürichberg. Geodaten©swisstopo.

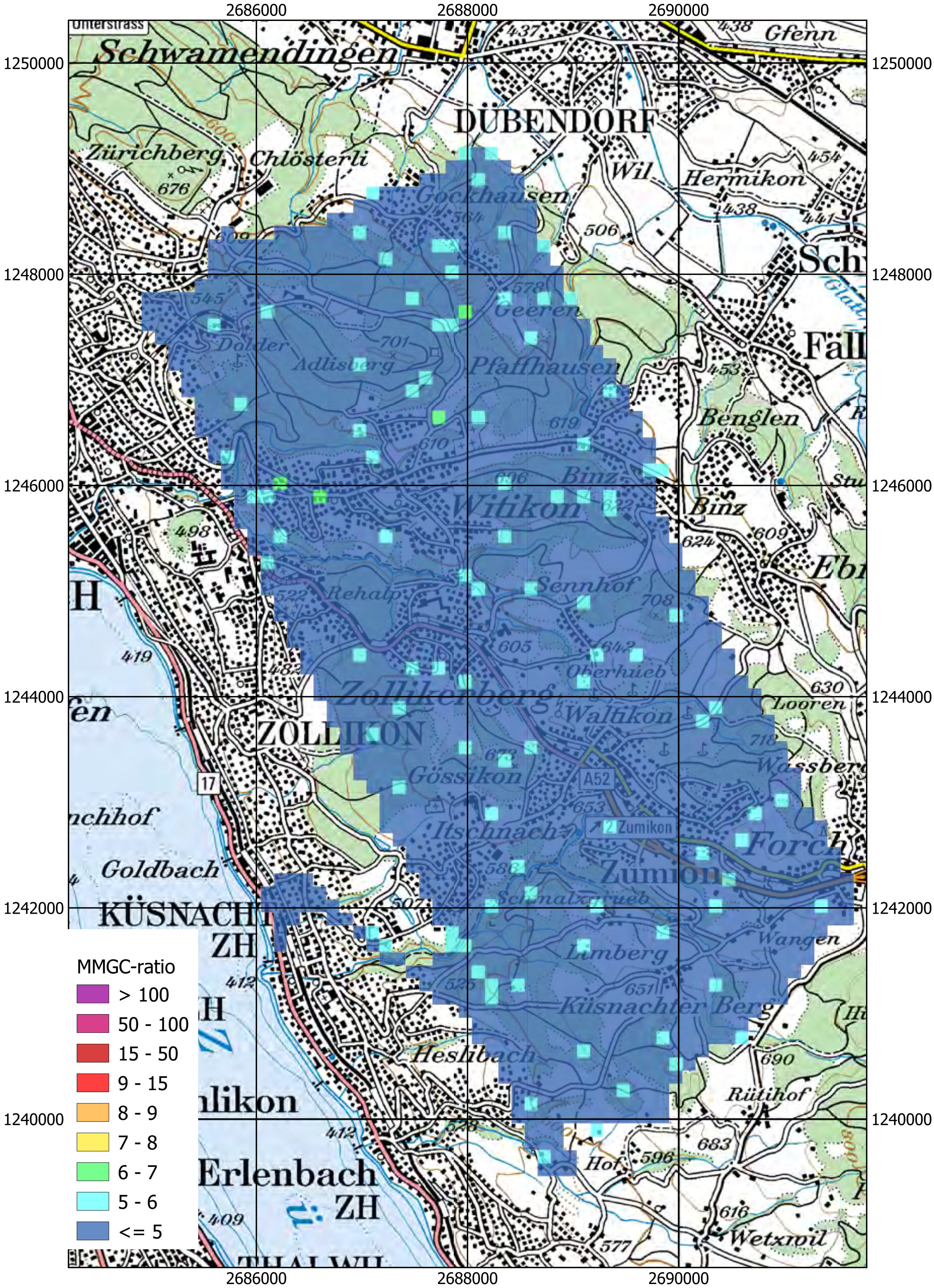

Figure 23: MMGC-ratio near Pfannenstiel-Zürichberg. Geodaten©swisstopo.

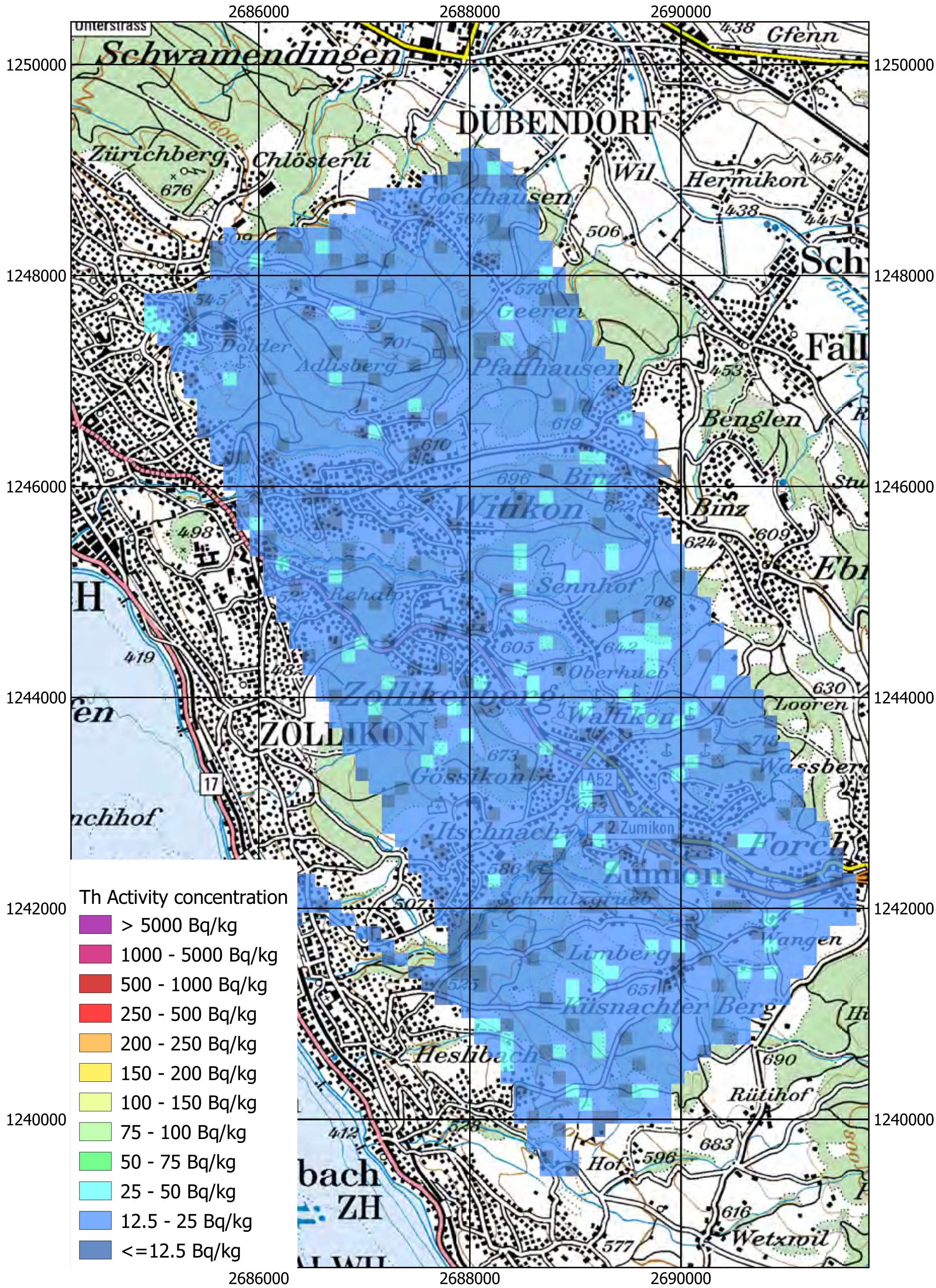

Figure 24: ^{232}Th activity concentration near Pfannenstiel-Zürichberg. Geodaten©swisstopo.

2.5 District Jura-Nord vaudois

The dose rate over the District Jura-Nord vaudois located in western Switzerland shows typical background values (Figure 25). Compensated for the altitude dependent influence of cosmic radiation, the terrestrial component of the dose rate (Figure 26) shows slightly larger values in the south-eastern corner of the measurement area. The increased dose rate correlates with elevated concentrations of the natural radionuclides (Figures 29 and 28) associated with glacial moraines (Figure 31).

A larger frequency of elevated MMGC-ratio values as indicator for the presence of man-made radionuclides is observed in the northern part of the measuring area near the border to France. This region was exposed to some deposition of radionuclides during the Chernobyl accident. The map of the ^{137}Cs activity concentration (Figure 30) shows a minor concentration increase in the area identified by the MMG-ratio map. A comparison between measured ^{137}Cs concentration values and values published in the scientific literature was presented in the report of ARM21 (Butterweck et al., 2022).

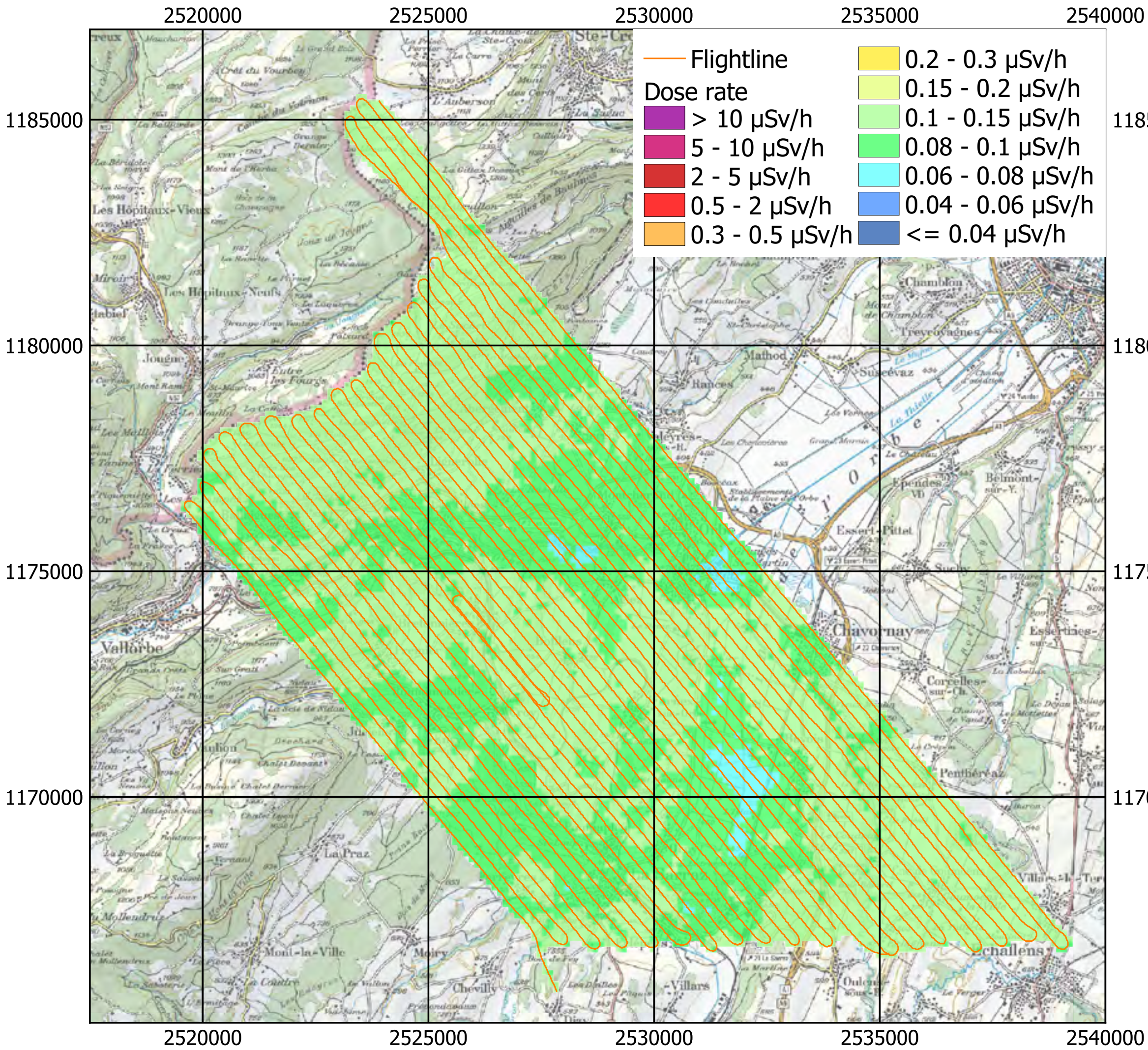

Figure 25: Dose rate over the District Jura-Nord vaudois. Geodaten©swisstopo.

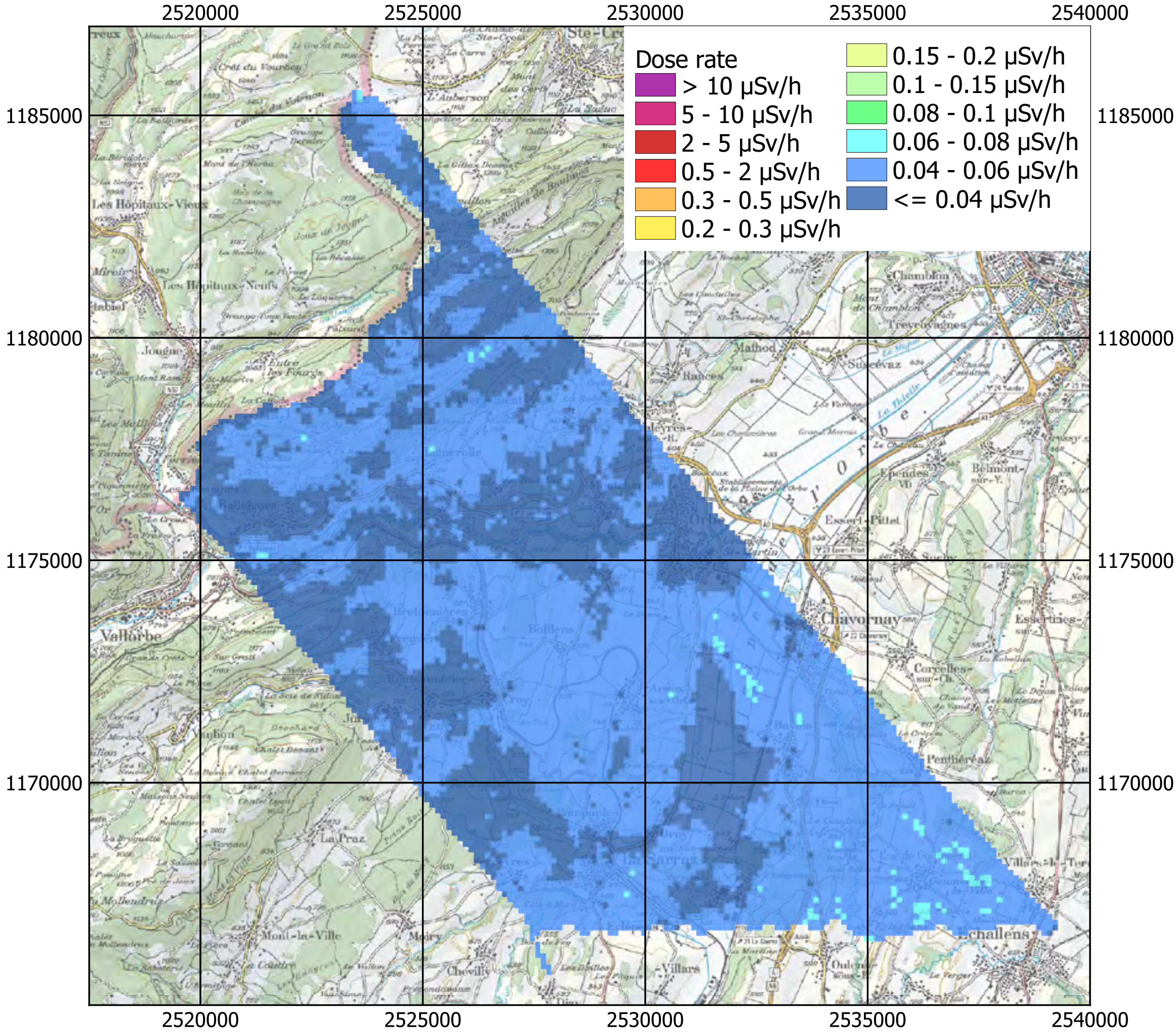

Figure 26: Terrestrial dose rate over the District Jura-Nord vaudois. Geodaten©swisstopo.

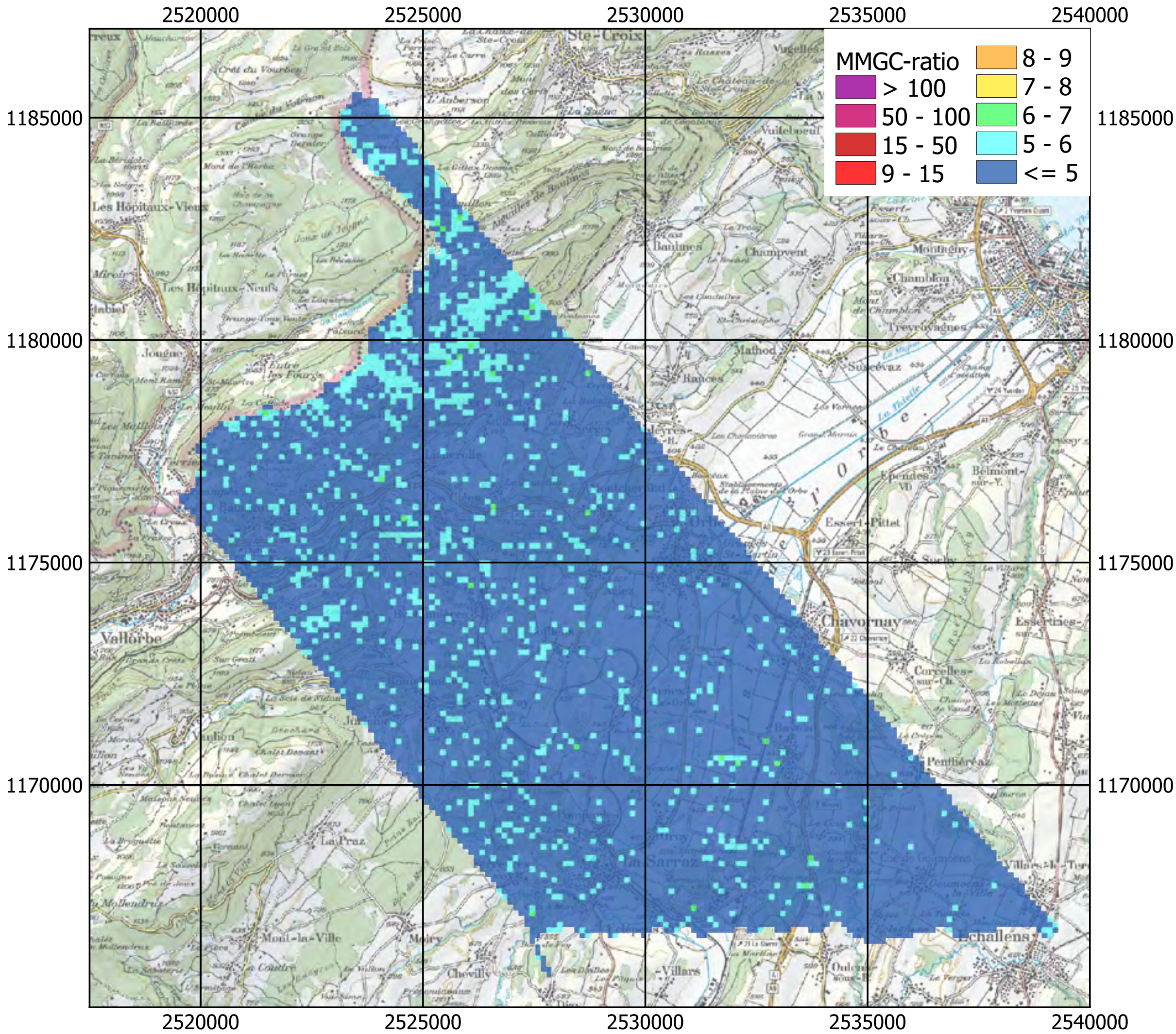

Figure 27: MMGC-ratio over the District Jura-Nord vaudois. Geodaten©swisstopo.

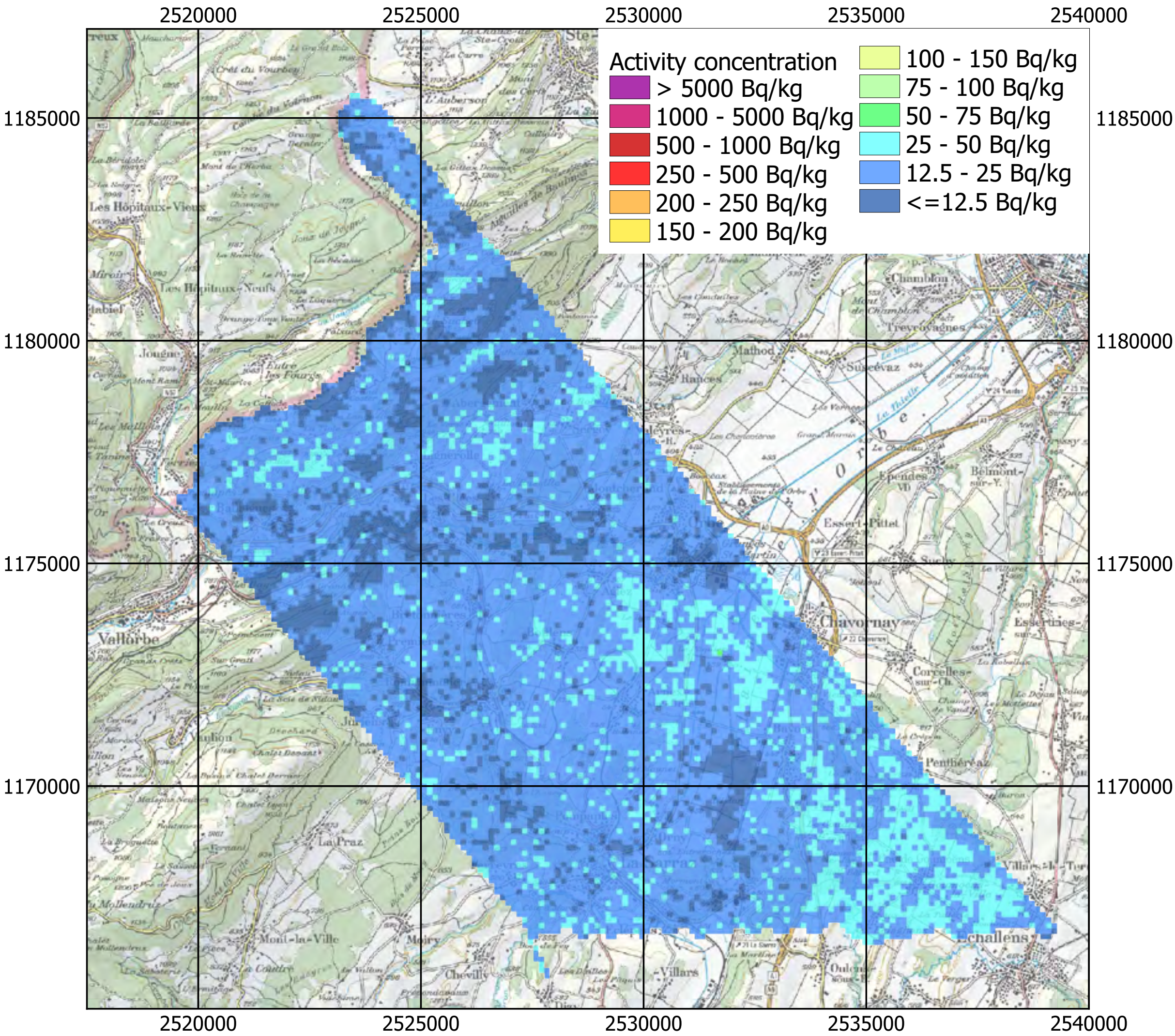

Figure 28: ^{232}Th activity concentration over the District Jura-Nord vaudois. Geodaten©swisstopo.

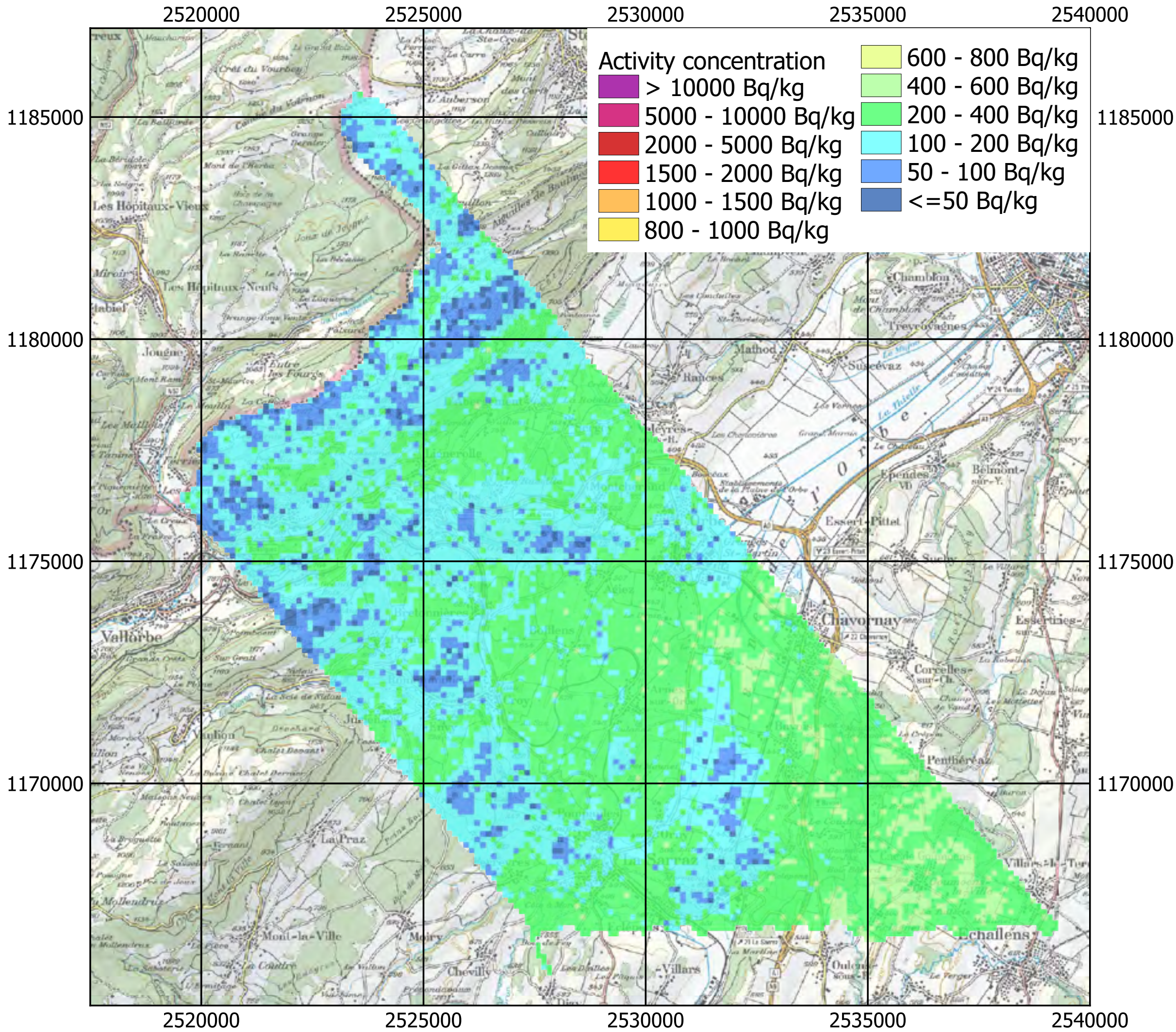

Figure 29: ^{40}K activity concentration over the District Jura-Nord vaudois. Geodaten©swisstopo.

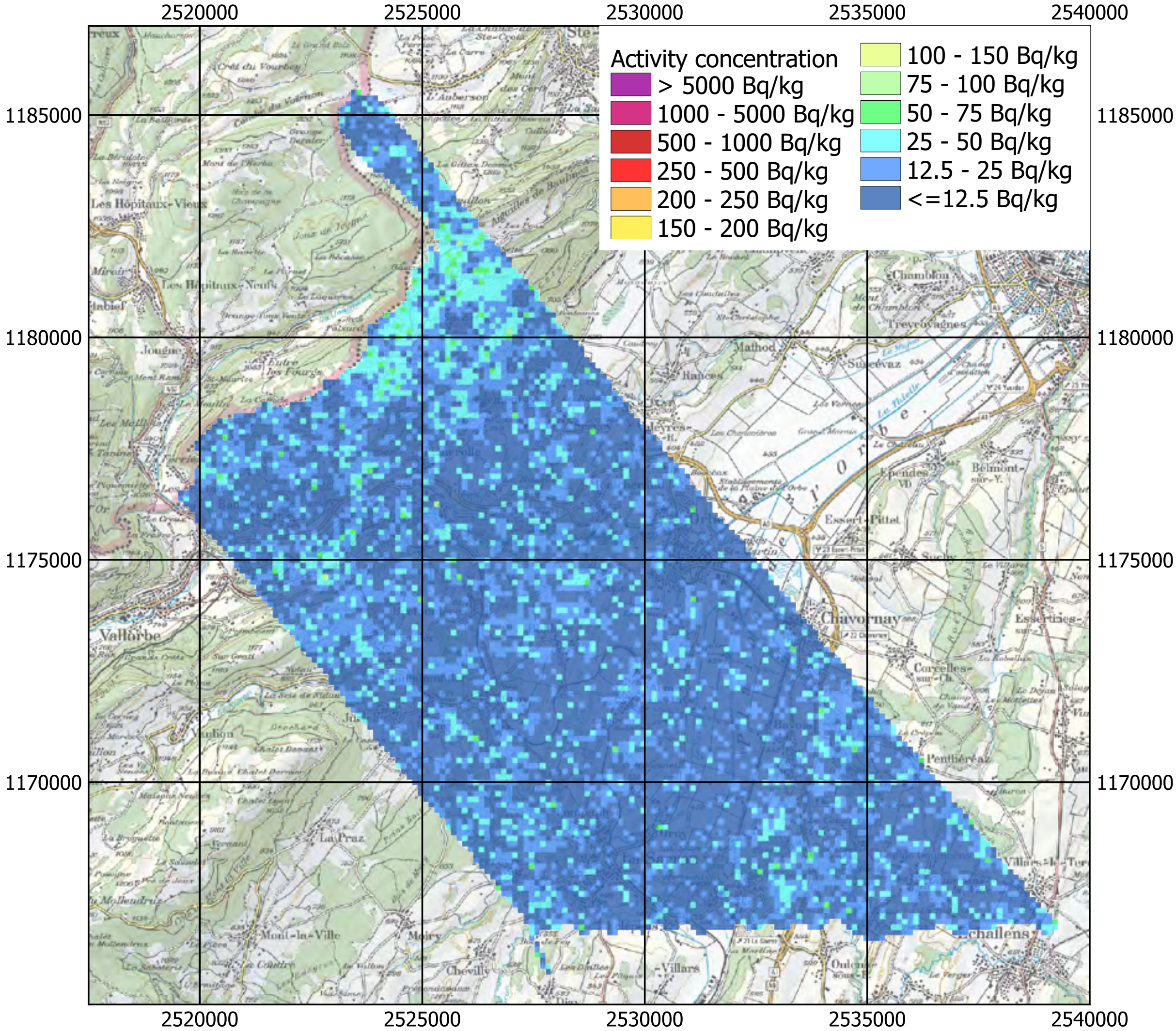

Figure 30: ^{137}Cs activity concentration over the District Jura-Nord vaudois. Geodaten©swisstopo.

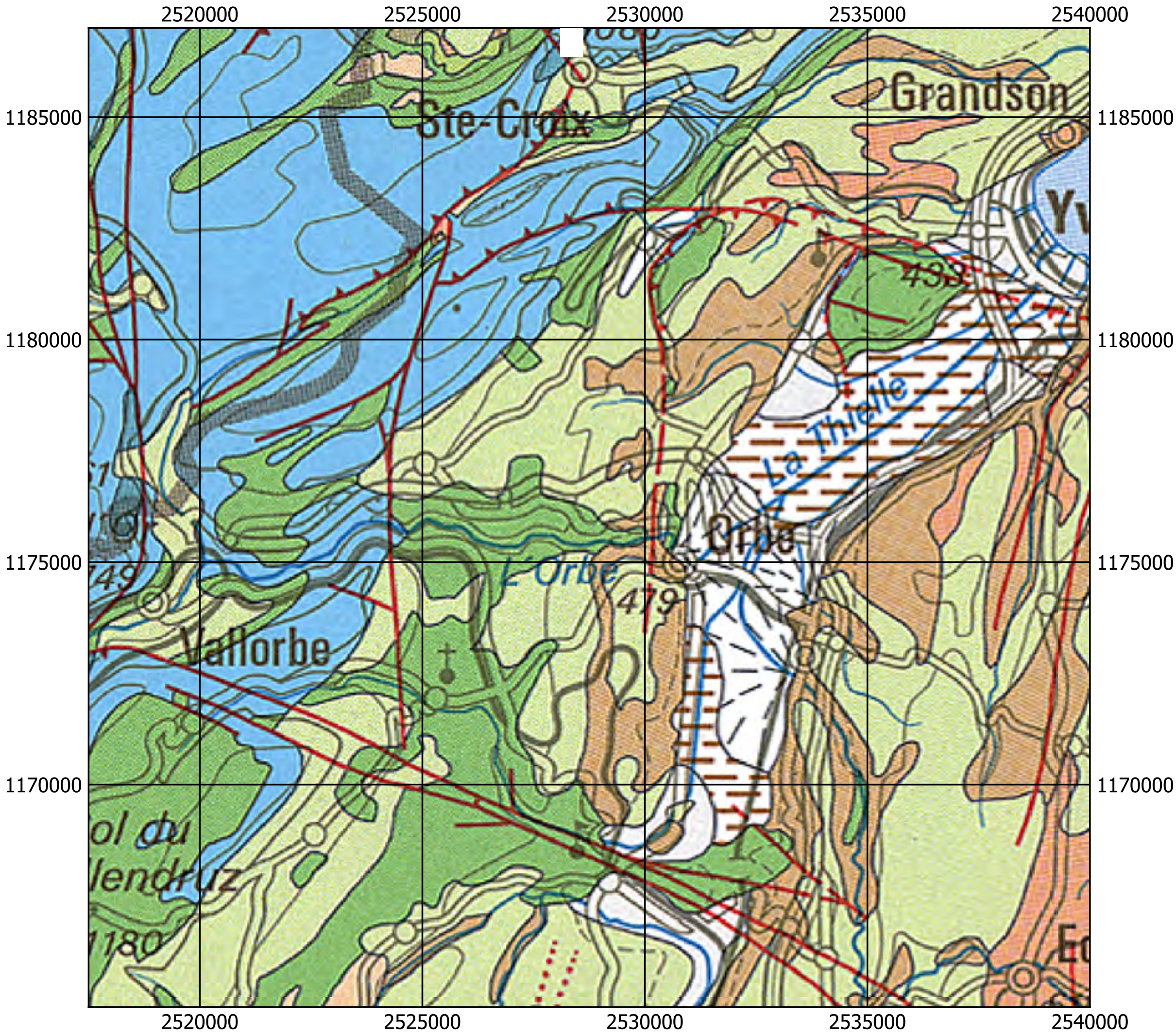

Figure 31: Geology of the District Jura-Nord vaudois. Legend see Figure 32.
Geodaten©swisstopo.

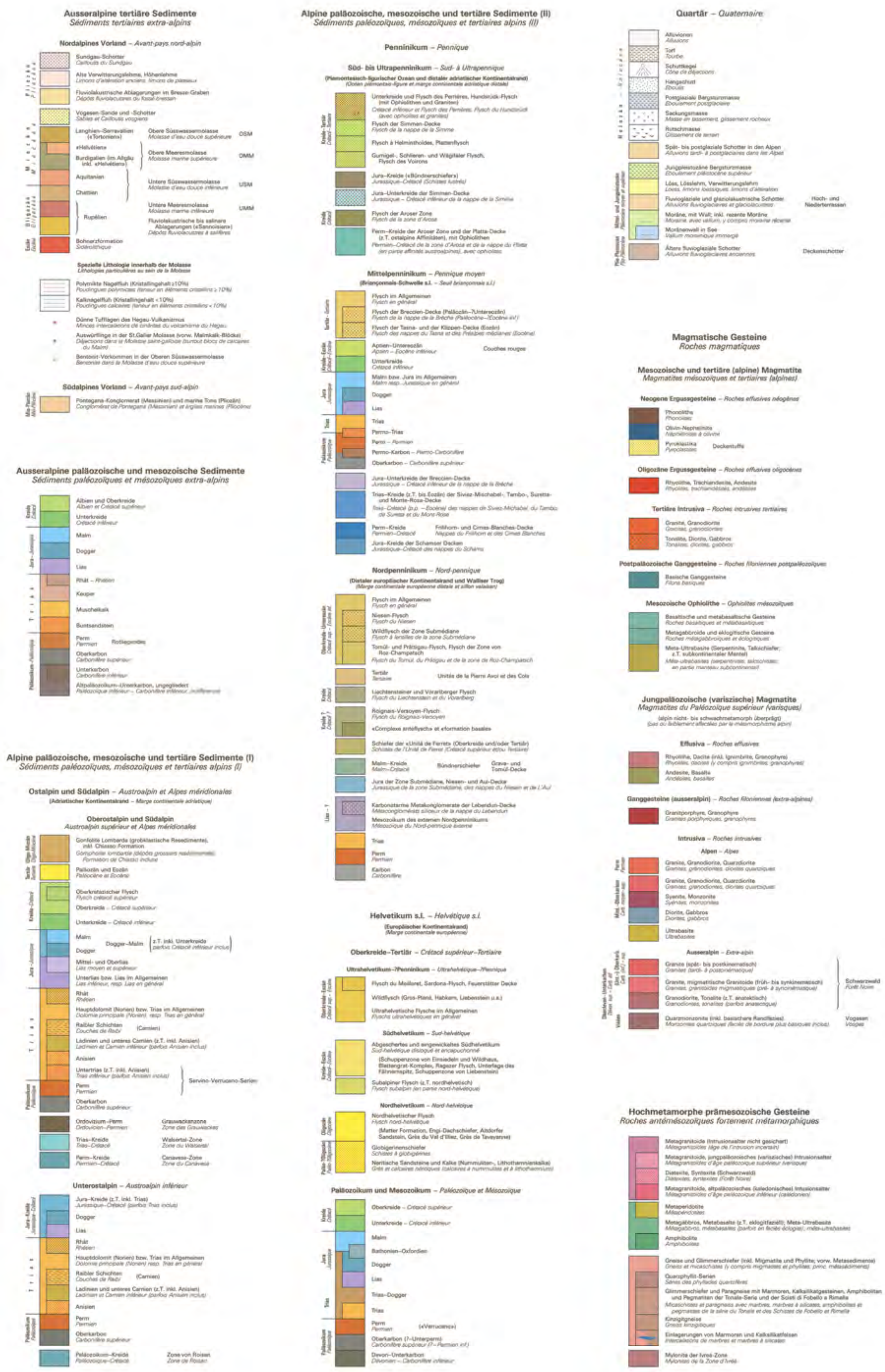

Figure 32: Legend for geological map (in German and French). Geodaten©swisstopo.

2.6 Districts Riviera and Gruyère

The maps of total dose rate (Figure 33) and the terrestrial component of the dose rate (Figure 34) show clearly the attenuation of gamma rays emitted by terrestrial radionuclides due to the water layer of Lake Geneva. The map of the MMGC-ratio (Figure 35) does not indicate any presence of man-made radionuclides. Dose rate increases in the northern part of the measured area and the eastern shore of Lake Geneva can be attributed to increased activity concentrations of the natural radionuclide ^{40}K (Figure 37), whereas areas with elevated activity concentrations of ^{232}Th (Figure 36) are unobtrusive in respect to dose rate. The elevated potassium concentrations in the northern part of the measuring area overlap with coal-bearing molasses, whereas the elevated readings directly at the eastern shore of Lake Geneva are associated with alluvial deposits (Figure 38).

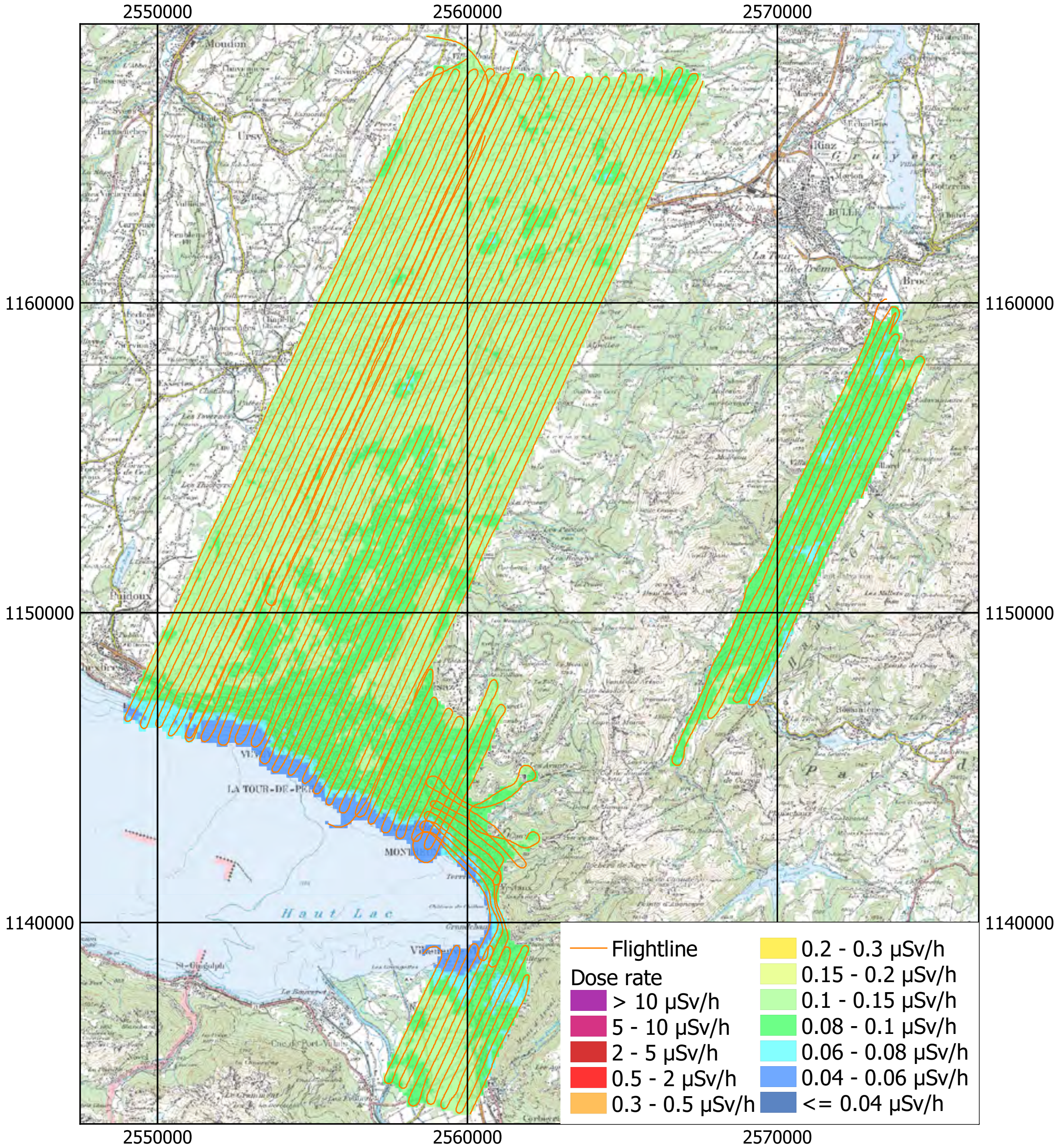

Figure 33: Dose rate in the Districts Riviera and Gruyère. Geodaten©swisstopo.

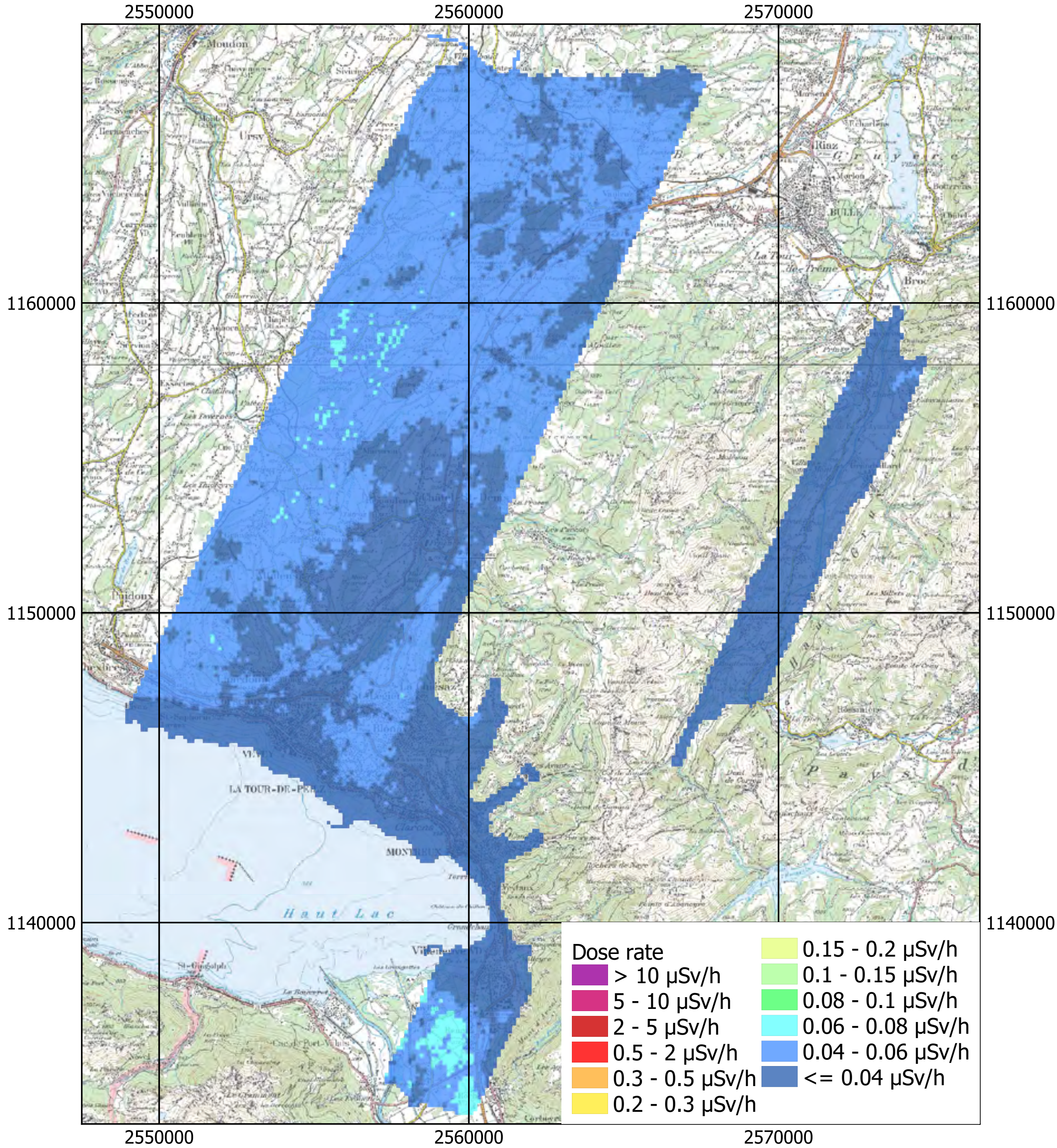

Figure 34: Terrestrial dose rate in the Districts Riviera and Gruyère. Geodaten©swisstopo.

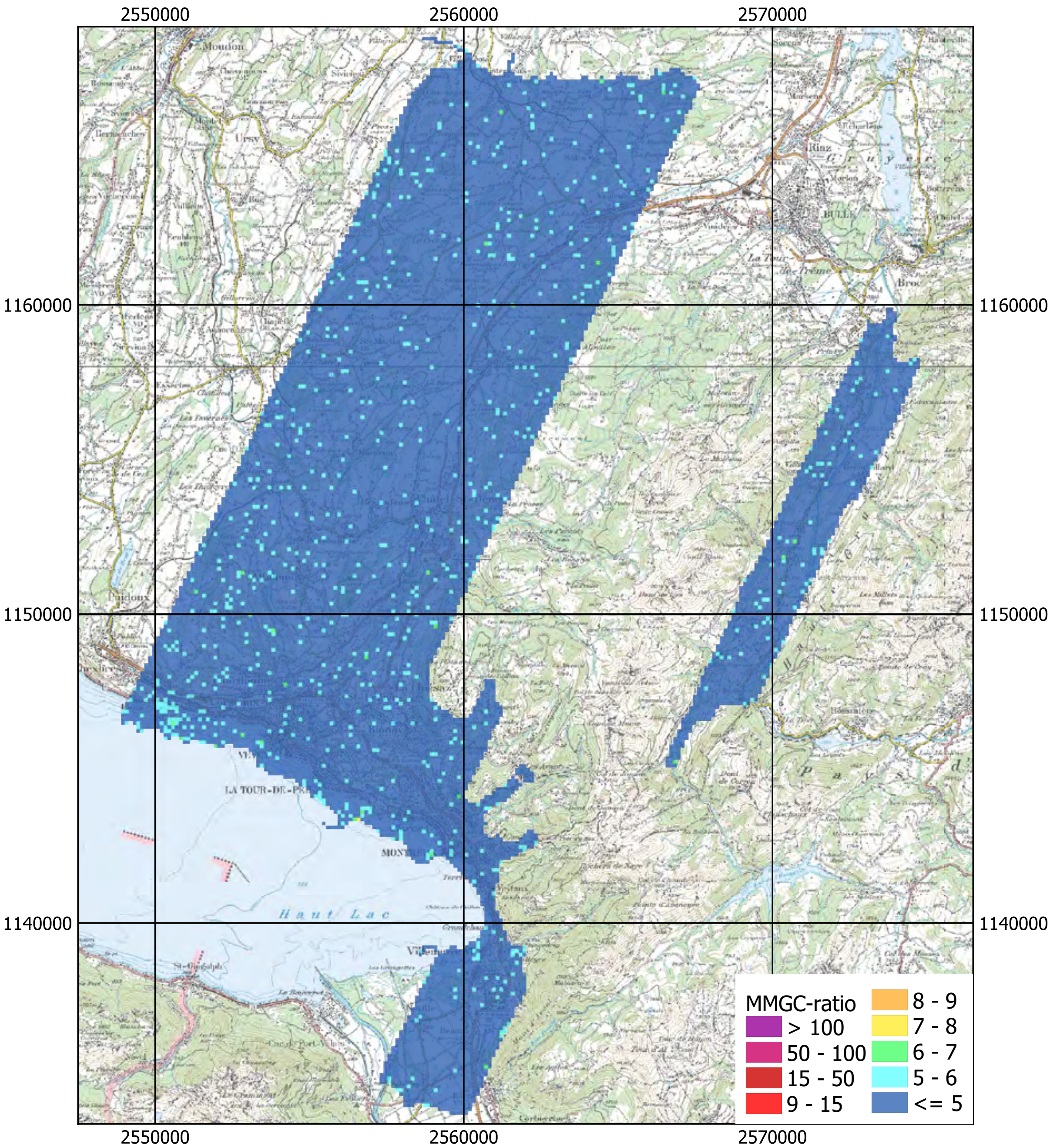

Figure 35: MMGC-ratio in the Districts Riviera and Gruyère. Geodaten©swisstopo.

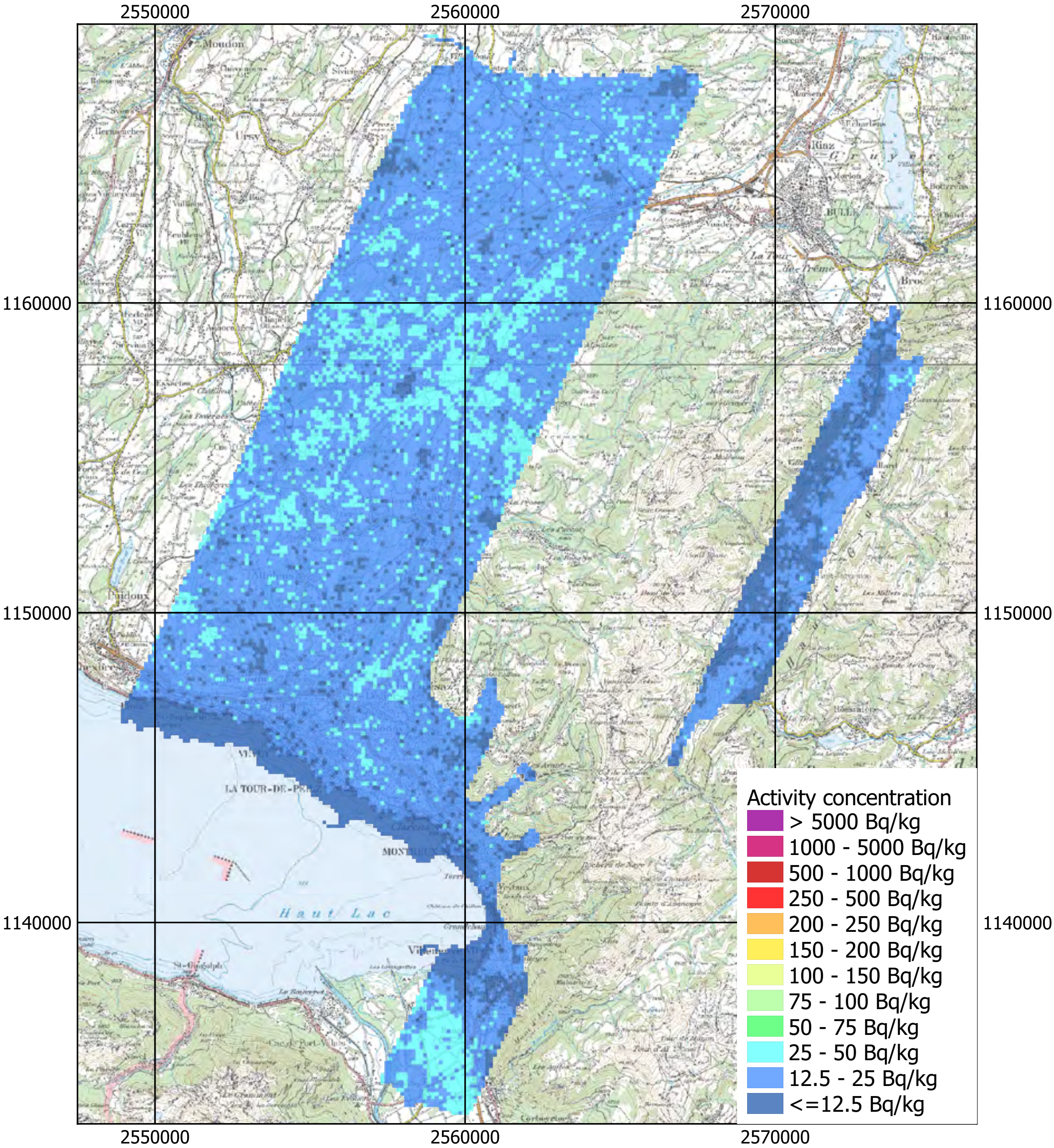

Figure 36: ^{232}Th activity concentration in the Districts Riviera and Gruyère. Geodaten©swisstopo.

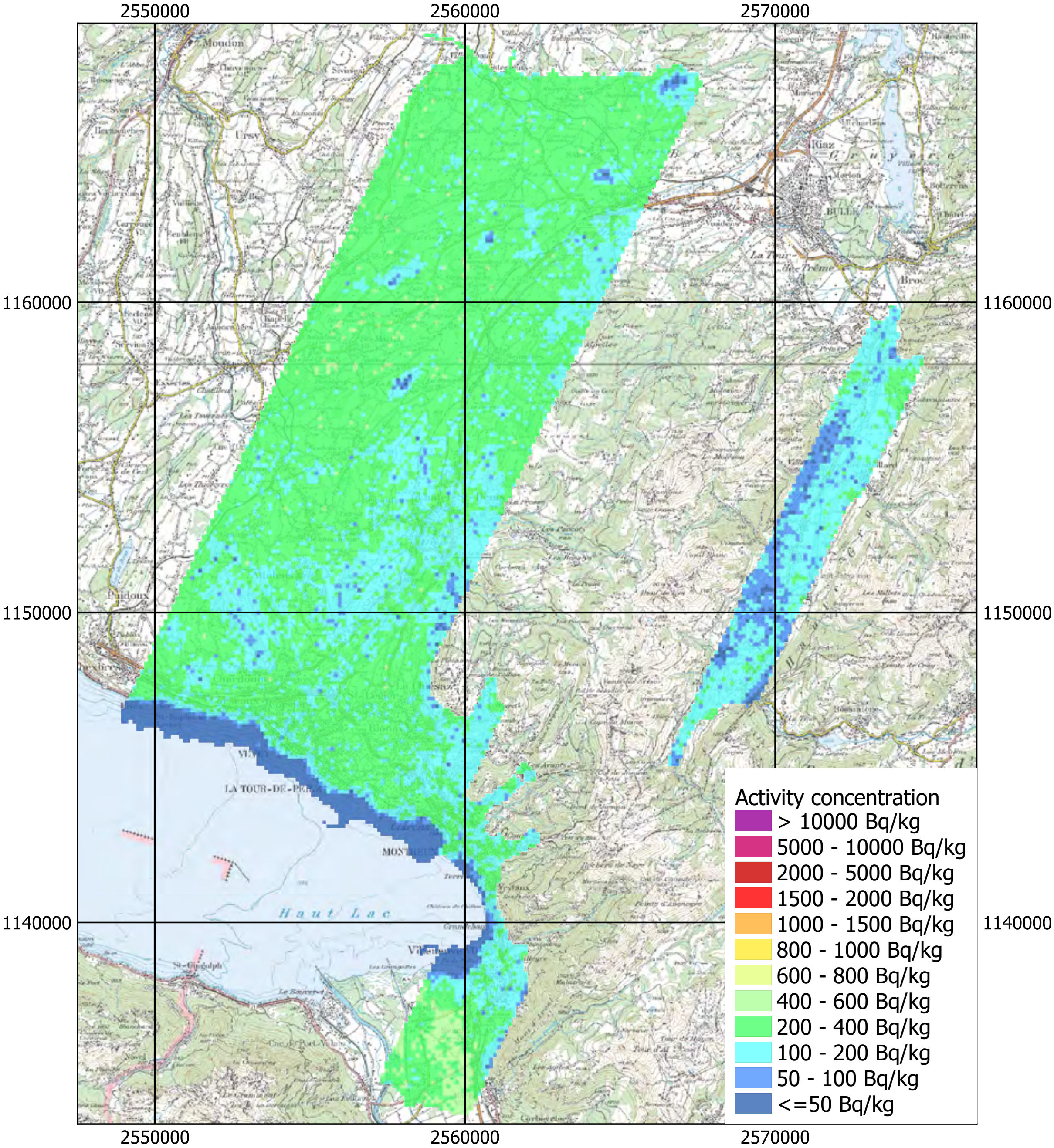

Figure 37: ^{40}K activity concentration in the Districts Riviera and Gruyère. Geodaten©swisstopo.

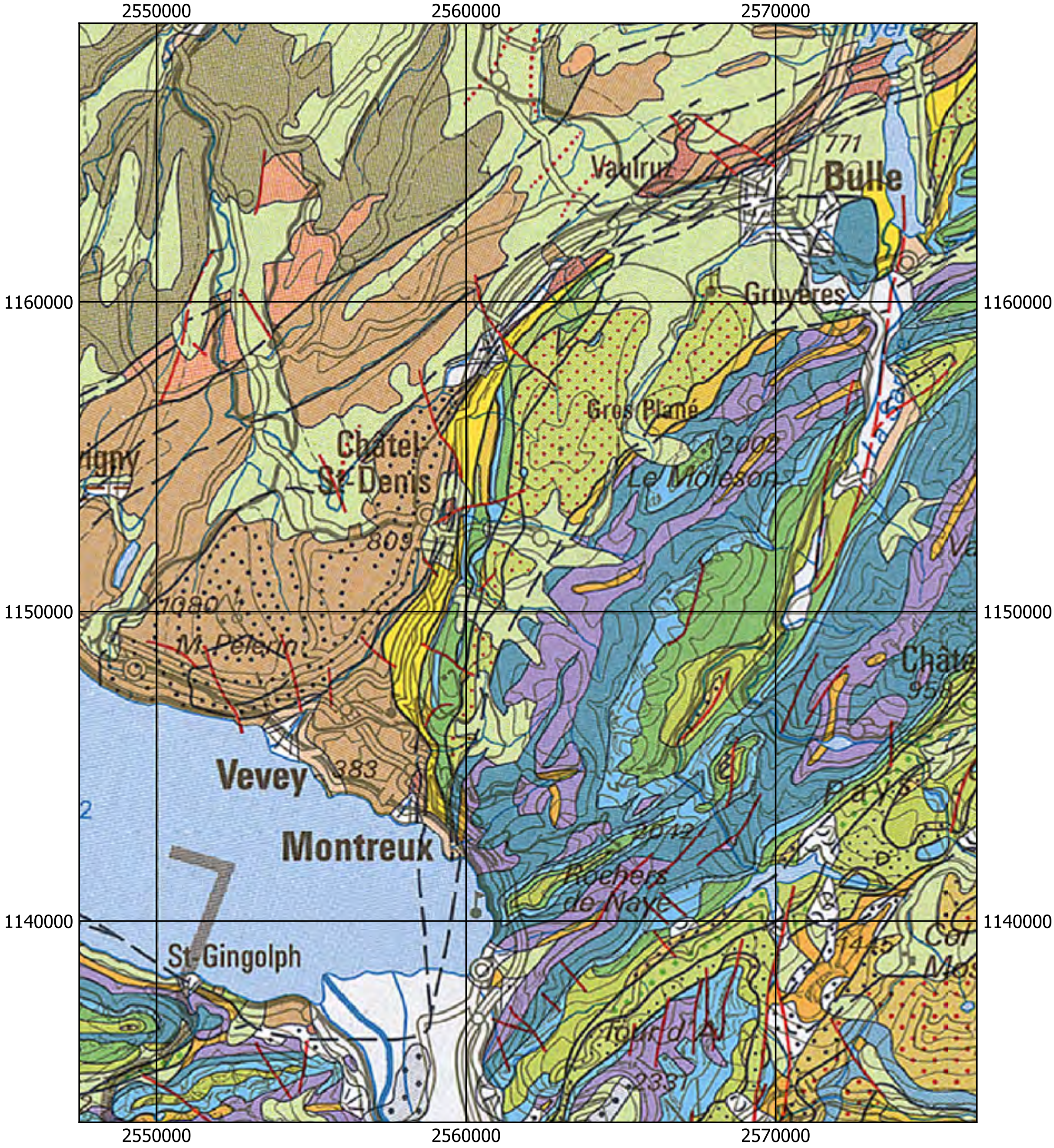

Figure 38: Geology in the Districts Riviera and Gruyère. Legend see Figure 32. Geodaten©swisstopo.

2.7 Districts Broye et Glâne

Maps of the dose rate (Figure 39), MMGC-ratio (Figure 40) and the ^{232}Th activity concentration (Figure 41) in the measurement area depict unremarkable readings. The former site of the Lucens reactor (Wildi, 2003), which was given up after a partial core melt in 1969 and completely decommissioned in 2003, does not stand out in the radiological maps. Previous airborne measurements over this site are documented in the reports of the exercises in 1999, 2000, 2001 and 2004 (Bucher et al. 2000, 2001, 2002 and 2005).

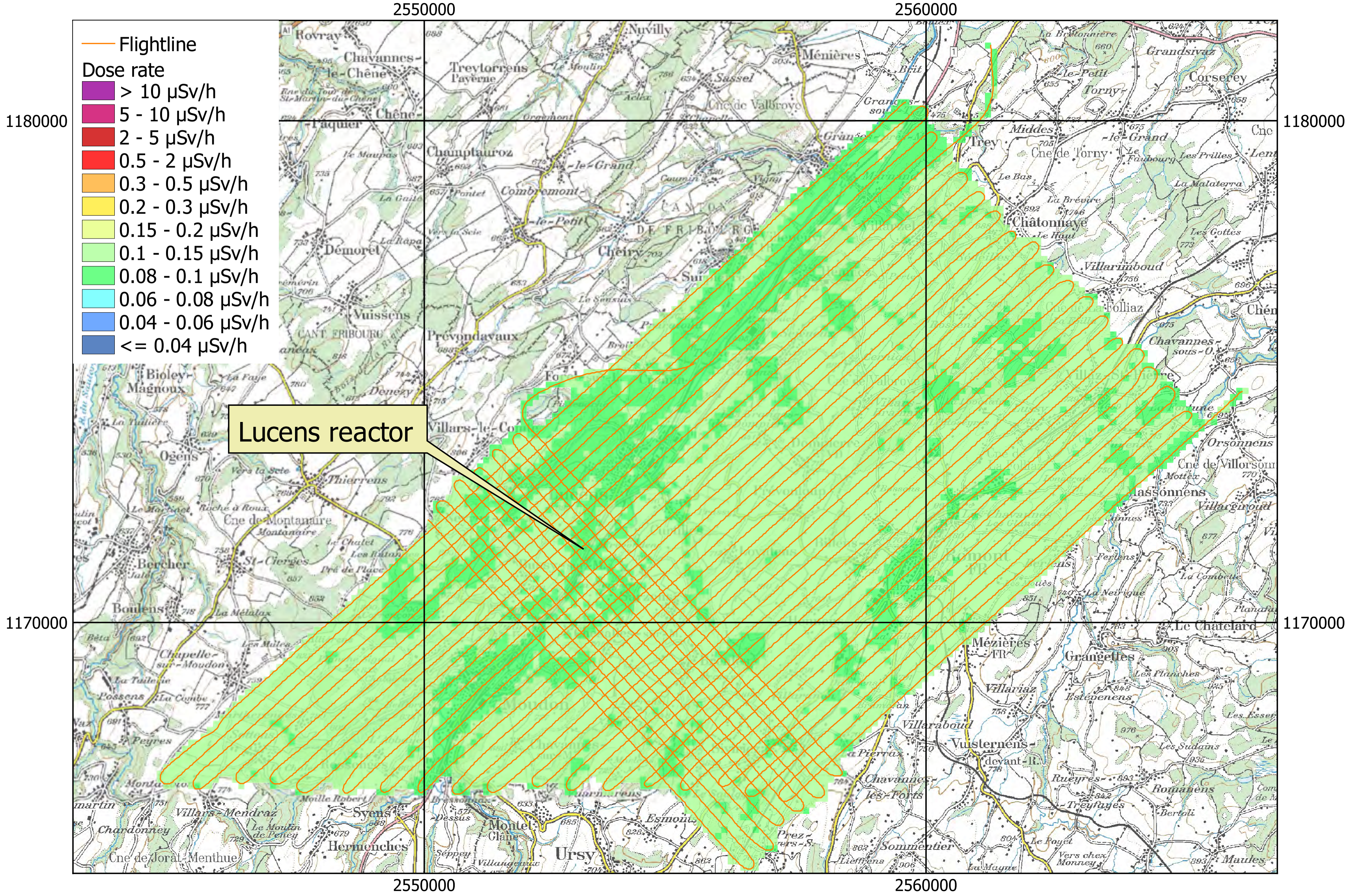

Figure 39: Dose rate in the Districts Broye et Glâne. Geodaten©swisstopo.

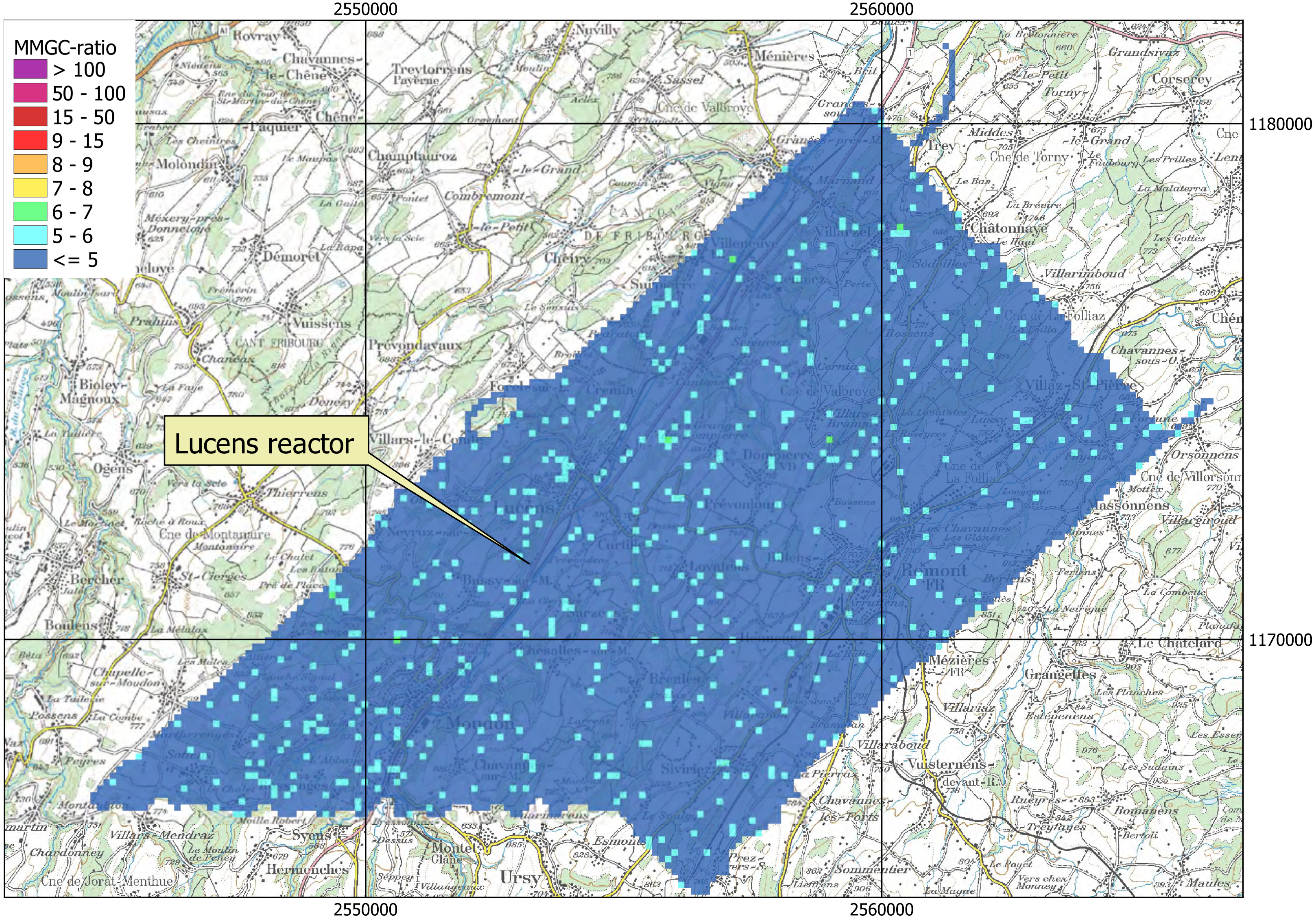

Figure 40: MMGC-ratio in the Districts Broye et Glâne. Geodaten©swisstopo.

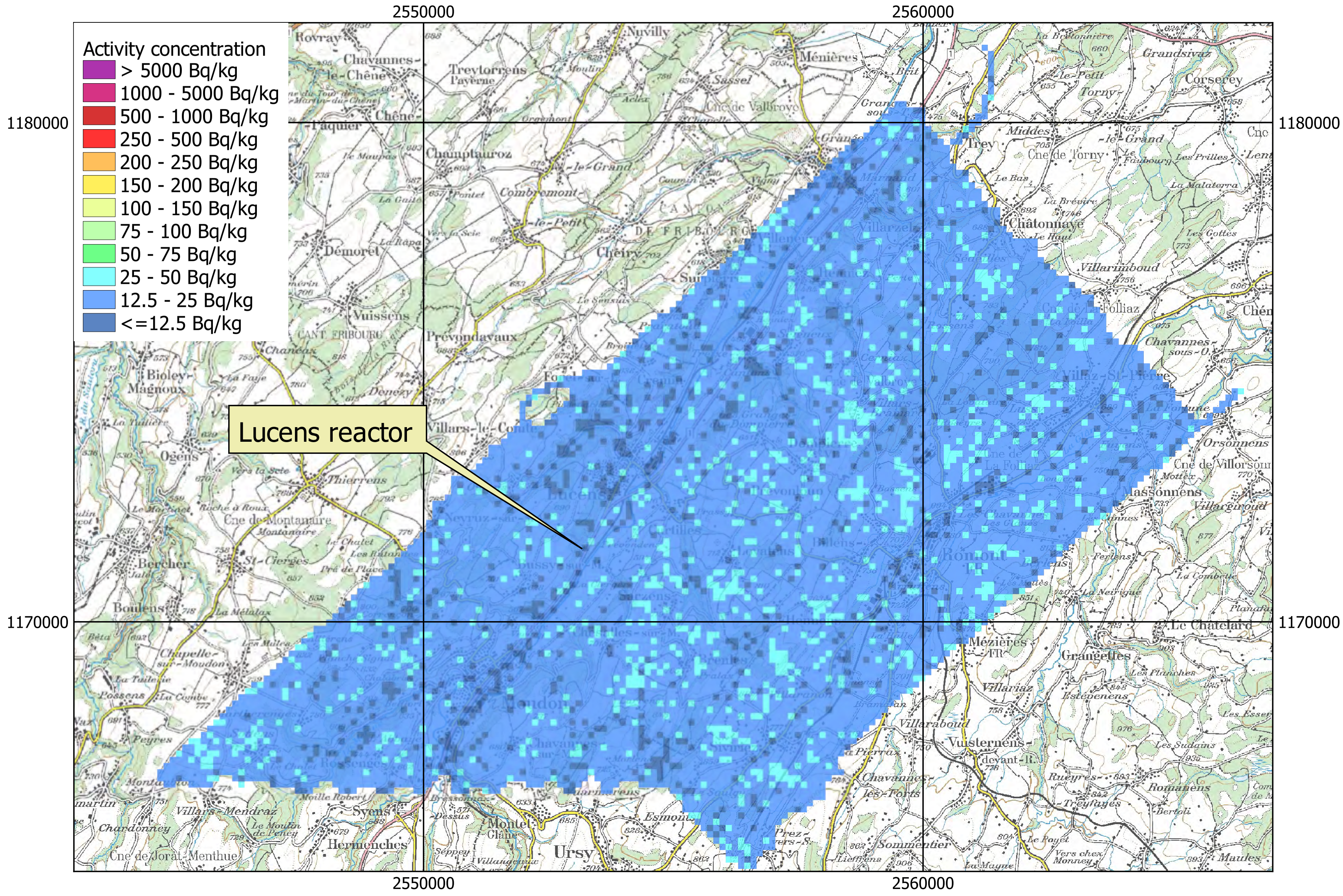

Figure 41: ^{232}Th activity concentration in the Districts Broye et Glâne. Geodaten©swisstopo.

2.8 Val de Travers

The Val de Travers, located to the west of Lake Neuchâtel, shows typical values of dose rates in Switzerland (Figure 42). Corrected for the altitude dependent influence of cosmic radiation, the terrestrial dose rate component depicts slightly elevated values in the northern part of the measuring area (Figure 43). The map of the MMGC-ratio (Figure 44) does not indicate the presence of man-made radionuclides in this part of the measuring area. A single point with a marginally elevated MMGC-ratio at coordinate (2543869, 1201317) could be rated as artefact caused by a unusually low count rate of high energy photons. Both maps of natural radionuclides ^{232}Th (Figure 45) and ^{40}K (Figure 46) reflect the pattern observed in the terrestric dose rate, matching a geological layer from the Aquitanian stage (Figure 47).

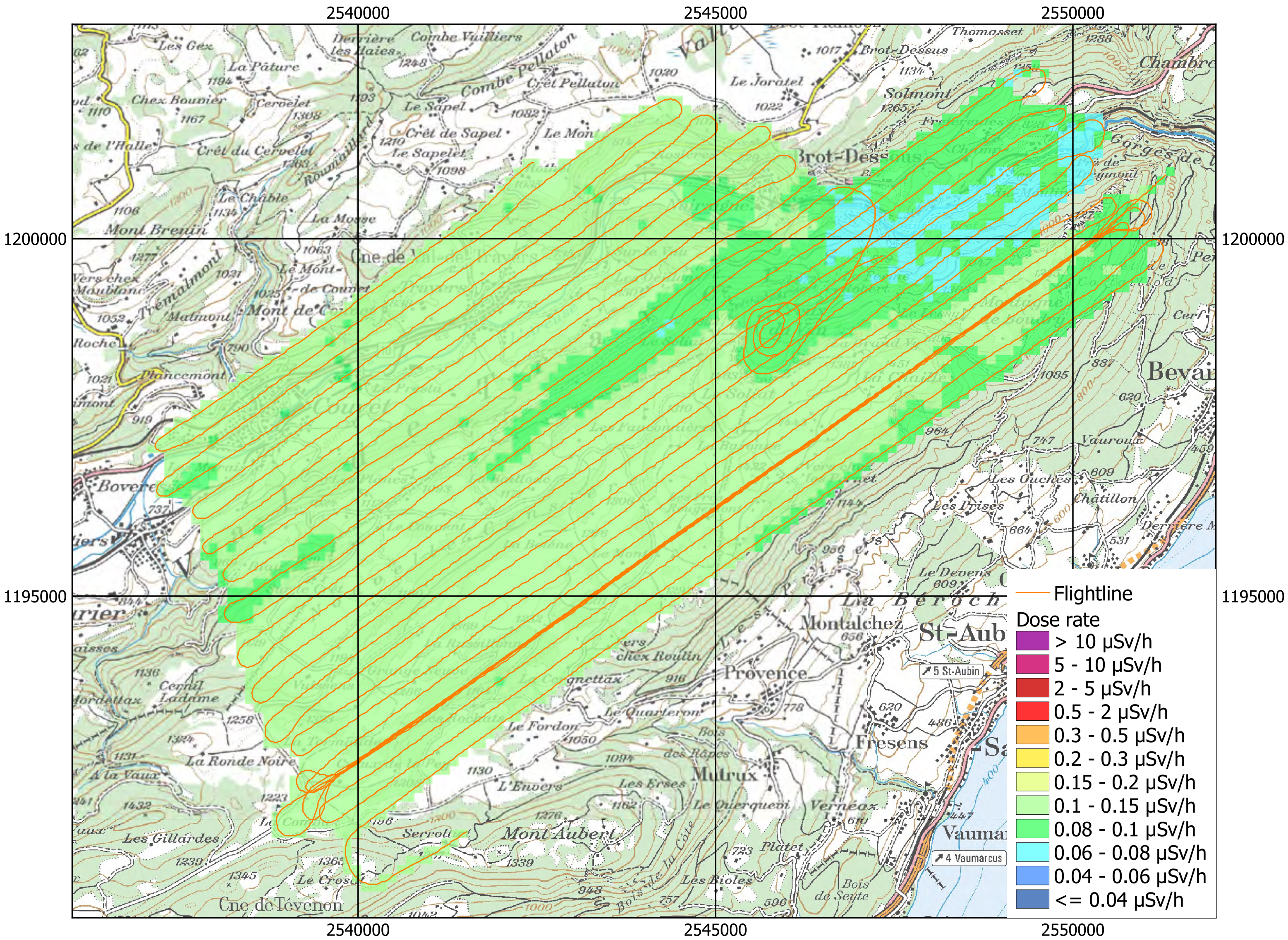

Figure 42: Dose rate over the Val de Travers. Geodaten©swisstopo.

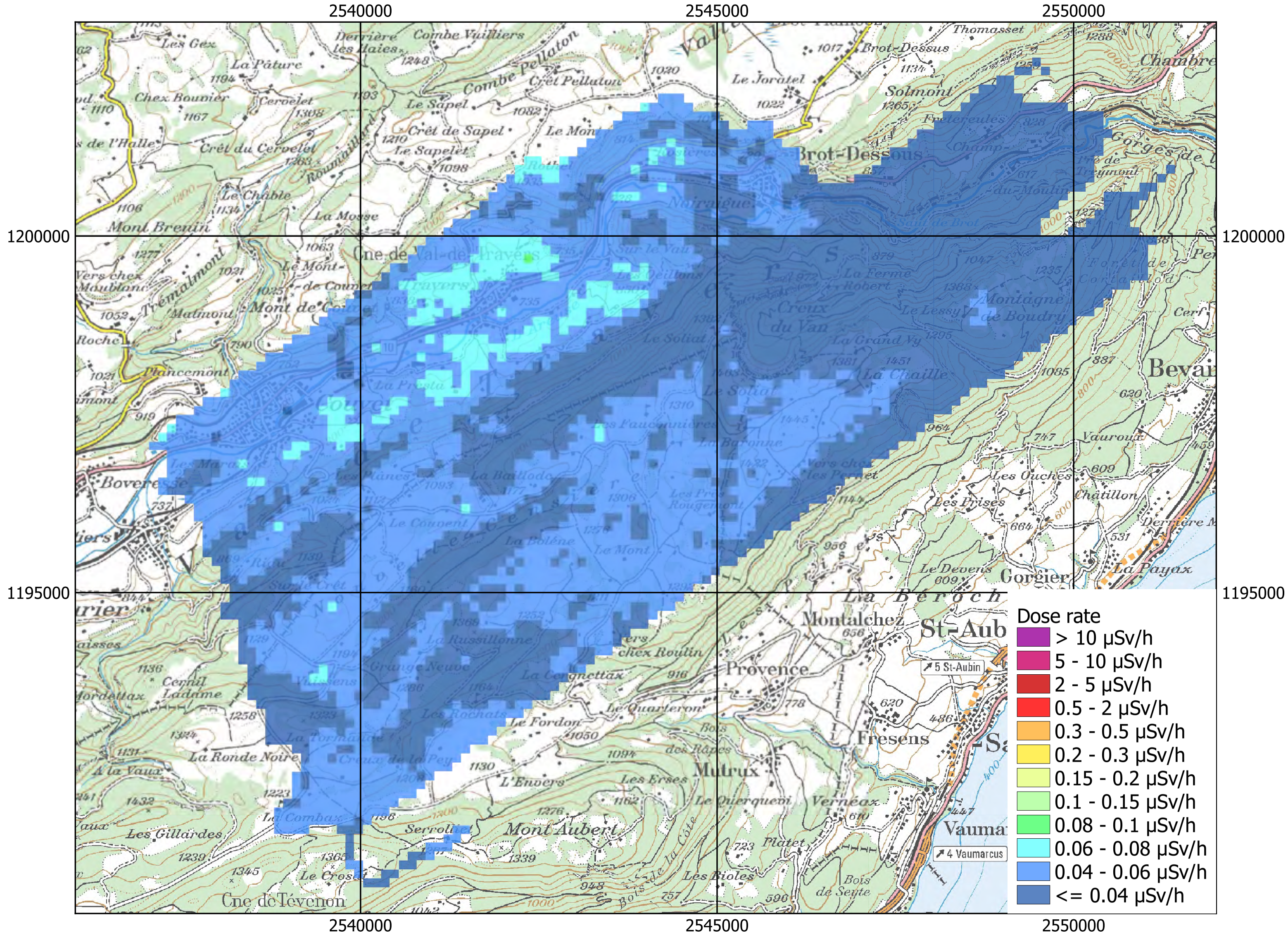

Figure 43: Terrestrial dose rate over the Val de Travers. Geodaten©swisstopo.

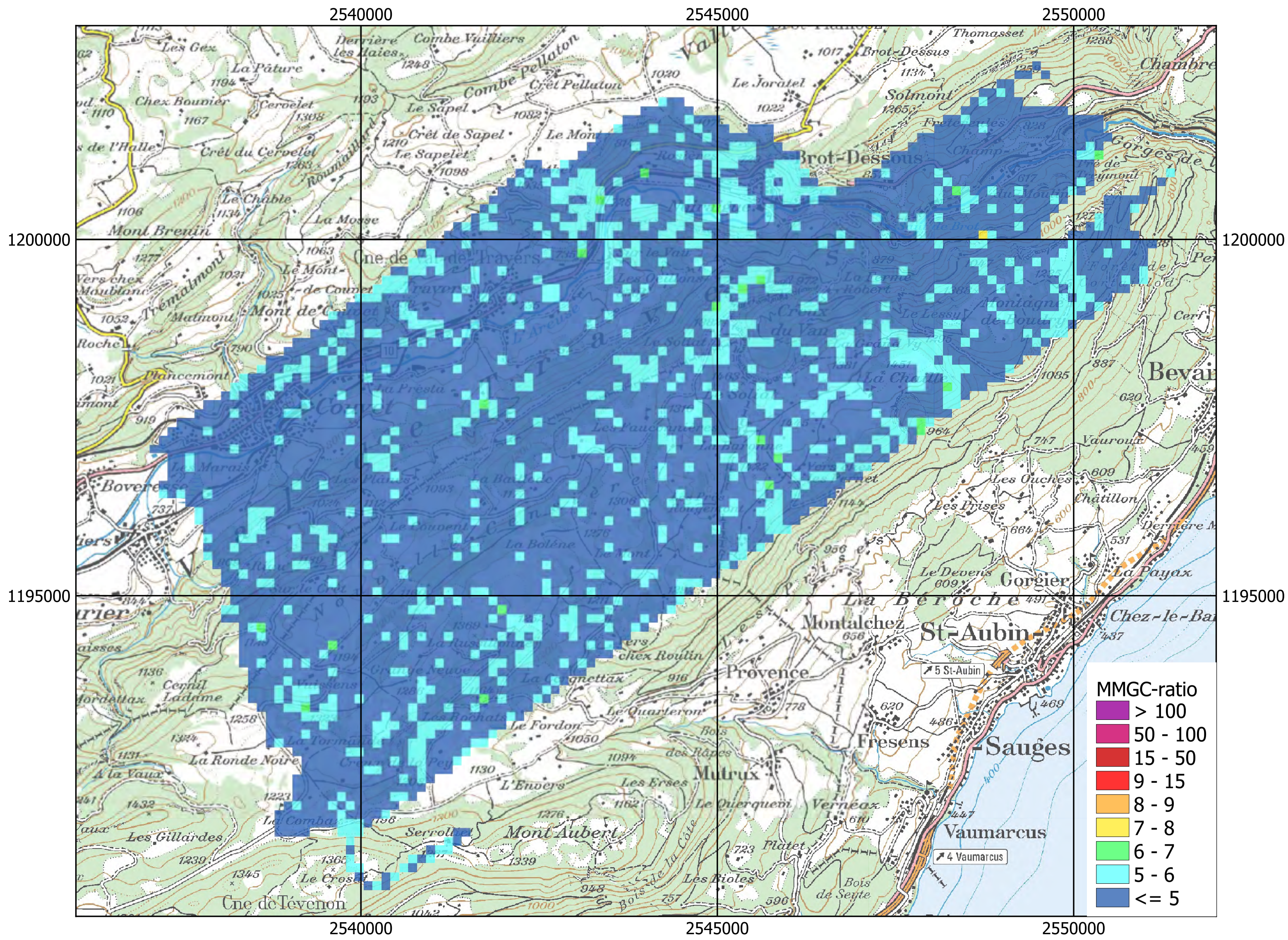

Figure 44: MMGC-ratio over the Val de Travers. Geodaten©swisstopo.

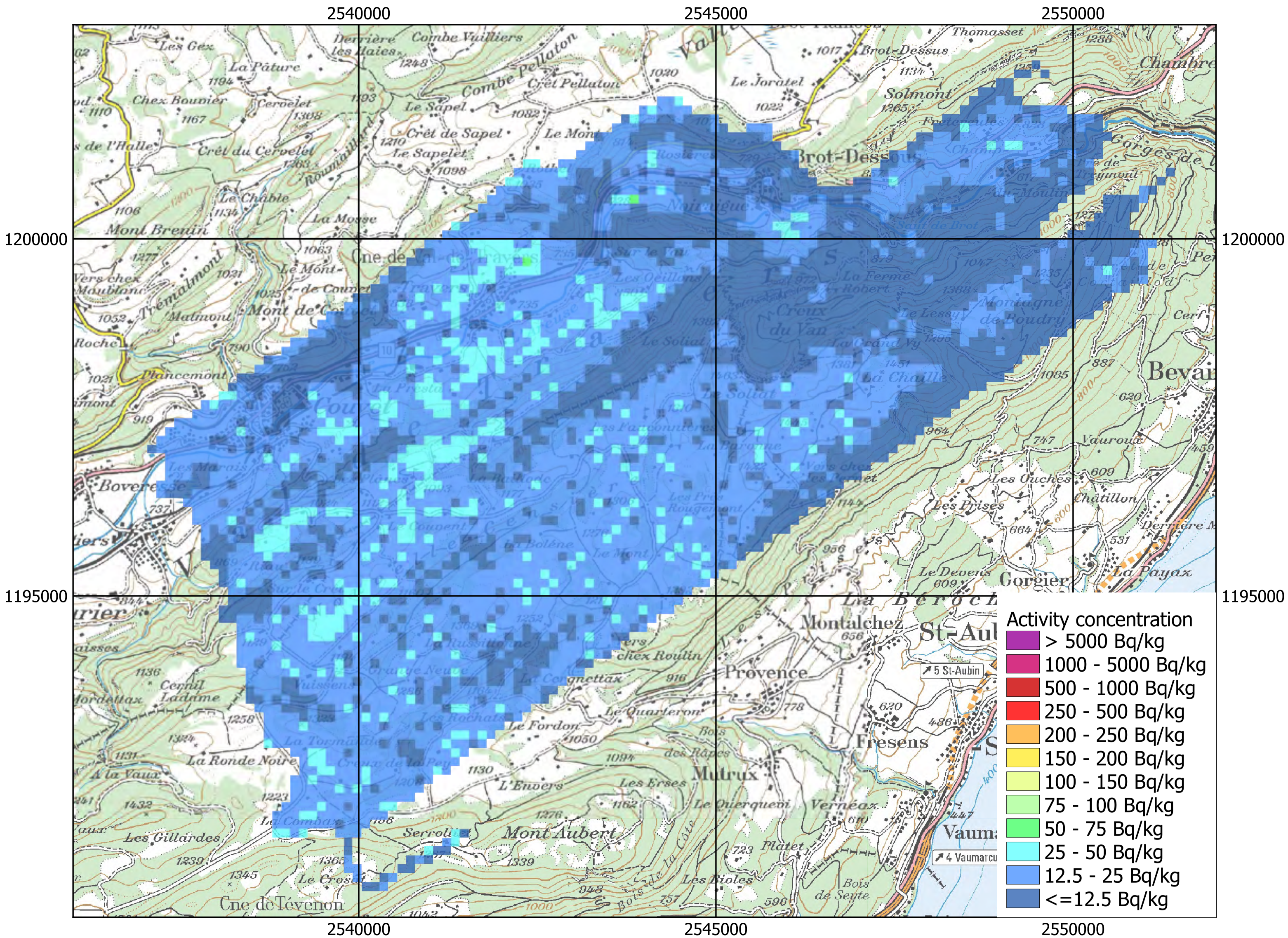

Figure 45: ^{232}Th activity concentration over the Val de Travers. Geodaten©swisstopo.

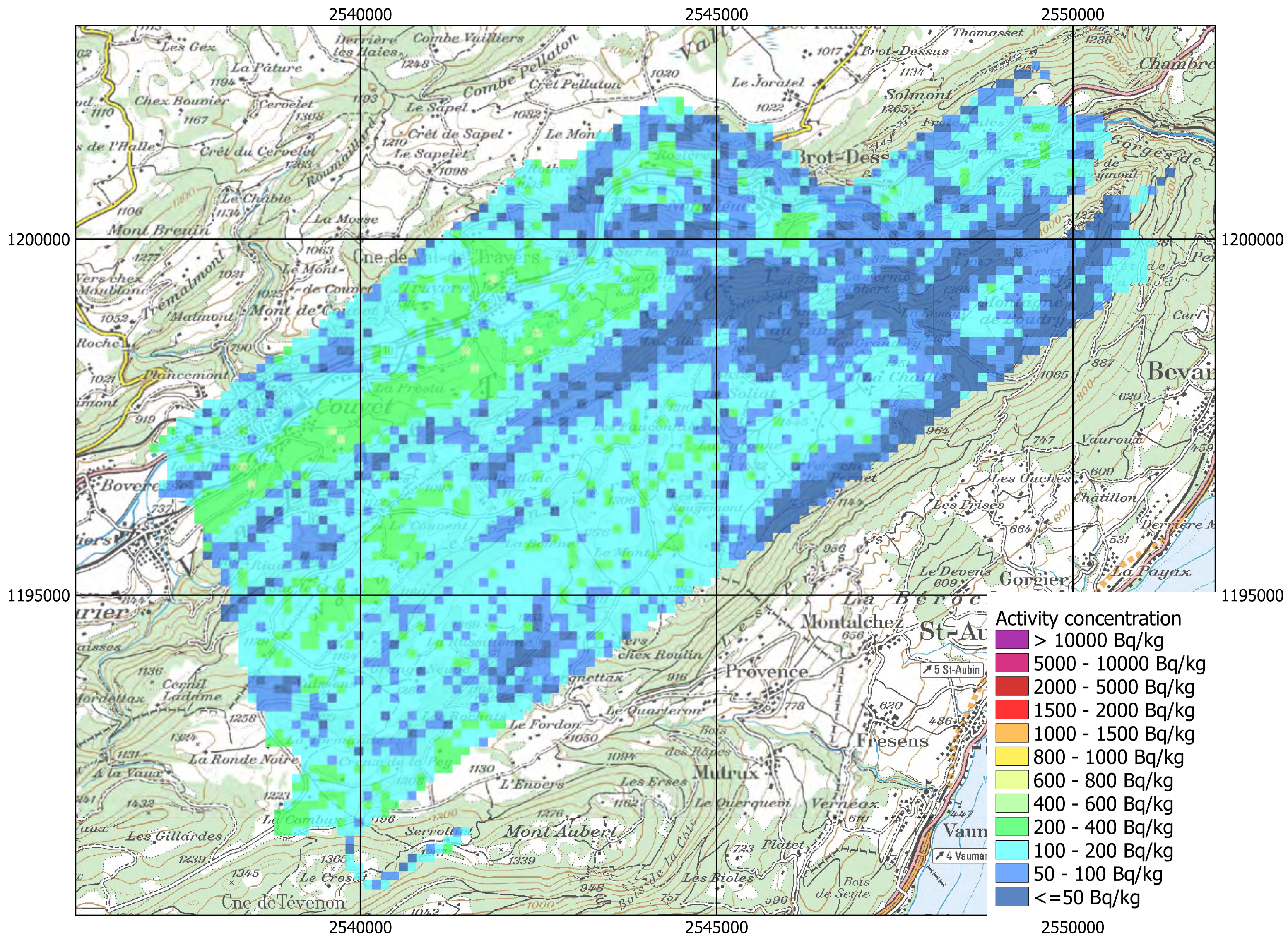

Figure 46: ^{40}K activity concentration over the Val de Travers. Geodaten©swisstopo.

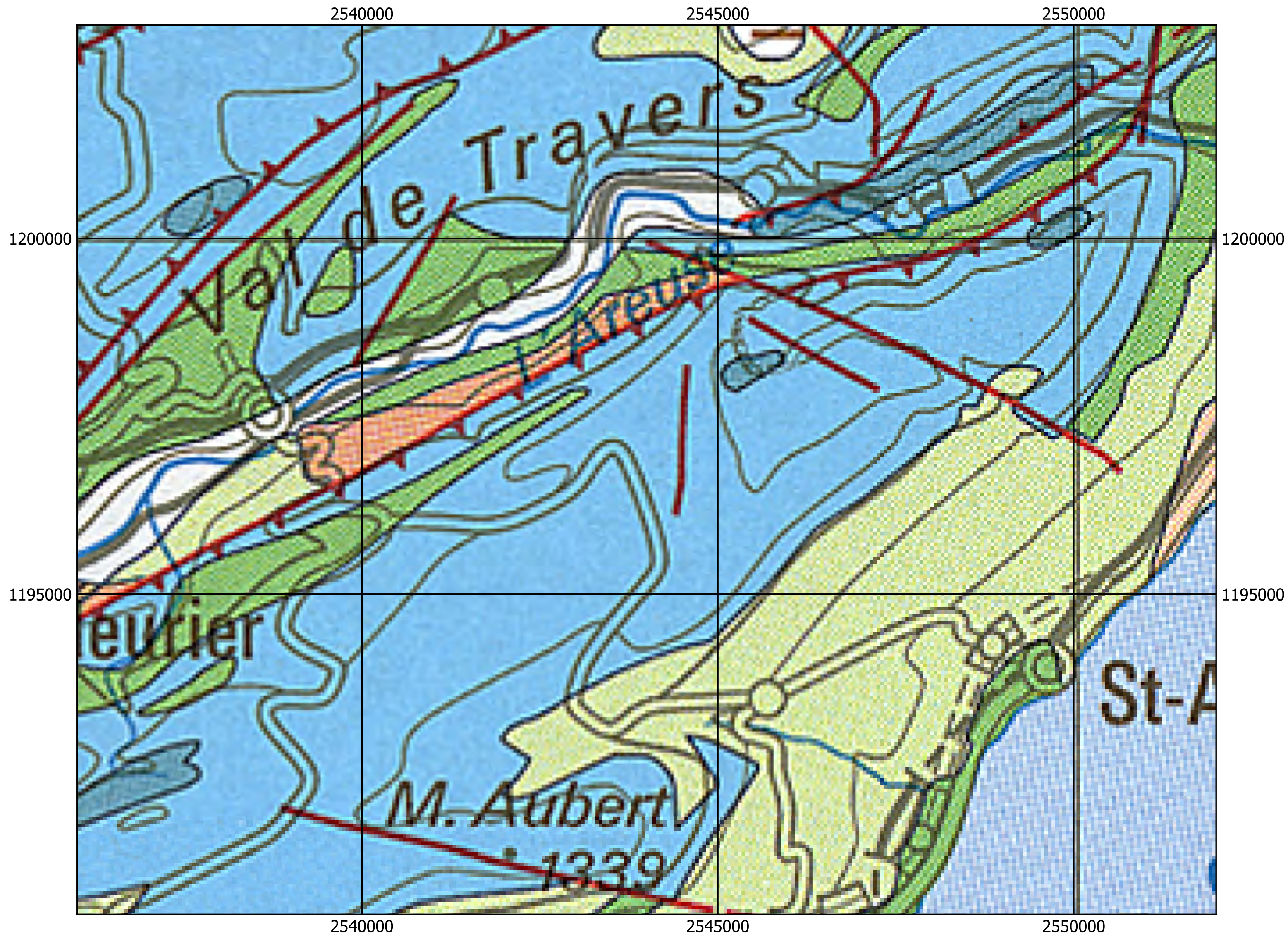

Figure 47: Geology of the Val de Travers. Legend see Figure 32. Geodaten©swisstopo.

2.9 Alpine valleys

The three alpine valleys Rheinwald, Misox and Val Calanca were surveyed during one flight of ARM22c together with the connecting San Bernadino pass. The flightline (Figure 48) starts in the north-east, follows the Rheinwald via San Bernadino pass into Misox and Val Calanca. A second flight inspected an area in the Weisstannental, where an uranium hotspot was reported in the past. The geological maps (Figures 49 and 77) display chalk, limestone and slide-rock in the valleys and granites and granodiorites in the adjacent mountains. The reported uranium hotspot in the Weisstannental is located at the border between Permian and Cretaceous layers.

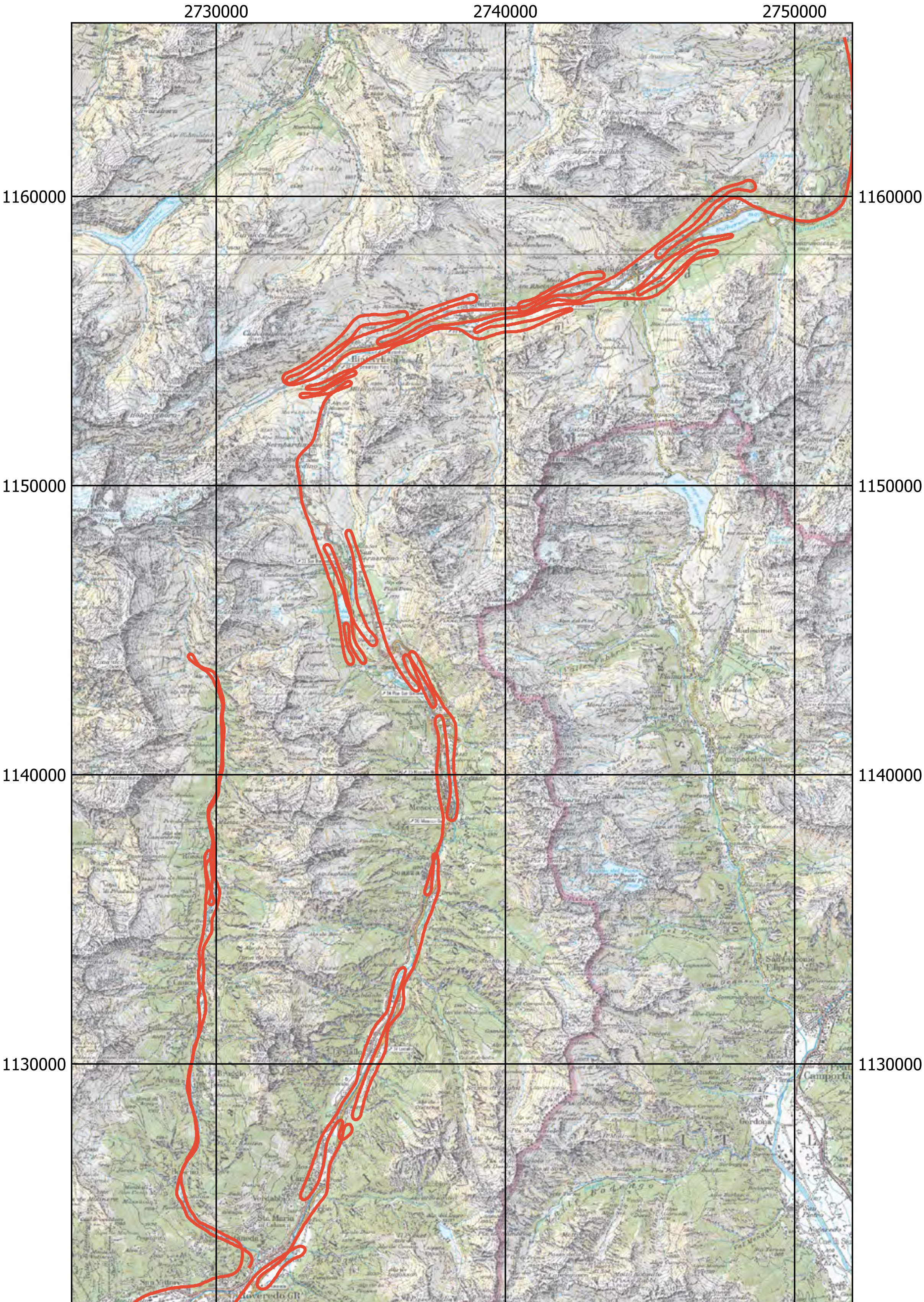

Figure 48: Flightline through the alpine valleys Rheinwald, Misox and Val Calanca. Geodaten©swisstopo.

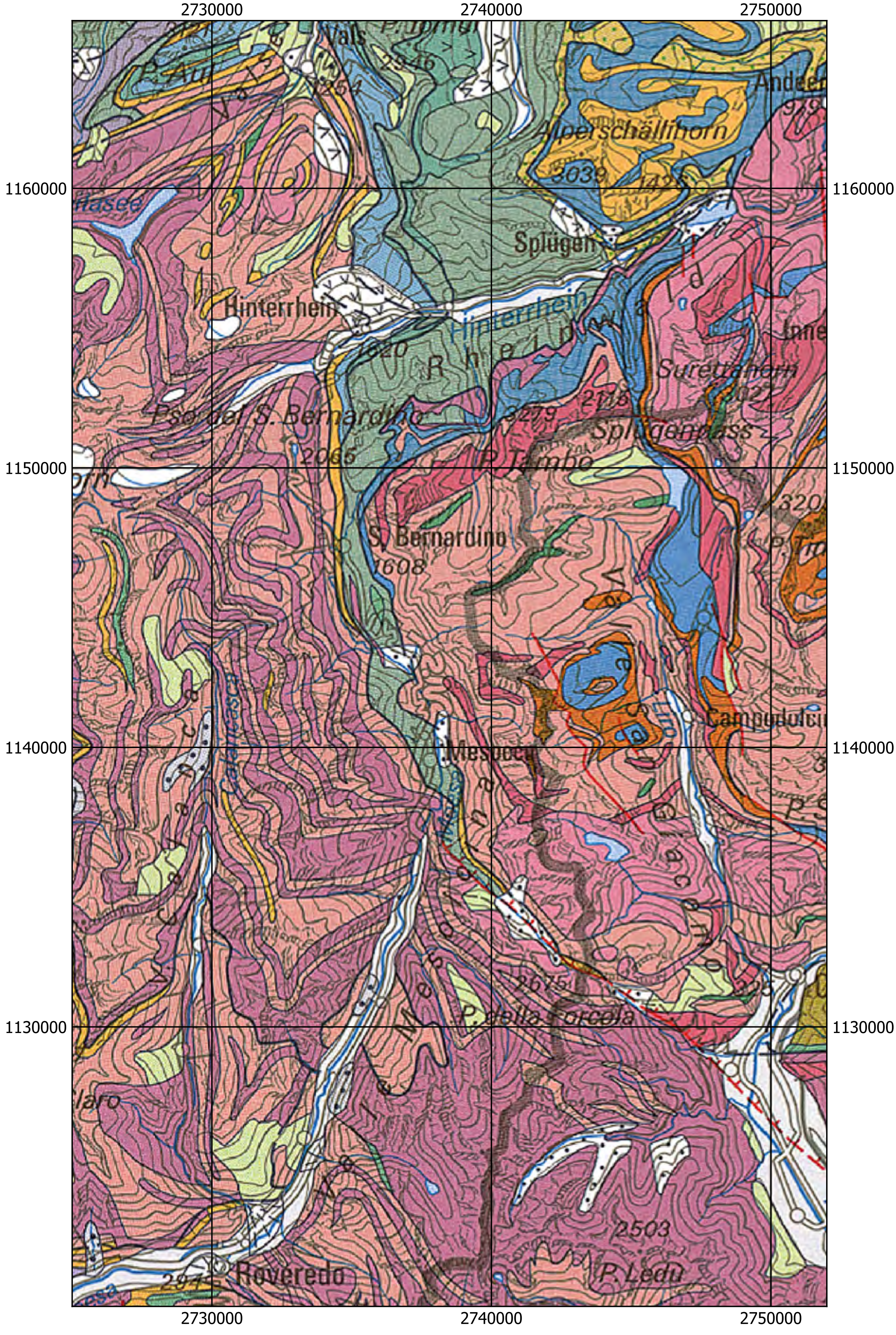

Figure 49: Geology around the alpine valleys Rheinwald, Misox and Val Calanca. Legend see Figure 32. Geodaten©swisstopo.

2.9.1 Rheinwald

The map of the dose rate (Figure 51) shows typical values for elevated alpine terrain. Corrected for the cosmic contribution to the dose rate (Figure 52), the terrestrial component of the dose rate indicates elevated values at the valley mouths. The map of the man-made gross count (MMGC) ratio yields no clear indication of man-made radionuclides. Nevertheless, besides of the photon emissions of natural radionuclides ^{40}K, ^{208}Tl, ^{214}Bi, ^{214}Pb and the positron annihilation peak at 511 keV, a weak signal from the 662 keV photon emission of ^{137}Cs can be observed both in the spectra averaged over the valley floor and the western valley mouth (Figure 50). The spectrum averaged over the valley mouth shows both elevated signals of natural radionuclides and ^{137}Cs. The maps of natural radionuclides (Figures 54, 55 and 56) and ^{137}Cs (Figure 57) reflect the observed elevated signals at the location of dose rate increase. The dose rate increase of the natural radionuclides can be attributed to granite and gneiss layers on the slopes of the Rheinwald (Figure 49), compared to shale layers in the valley floor. Larger residuals of ^{137}Cs activity deposited during the Chernobyl accident in forests compared to urban areas, due to different purging rates by precipitation, were already observed in the past (see for example Bucher et al., 2006). As the slopes of the valley are forested, the pattern of elevated values of ^{137}Cs activity concentration is similar to the pattern of elevated activity concentrations of natural radionuclides. The dose rates due to natural radionuclides and due to ^{137}Cs at the western valley mouth are twice the value observed at the valley bottom. ^{137}Cs contributes to about 10 percent of the terrestrial dose rate for both valley bottom and valley mouth.

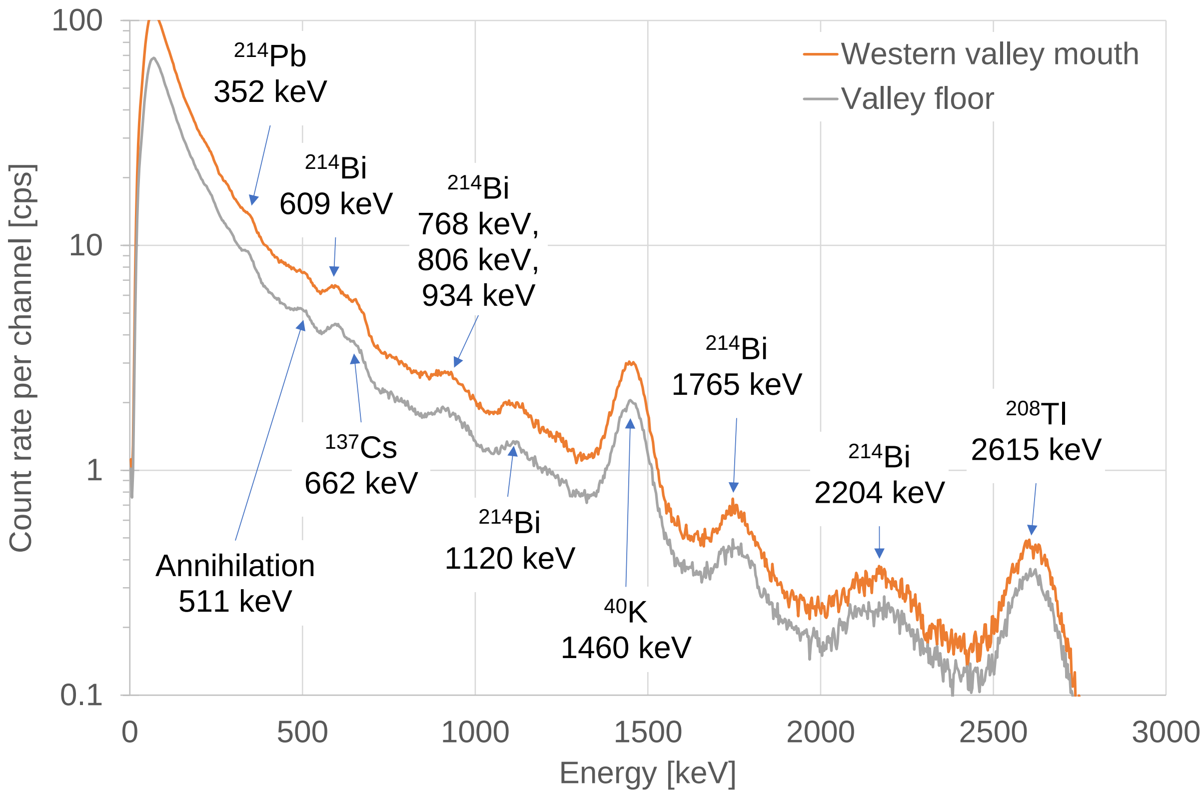

Figure 50: Average photon spectrum of the Rheinwald.

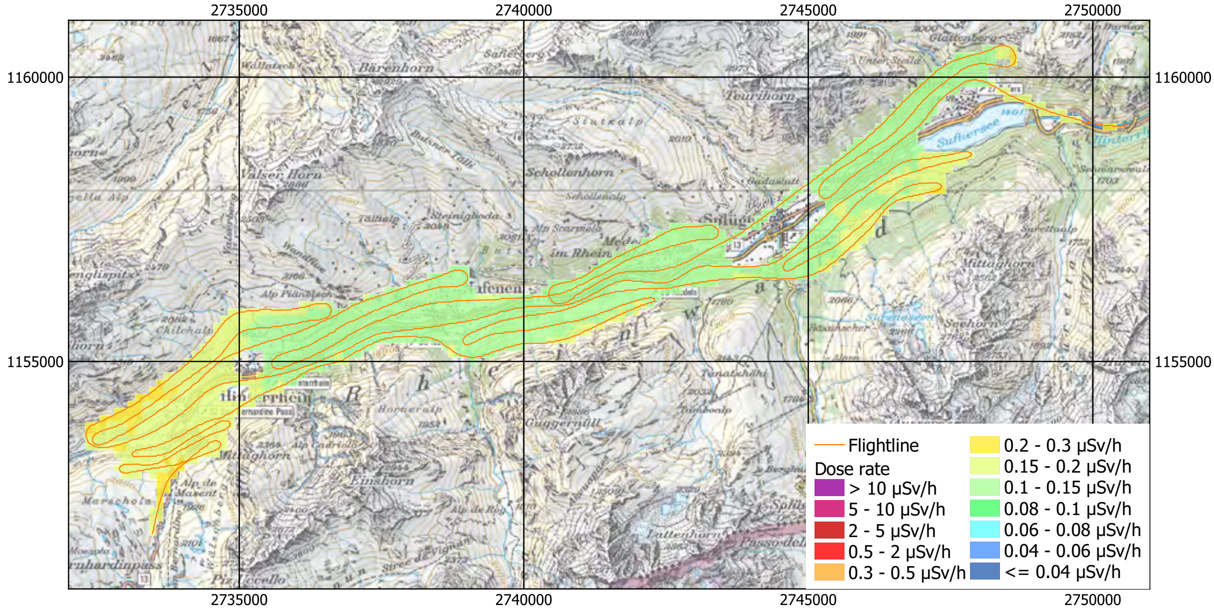

Figure 51: Dose rate in the Rheinwald. Geodaten©swisstopo.

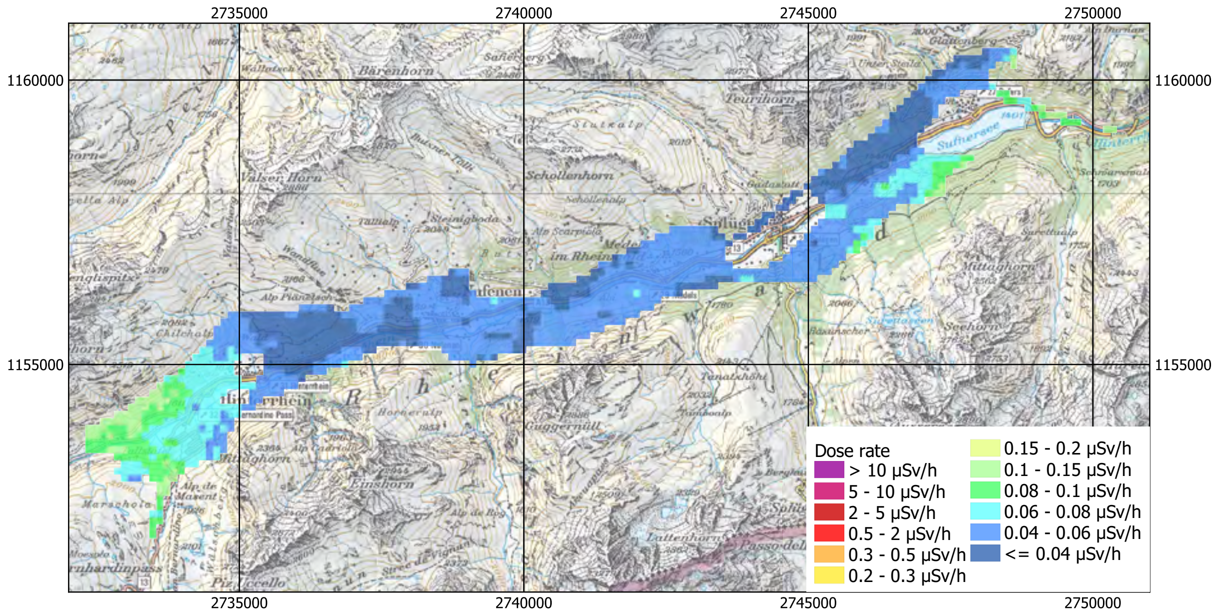

Figure 52: Terrestrial component of the dose rate in the Rheinwald. Geodaten©swisstopo.

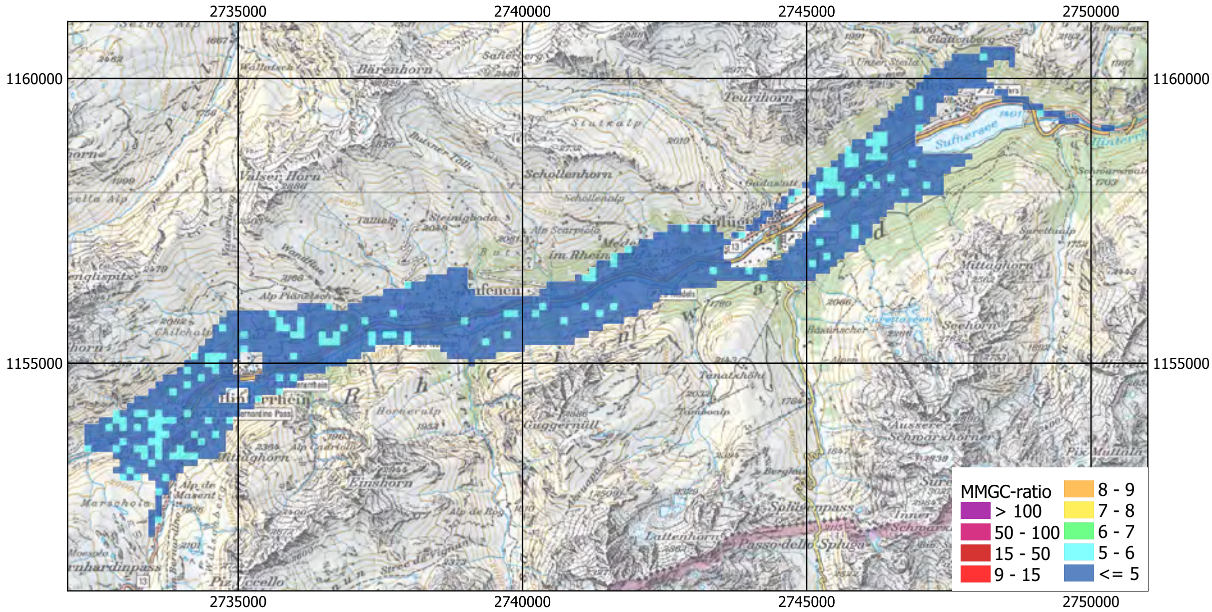

Figure 53: MMGC-ratio in the Rheinwald. Geodaten©swisstopo.

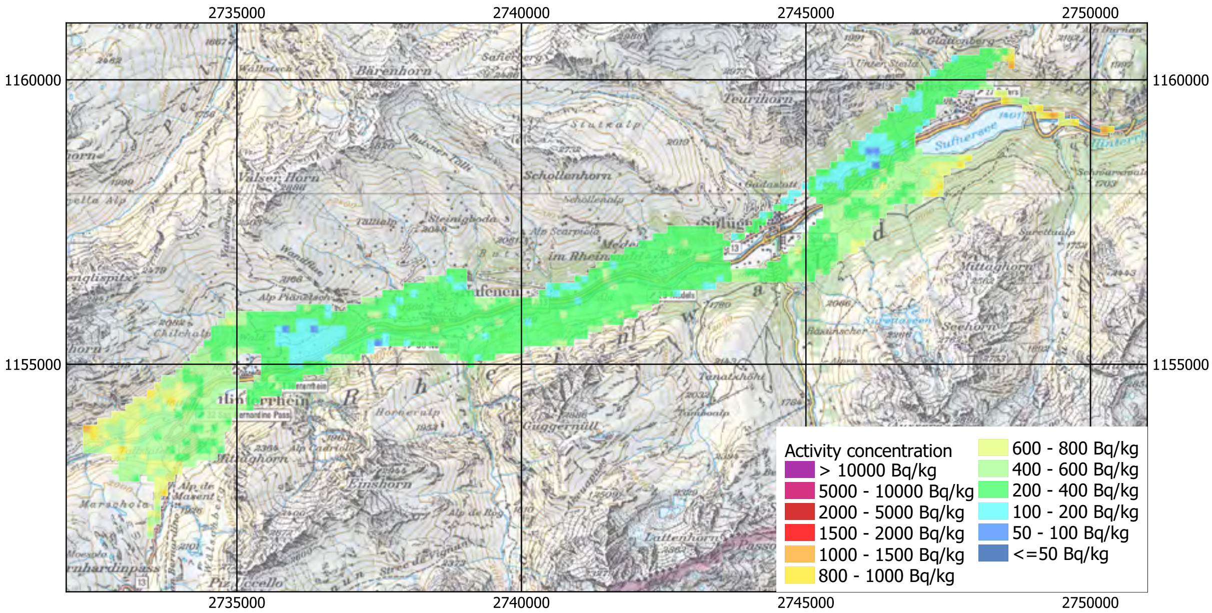

Figure 54: ^{40}K activity concentration in the Rheinwald. Geodaten©swisstopo.

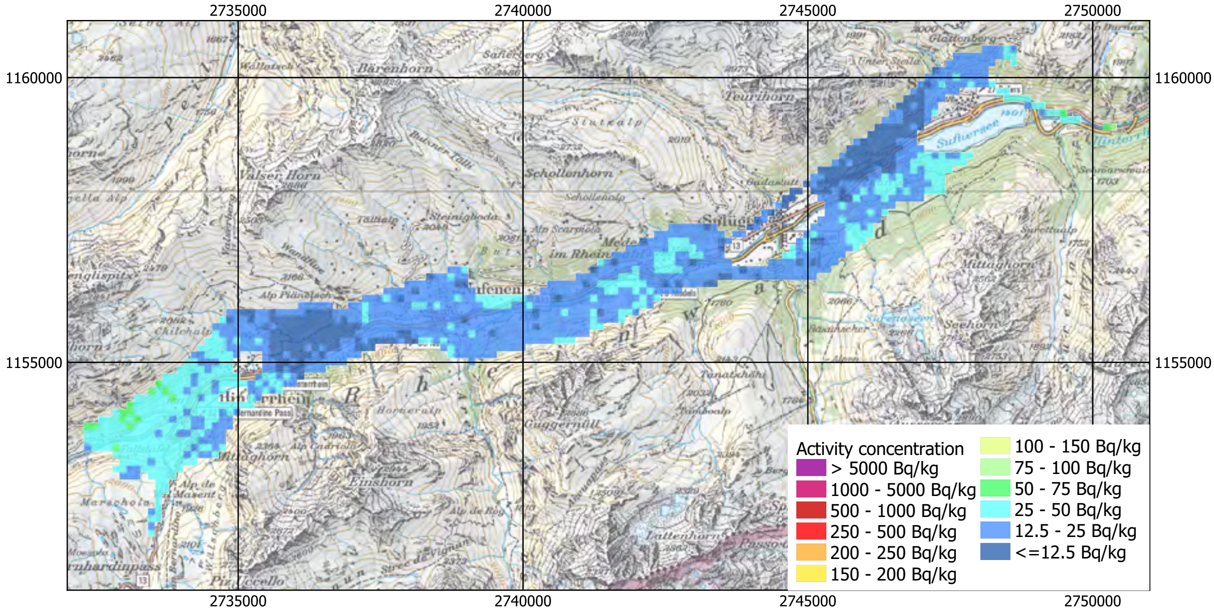

Figure 55: ^{232}Th activity concentration in the Rheinwald. Geodaten©swisstopo.

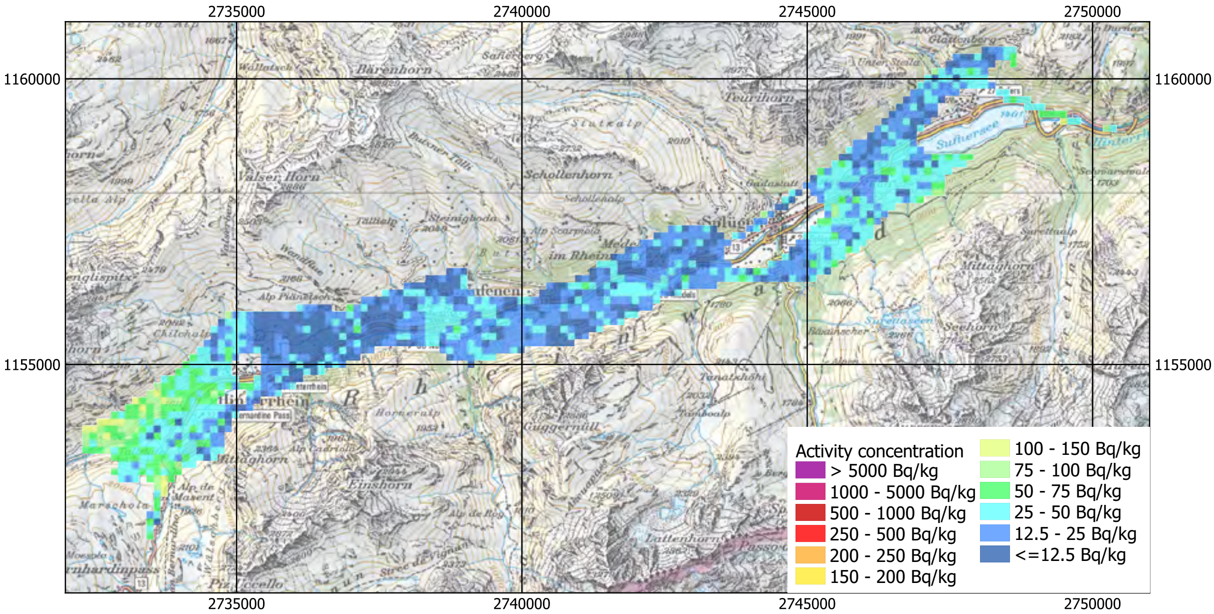

Figure 56: ^{238}U activity concentration in the Rheinwald. Geodaten©swisstopo.

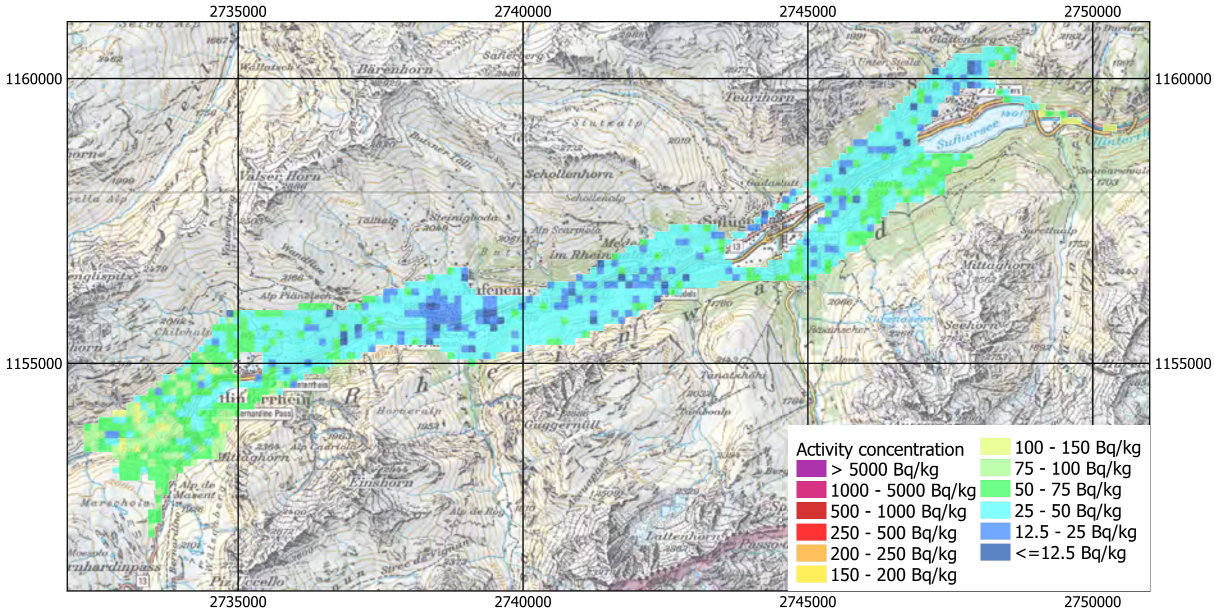

Figure 57: ^{137}Cs activity concentration in the Rheinwald. Geodaten©swisstopo.

2.9.2 San Bernadino

The maps of total dose rate (Figure 58) and the terrestrial dose rate (Figure 59) near San Bernadino repeat the pattern observed in the Rheinwald (section 2.9.1) with lower values measured over the valley bottom and higher values over the valley slopes. The elevated values concur with elevated concentrations of the natural radionuclides (Figures 61, 62 and 63) associated with the underlying granite (49). Residual ^{137}Cs activity originating from the Chernobyl accident can be detected throughout the measuring area (Figure 64). The man-made gross count (MMGC-) ratio as indicator for the presence of man-made radionuclides shows only a weak signal due to the low ^{137}Cs activity concentrations observed (Figure 60).

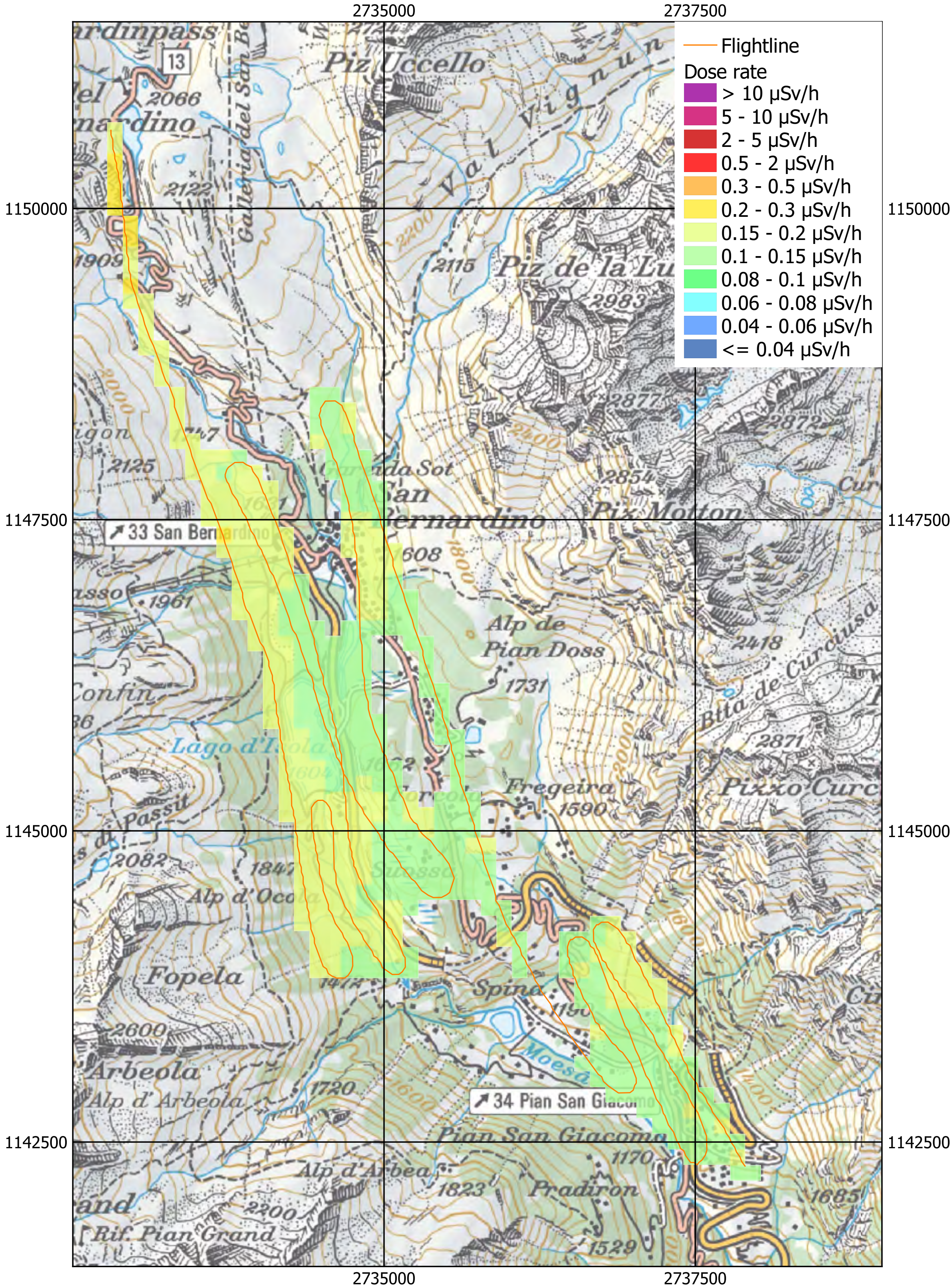

Figure 58: Dose rate near San Bernadino. Geodaten©swisstopo.

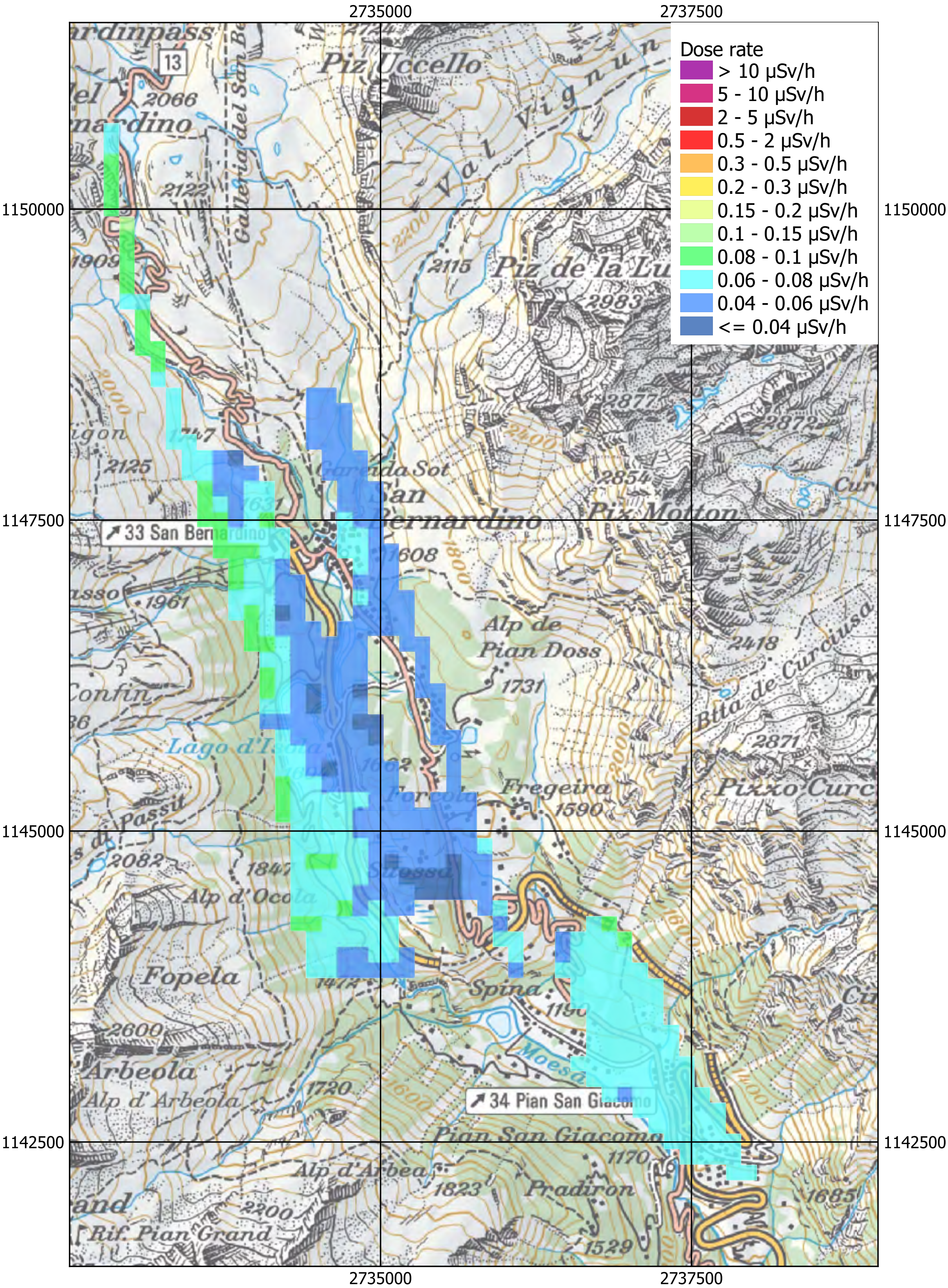

Figure 59: Terrestrial component of the dose rate near San Bernadino. Geodaten©swisstopo.

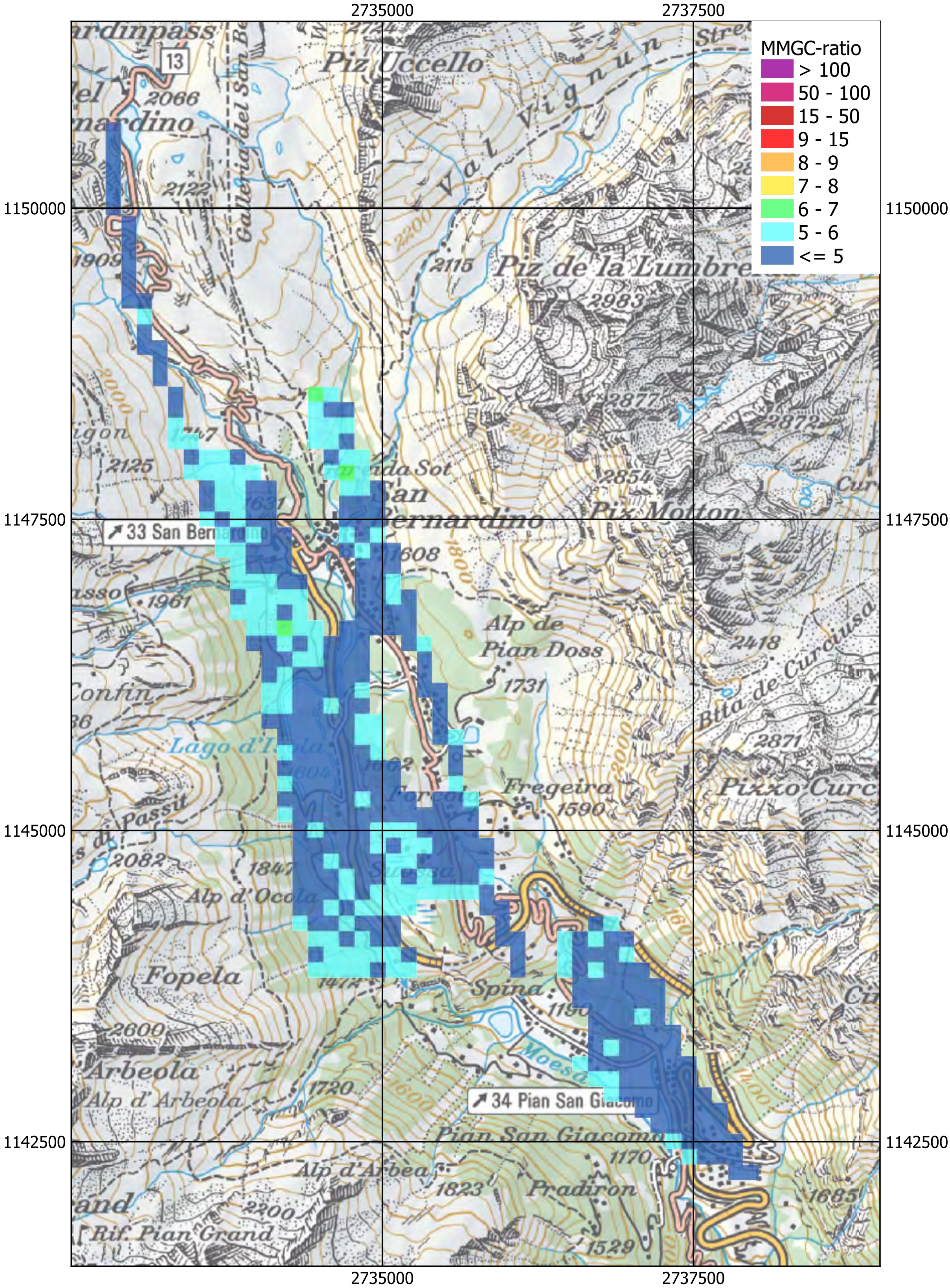

Figure 60: MMGC-ratio near San Bernadino. Geodaten©swisstopo.

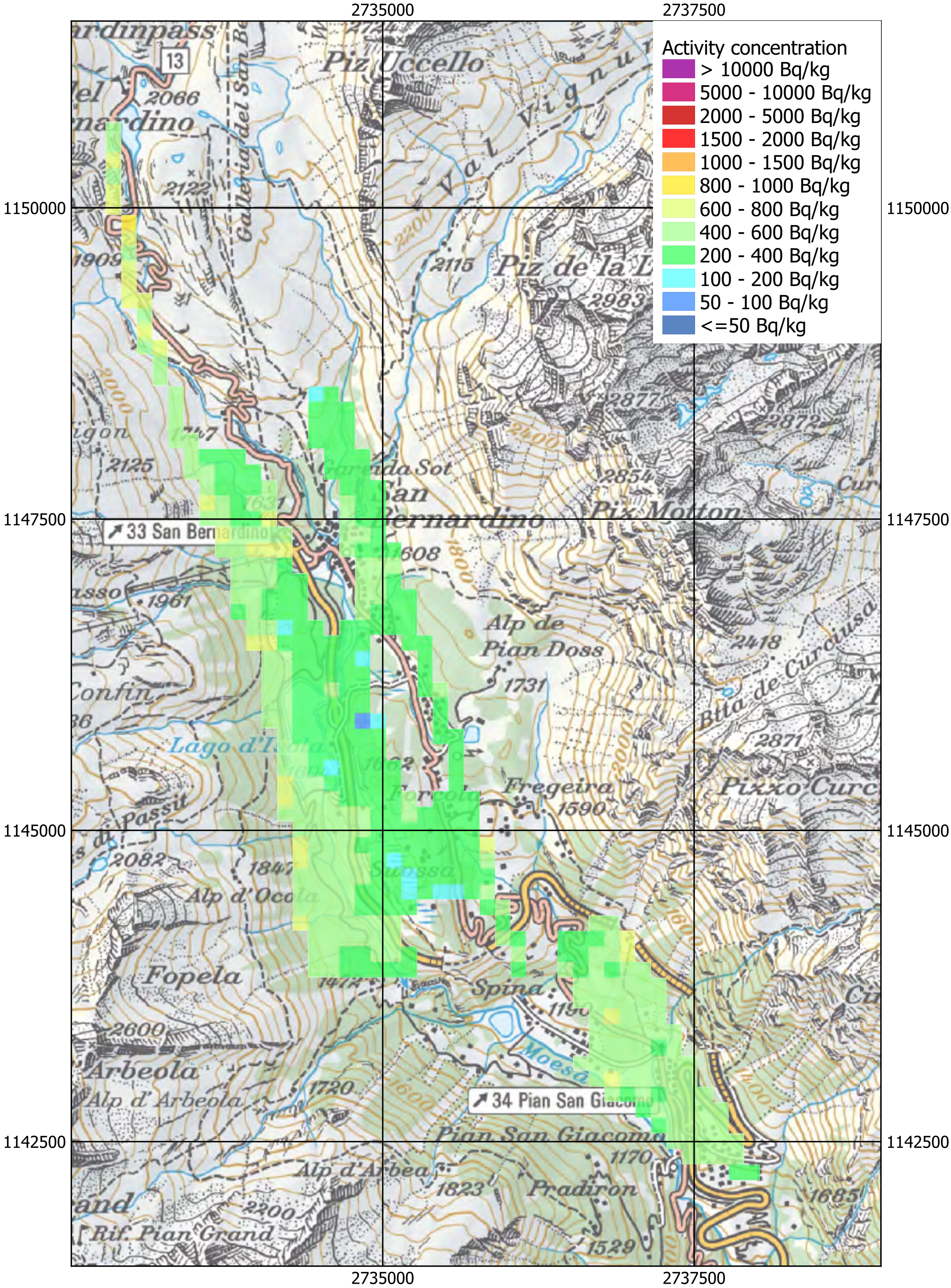

Figure 61: ^{40}K activity concentration near San Bernadino. Geodaten©swisstopo.

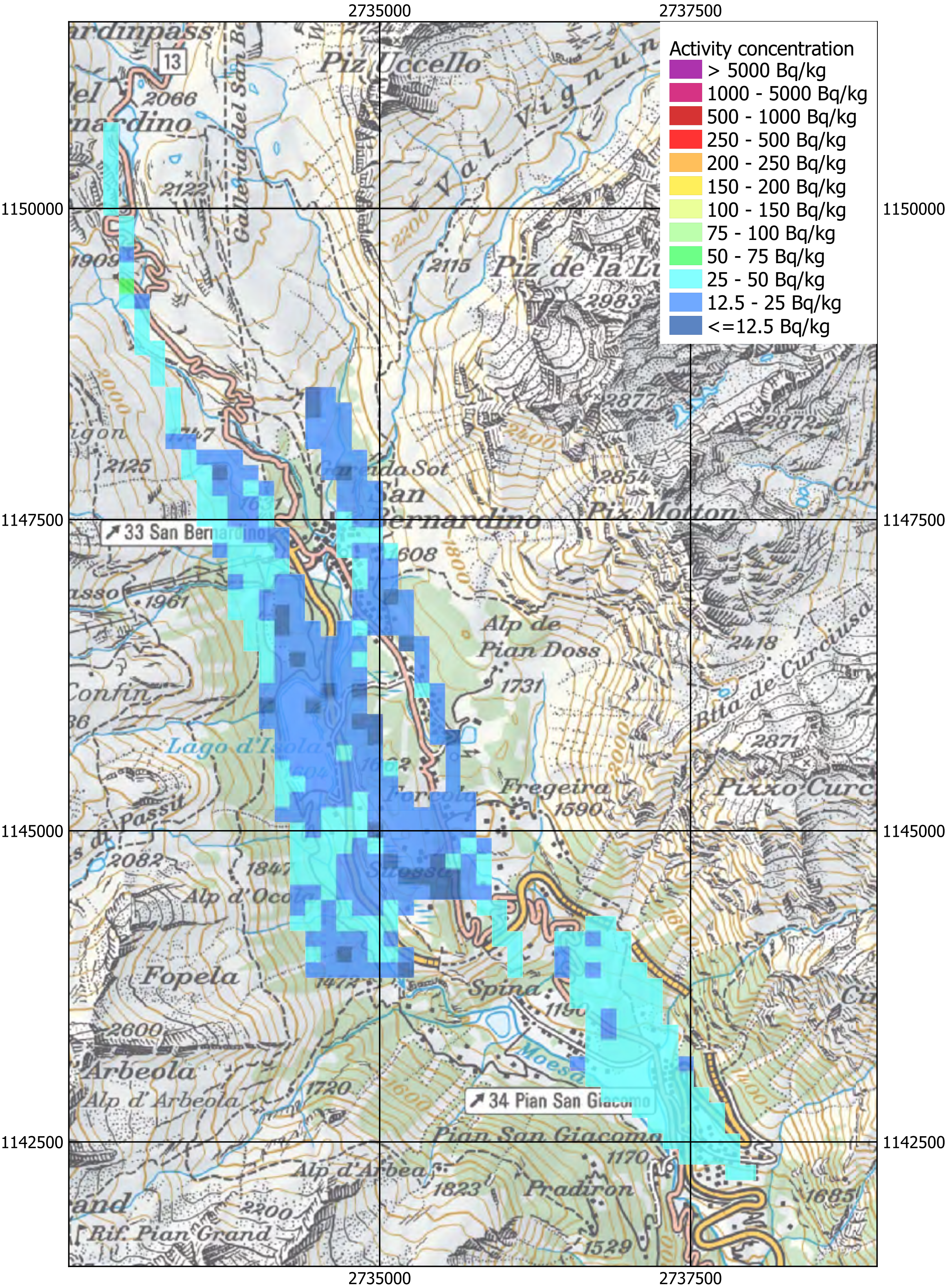

Figure 62: ^{232}Th activity concentration near San Bernadino. Geodaten©swisstopo.

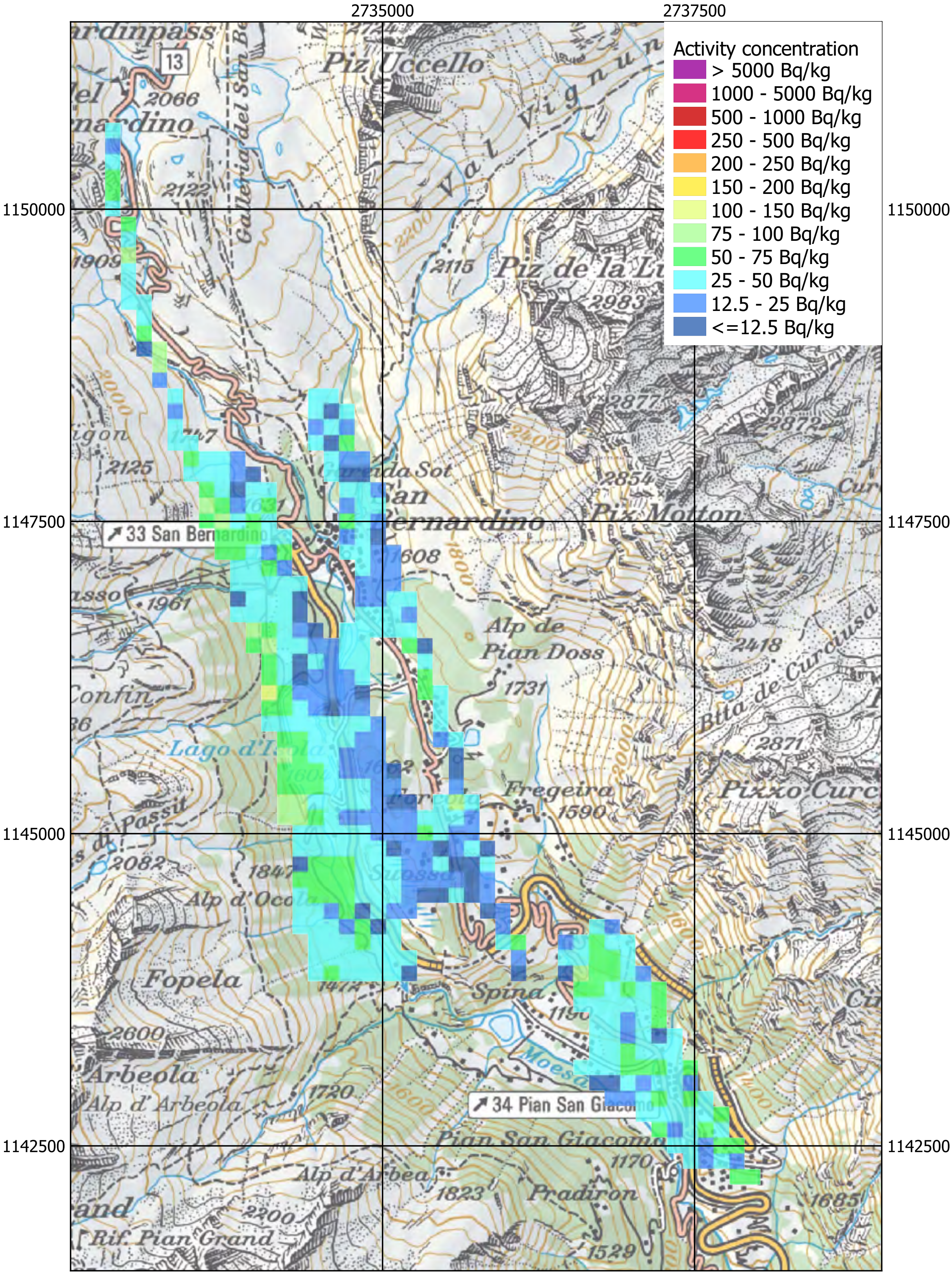

Figure 63: ^{238}U activity concentration near San Bernadino. Geodaten©swisstopo.

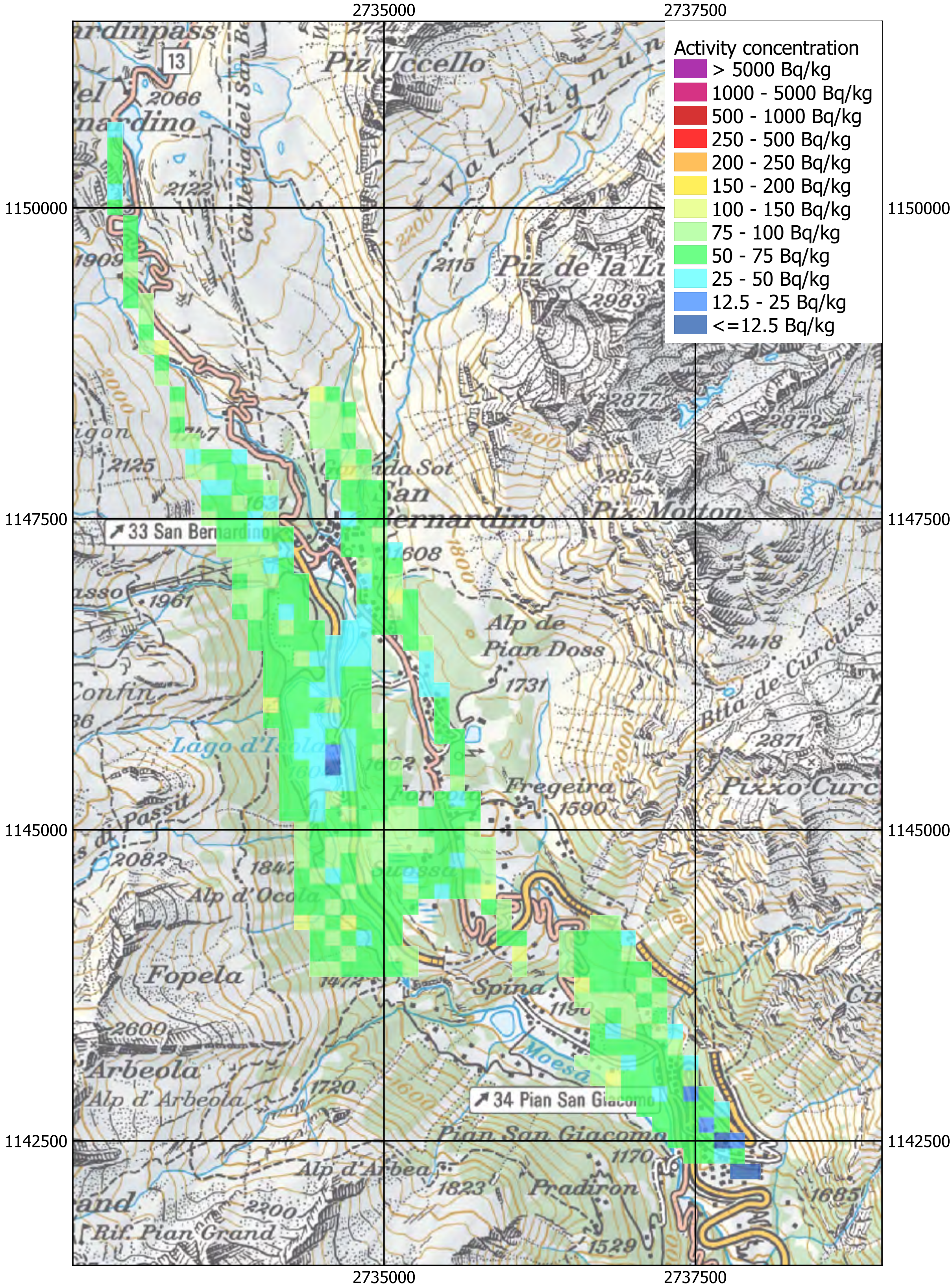

Figure 64: ^{137}Cs activity concentration near San Bernadino. Geodaten©swisstopo.

2.9.3 Valle Mesolcina and Val Calanca

The two nearly parallel valleys Valle Mesolcina and Val Calanca repeat the pattern of higher dose rates on the valley slopes compared to the valley bottom (Figures 65 and 66) caused both by a higher concentration of natural radionuclides (Figures 68, 69 and 70) and elevated concentration of Chernobyl caesium (Figure 71). Slightly elevated ^{137}Cs activity concentrations are found in the northern part of Val Calanca, also reflected in the map of the MMGC-ratio (Figure 67).

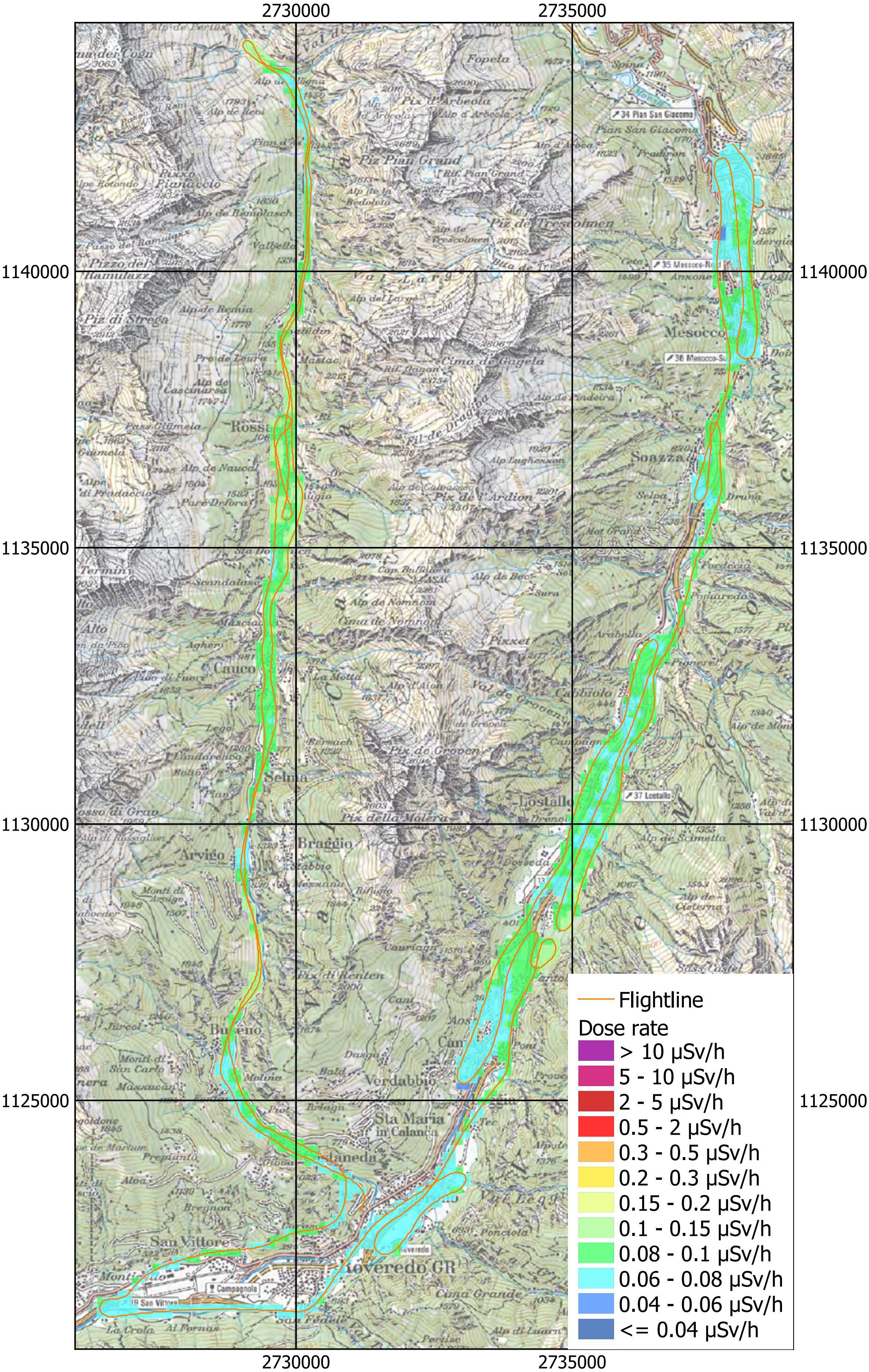

Figure 65: Dose rate in Valle Melsocina and Val Calanca. Geodaten©swisstopo.

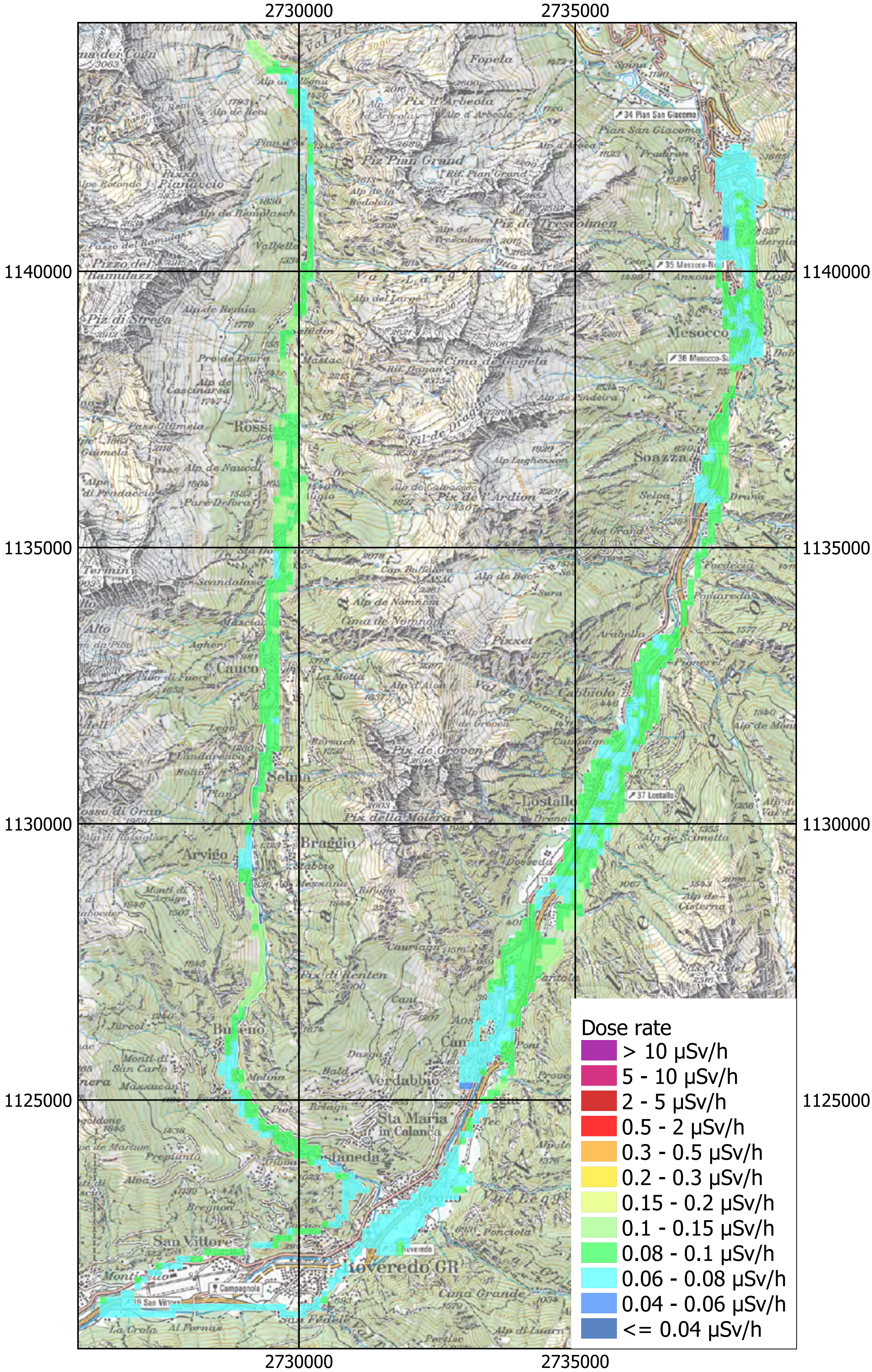

Figure 66: Terrestrial component of the dose in Valle Melsocina and Val Calanca. Geodaten©swisstopo.

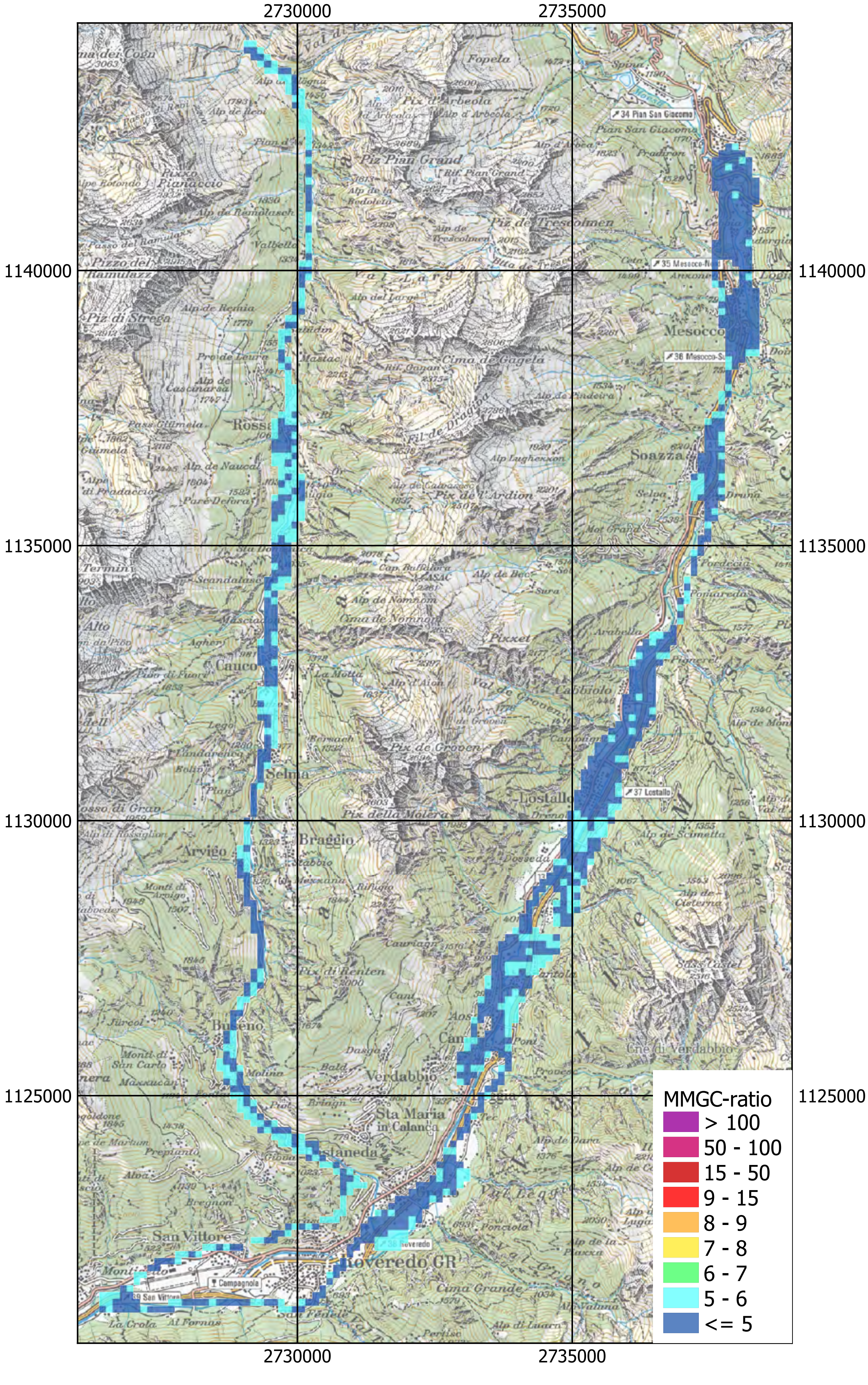

Figure 67: MMGC-ratio in Valle Melsocina and Val Calanca. Geodaten©swisstopo.

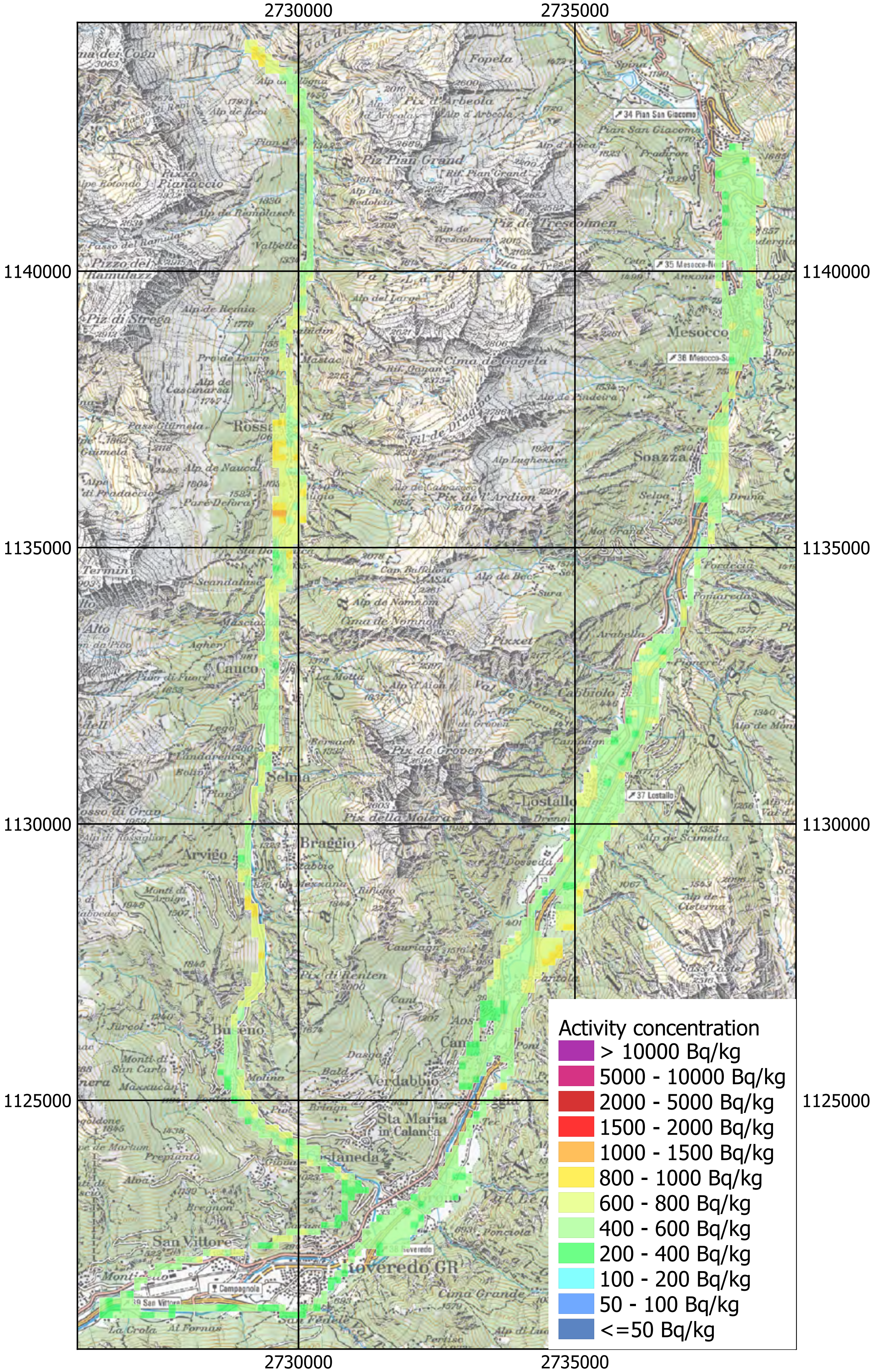

Figure 68: ^{40}K activity concentration in Valle Melsocina and Val Calanca. Geodaten©swisstopo.

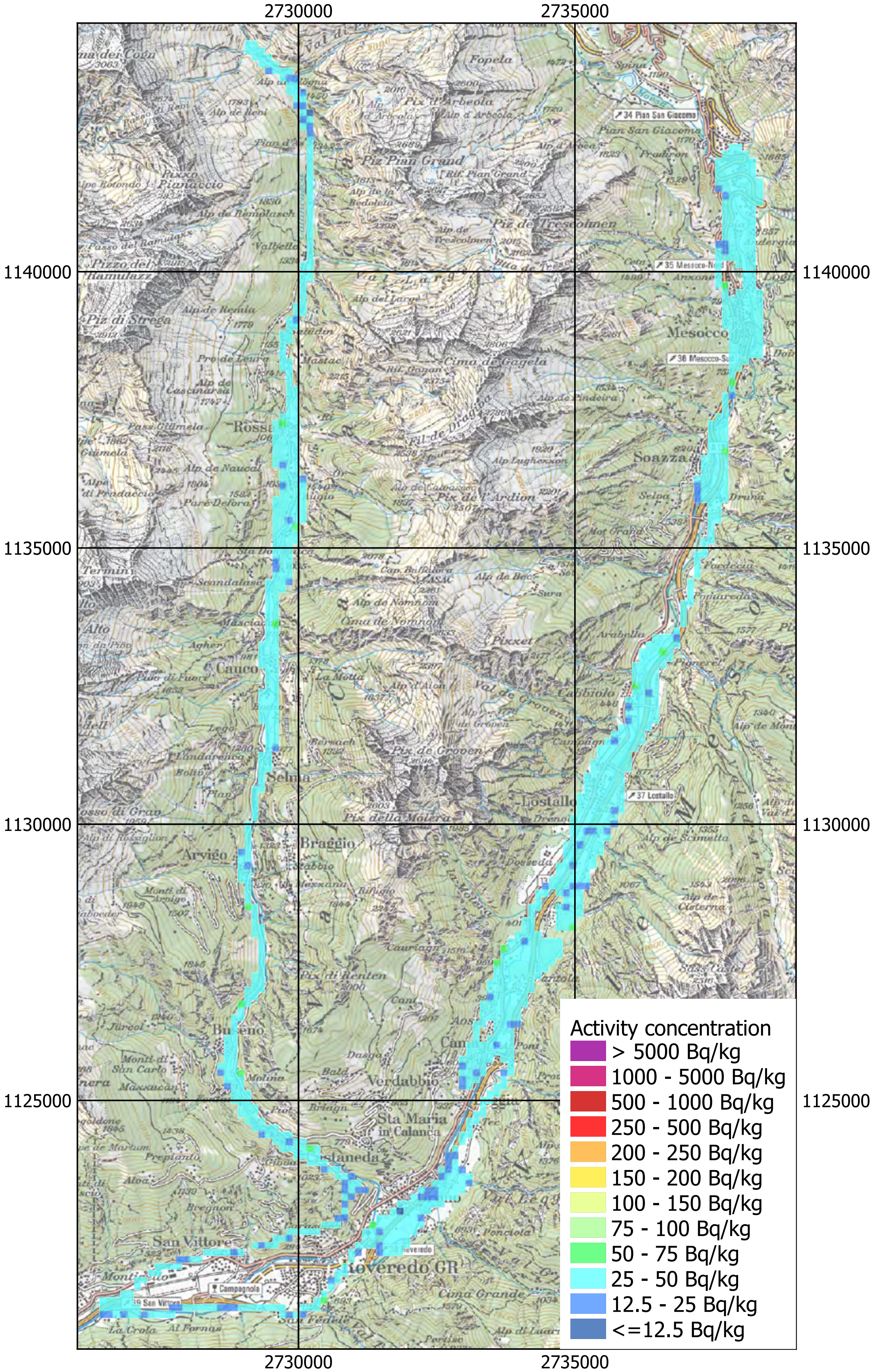

Figure 69: ^{232}Th activity concentration in Valle Melsocina and Val Calanca. Geodaten©swisstopo.

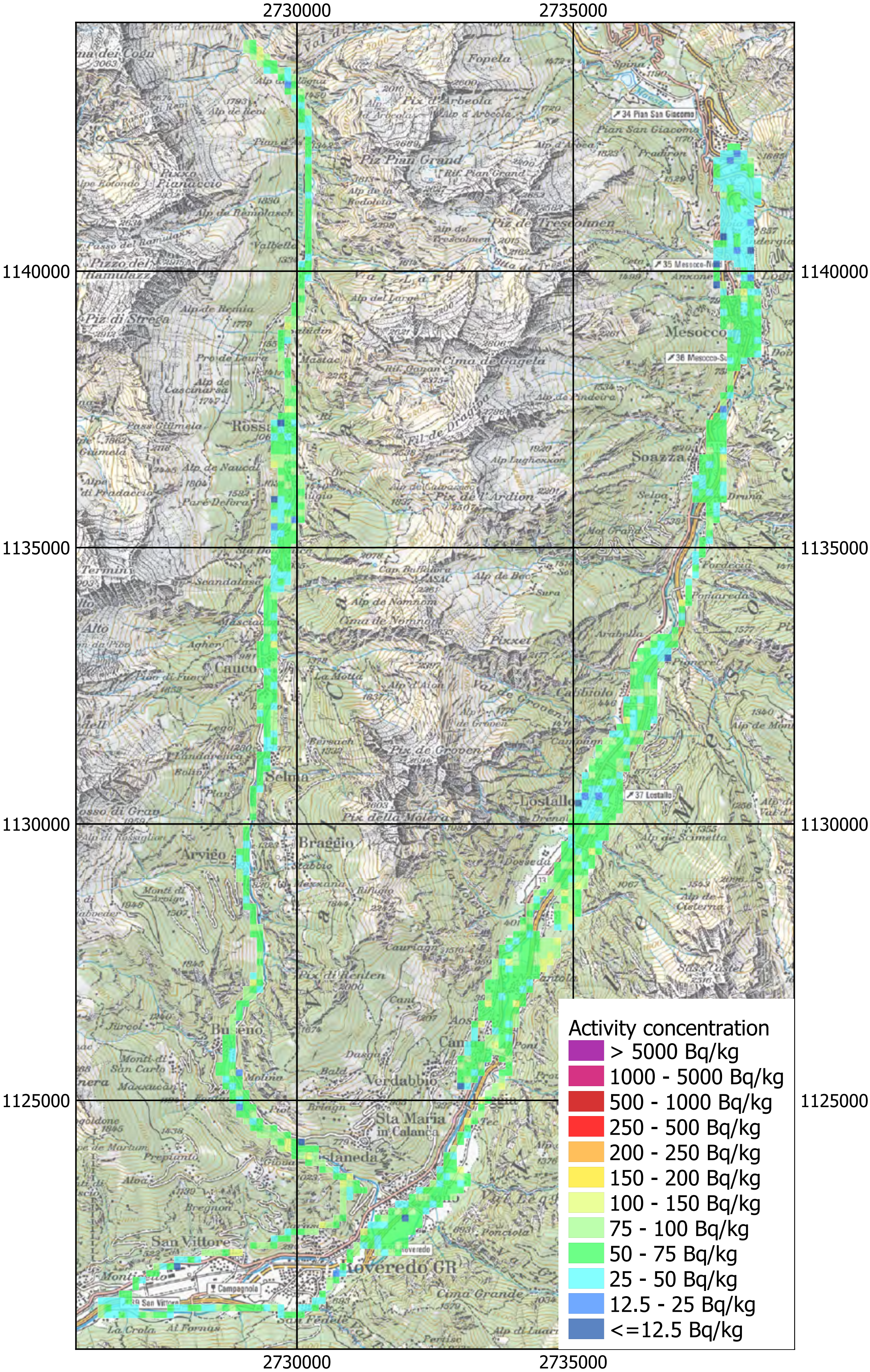

Figure 70: ^{238}U activity concentration in Valle Melsocina and Val Calanca. Geodaten©swisstopo.

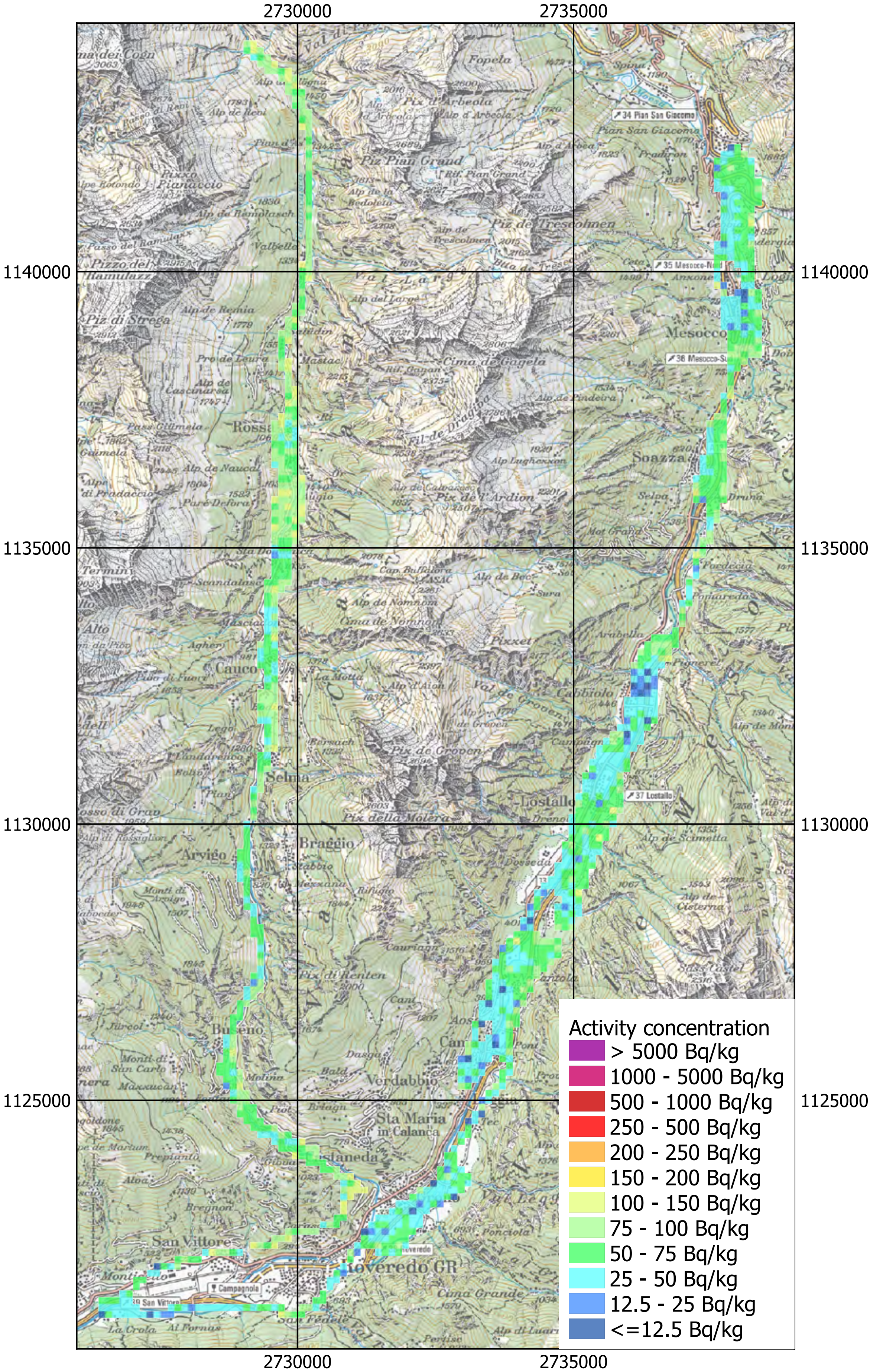

Figure 71: ^{137}Cs activity concentration in Valle Melsocina and Val Calanca. Geodaten©swisstopo.

2.9.4 Weisstannental

Uranium hotspots in the Weisstannental were already observed fifty years ago during a scientific measurement campaign to locate prospective uranium deposits in Switzerland (Burkhard et al., 1985). In association with a school project of the Kantonsschule Heerbrugg in 1996, the area with the uranium hotspots was inspected with airborne gamma-spectrometry in 1997 (Bucher et al., 1998). The hotspots could not be localised from these measurements due to the limited spatial extension of higher uranium concentrations. An uranium hotspot in the Weisstannental at Swiss national coordinates 2738452, 1204160 and 2040 m above sea level was reported in 2008 (Bützer, 2008). The area around this location was inspected to investigate if an anomaly can be identified with the AGS system. The dose rate map (Figure 72) of the area around the hotspot shows typically elevated values due to an increased amount of cosmic radiation at the altitude of 2000 m. Only measured data with a ground clearance between 30 m and 200 m were included into the maps, to prevent evaluation artefacts from the extrapolation to the standard ground clearance of 100 m. This leads to parts of the flight line not represented in the gridded quantity maps. The map of the terrestrial dose rate (Figure 73) shows higher values in the western part of the measurement area, due to elevated concentrations of the natural radionuclides ^{40}K (Figure 74), ^{232}Th (Figure 75) and ^{238}U (Figure 76). The geology of the area (Figure 77) reflects the pattern of the measured values with larger concentrations of natural radionuclides located in Permian layers (Verrucano, brown). Nevertheless, as in 1997, individual uranium hotspots could not be spatially resolved.

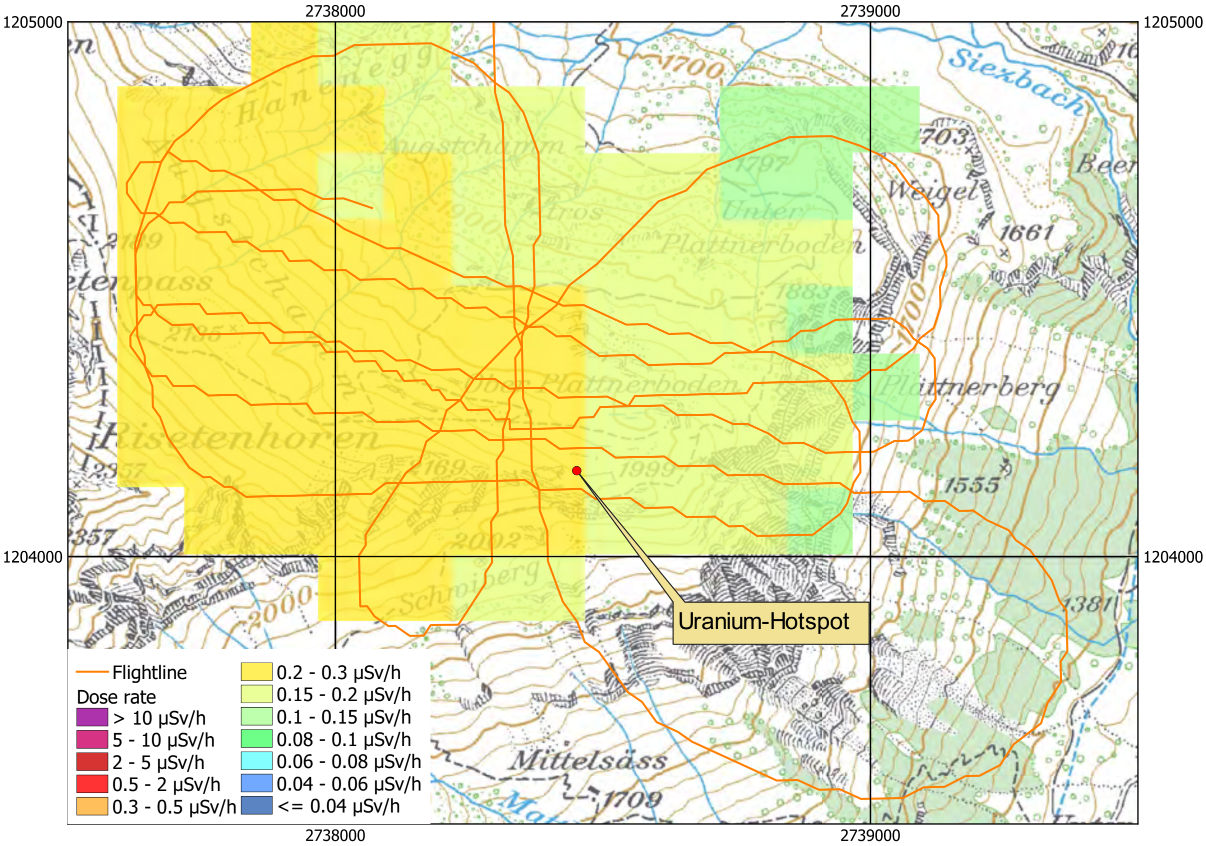

Figure 72: Dose rate near the Weisstannental. Geodaten©swisstopo.

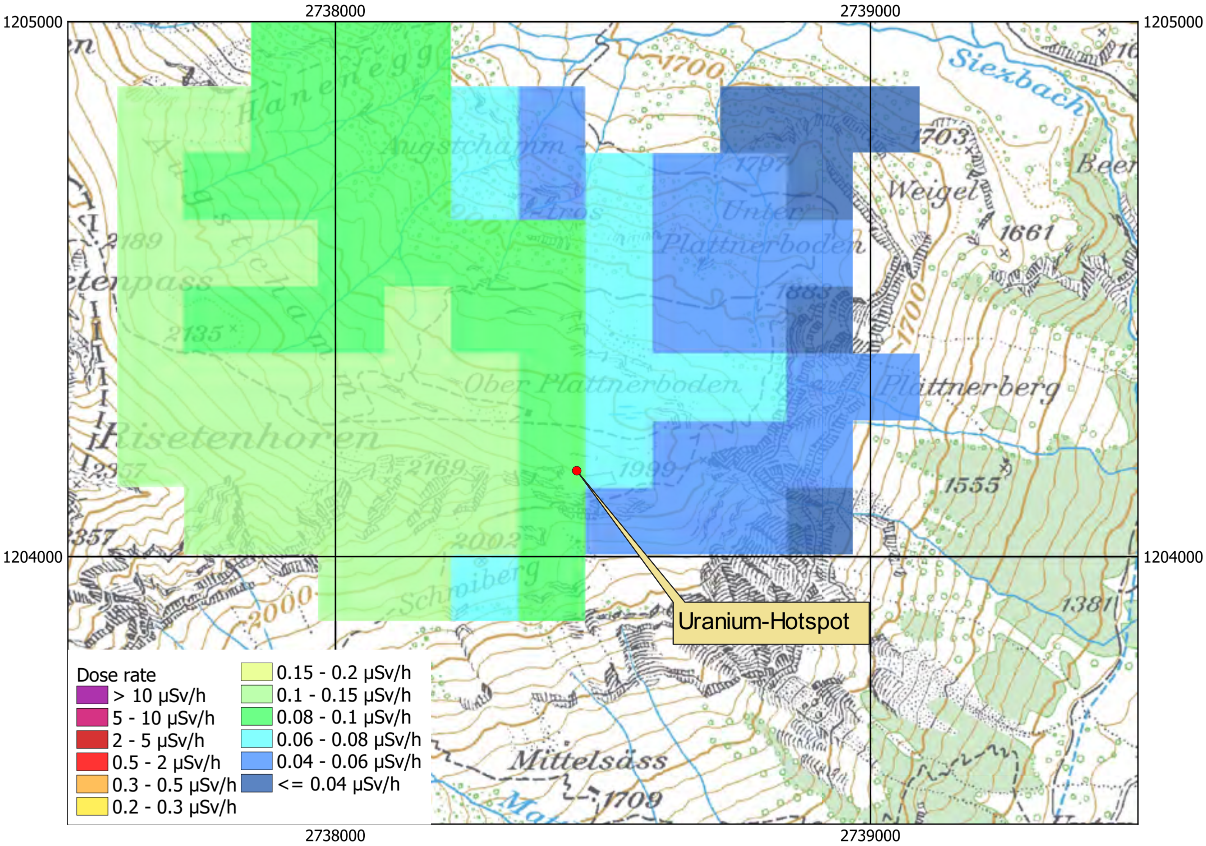

Figure 73: Terrestrial dose rate near the Weisstannental. Geodaten©swisstopo.

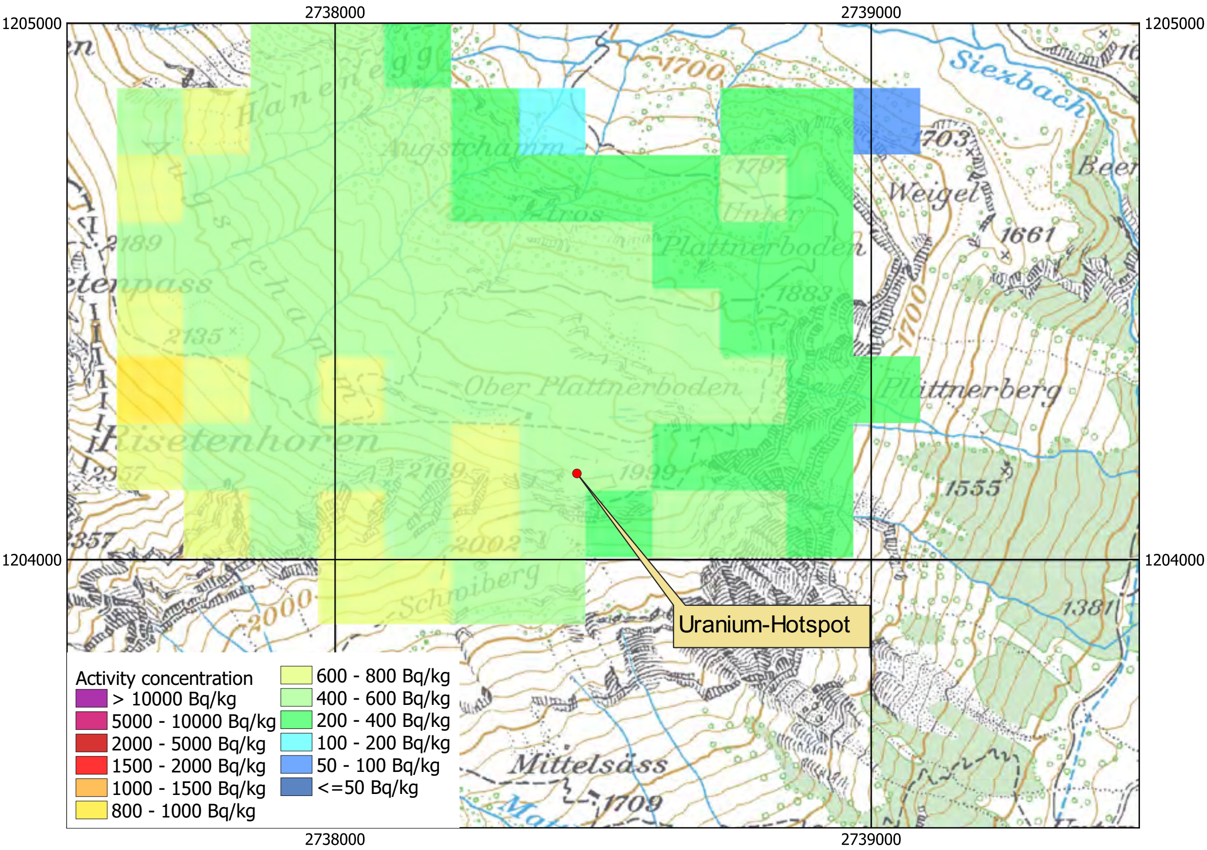

Figure 74: ^{40}K activity concentration near the Weisstannental. Geodaten©swisstopo.

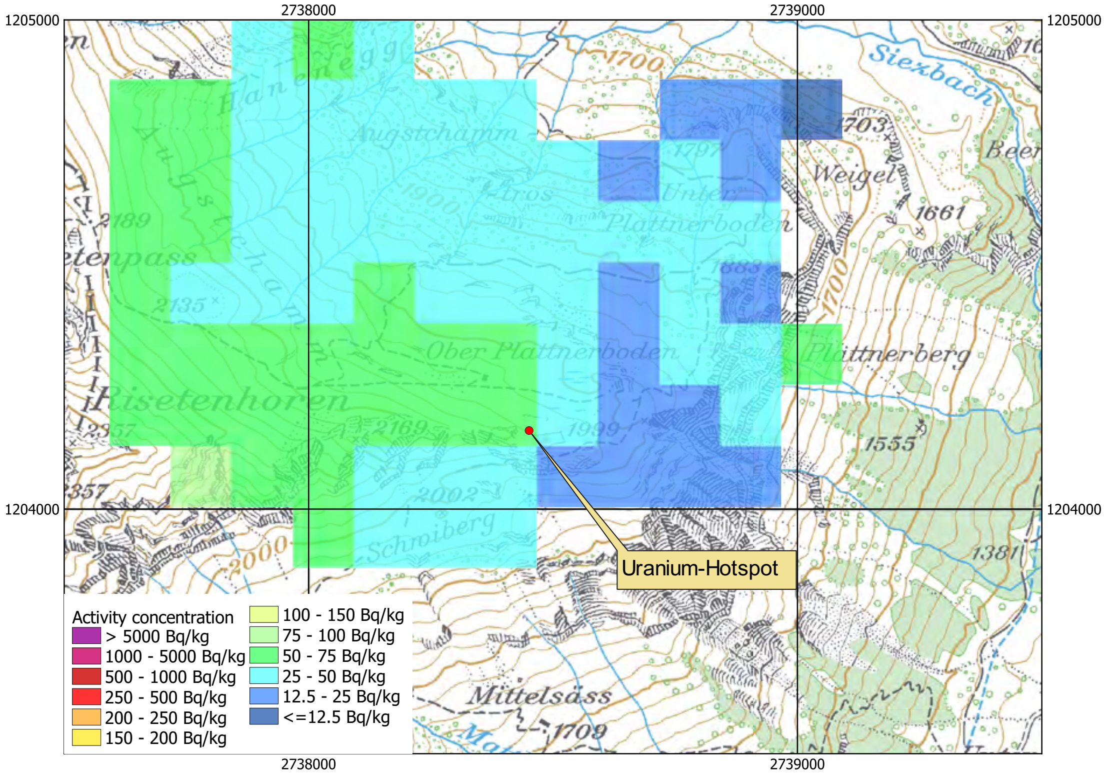

Figure 75: ^{232}Th activity concentration near the Weisstannental. Geodaten©swisstopo.

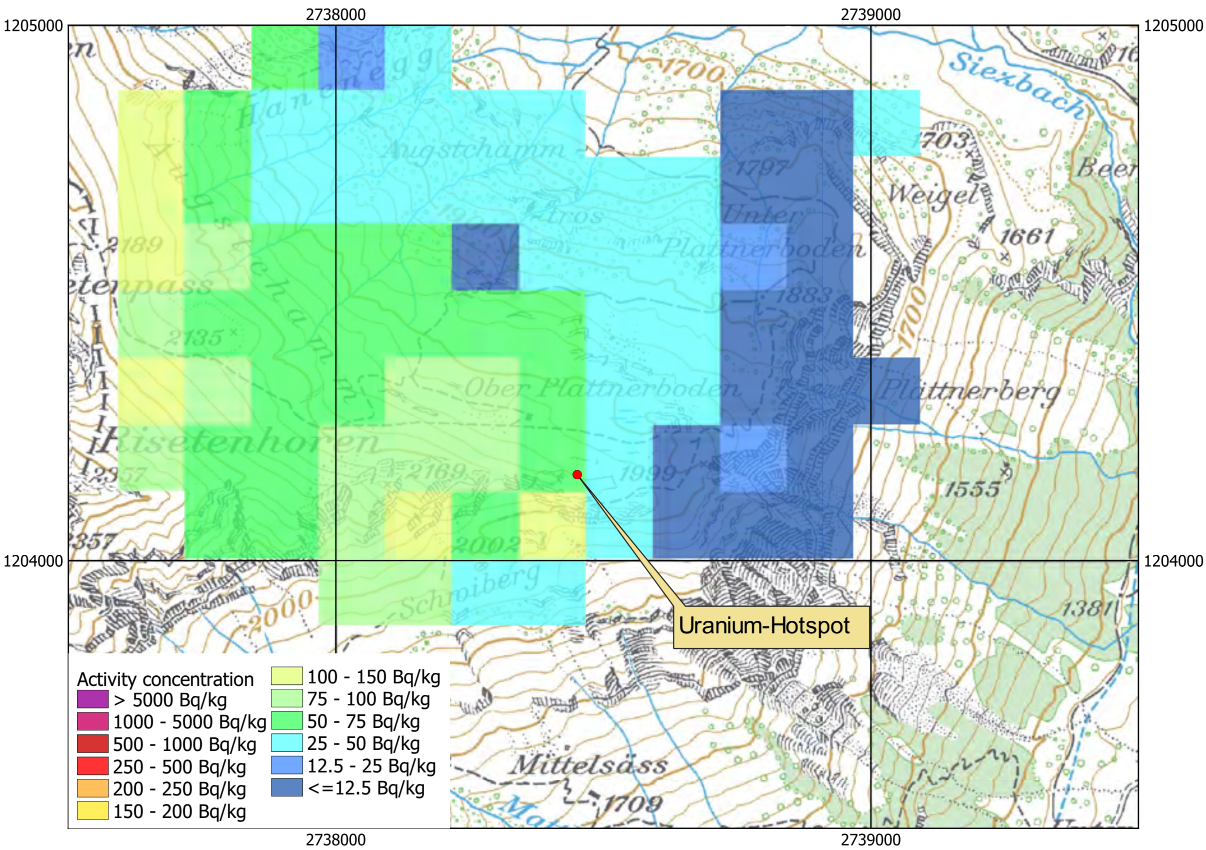

Figure 76: ^{238}U activity concentration near the Weisstannental. Geodaten©swisstopo.

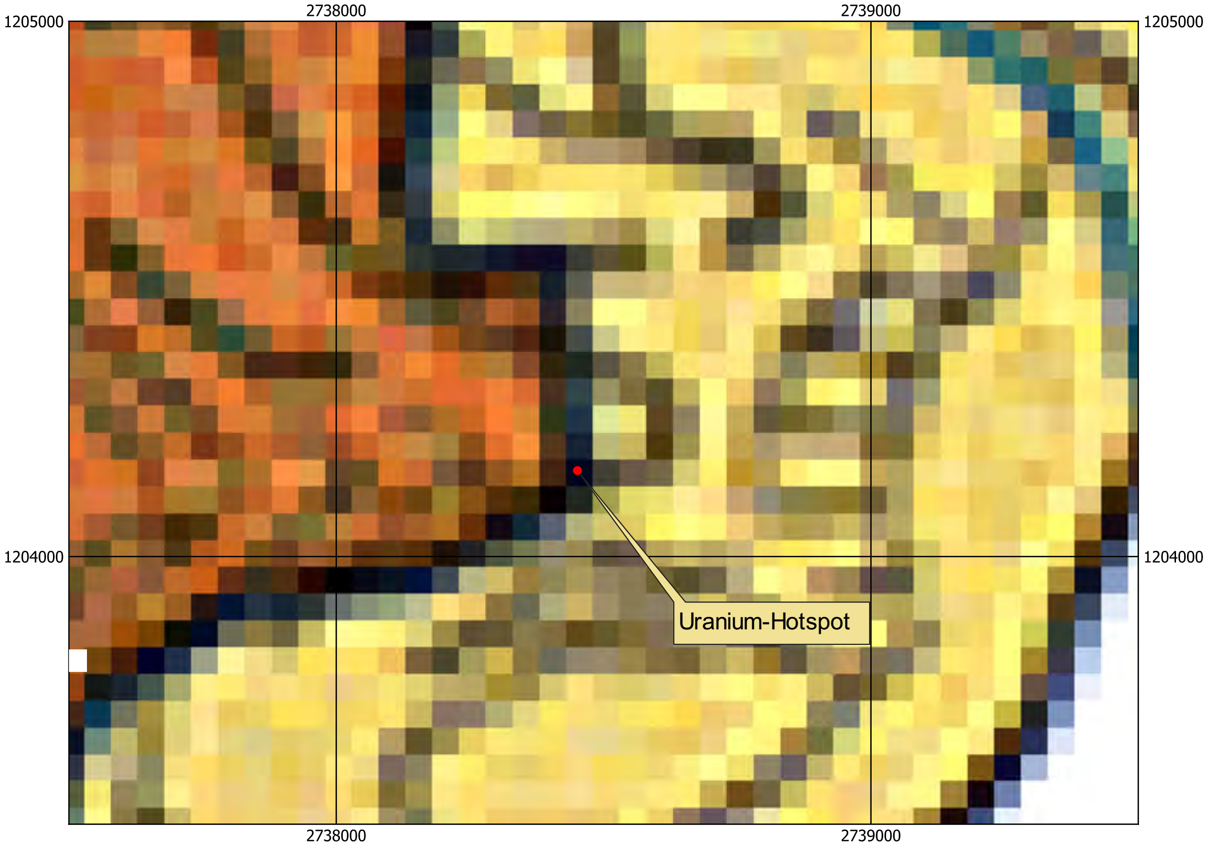

Figure 77: Geology near the Weisstannental. Legend see Figure 32.
Geodaten©swisstopo.

2.10 Thun military training ground

A complete day of the ARM22c exercise part was dedicated to support an ongoing PhD thesis at ETHZ and PSI (Breitenmoser et al., 2022). The task of the thesis is the development of a new calibration method for the Swiss airborne gamma-ray spectrometry systems based on the Monte-Carlo radiation transport code FLUKA maintained by CERN (Battistoni et al, 2015). The aim of the measurements was to provide an experimental verification of modelling results. Figure 78 shows one of the measurements, where the helicopter was exposed to a radioactive ^{137}Cs source provided by NBC-EOD Centre of Competence. The measurements were performed with different fuel levels to verify the quality of the numerical model parameters (Figure 79).

Figure 78: Ground measurement with radioactive source.

Figure 79: Numerical representation of the ground measurement with radioactive source. This figure was generated by the software package FLAIR (Vlachoudis, 2009).

3 Conclusions

The survey of the Swiss nuclear power plants Beznau (KKB) and Leibstadt (KKL) and the intermediate storage facility ZWILAG showed no artificial radionuclides in the vicinity of the plant premises. Short-lived radionuclides emitted from the stack of the western area of the Paul Scherrer Institute were detected in the vicinity of the research institute. These stack emissions are permitted by the regulatory authority and are continuously monitored. The site of the former Lucens reactor was unobtrusive in the measured data.
Altitude profiles over Lake Thun and Lake Neuchâtel demonstrated an evident effect of airborne radon progeny on the profiles. The results indicate that the applied experimental method for correction of cosmic radiation and background should be revised. Alternative approaches are under discussion.
Background flights were performed over several Swiss cities, regions and valleys. Besides attenuation effects of water bodies, variations of natural radionuclide content could be observed. Remains of the Chernobyl deposition were detected near the French border and in southern Switzerland.
Two of the four Swiss measuring systems were used during ARM22 and performed both according to specifications. Under the condition that all four systems perform inside of specifications, individual stripping profiles may be replaced with generic factors for all RLL detectors in the future.

4 Literature

Baldocini, M., Albéri, M., Bottardi, C., Minty, B., Raptis, K.G.C., Strati, V., Mantovani, F.: Exploring atmospheric radon with airborne gamma-ray spectroscopy. Atmospheric Environment 170, pp.259-268, 2017.
DOI https://doi.org/10.1016/j.atmosenv.2017.09.048

Battistoni, G., Boehlen, T., Cerutti, F., Chin, P.W., Esposito, L.S., Fassò, A., Ferrari, A., Lechner, A., Empl, A., Mairani, A., Mereghetti, A., Ortega, P.G., Ranft, J., Roesler, S., Sala, P.R., Vlachoudis, V., Smirnov, G.: Overview of the FLUKA code, Annals of Nuclear Energy, vol. 82, pp. 10–18, 2015.

Breitenmoser, D., Butterweck, G., Kasprzak, M. M., Yukihara, E. G., Mayer, S.: Experimental and Simulated Spectral Gamma-Ray Response of a NaI(Tl) Scintillation Detector used in Airborne Gamma-Ray Spectrometry. Advances in Geosciences 57, 89–107 (2022).
DOI https://doi.org/10.5194/ADGEO-57-89-2022

Bucher, B.: Methodische Weiterentwicklungen in der Aeroradiometrie. Dissertation Nr. 13973, ETH Zürich, 2001.

Bützer, P.: Ein radioaktiver "'Hotspot"' im Verrucano des Weisstannentals. Berichte der St. Gallischen Naturwissenschaftlichen Gesellschaft 91, 2008.
DOI http://doi.org/10.5169/seals-832615

Burkhard, D.J.M., Rybach, L., Bächtiger, K.: Uranium and copper ore minerals in a Lower Permian lapilli-agglomerate tuff in Eastern Switzerland (Weisstannental, Kanton St. Gallen), Schweiz, mineral, petrogr. Mitt. 65, pp. 335-352, 1985.

Jacobi, W., André, K.: The Vertical Distribution of Radon 222, Radon 220 and Their Decay Products in the Atmosphere, J. Geophys. Res. 68(13), pp. 3799-3814, 1963.

Schwarz, G. F.: Methodische Entwicklungen zur Aerogammaspektrometrie. Beiträge zur Geologie der Schweiz, Geophysik Nr. 23, Schweizerische Geophysikalische Kommission, 1991.

Schwarz, G. F., Rybach, L., Klingele, E. E.: Design, calibration, and application of an airborne gamma spectrometer system in Switzerland, Geophysics 62(5), pp. 1369-1378, 1997.
DOI https://doi.org/10.1190/1.1444241

Vlachoudis, V.: Flair: A powerful but user friendly graphical interface for FLUKA, International Conference on Mathematics, Computational Methods & Reactor Physics (M&C 2009), Saratoga Springs, New York, May 3-7, 2009.
URL http://flair.web.cern.ch/flair/doc/Flair_MC2009.pdf

Wildi, T.: Der Traum vom eigenen Reaktor - Die schweizerische Atomtechnologieentwicklung 1945-1969, Dissertation ETH Zurich, 2003.
DOI https://doi.org/10.3929/ethz-a-004459704

5 Previous reports

Schwarz, G. F., Klingelé, E. E., Rybach, L.: Aeroradiometrische Messungen in der Umgebung der schweizerischen Kernanlagen. Bericht für das Jahr 1989 zuhanden der Hauptabteilung für die Sicherheit der Kernanlagen (HSK). Interner Bericht, Institut für Geophysik, ETH Zürich, 1990.

Schwarz, G. F., Klingelé, E. E., Rybach, L.: Aeroradiometrische Messungen in der Umgebung der schweizerischen Kernanlagen. Bericht für das Jahr 1990 zuhanden der Hauptabteilung für die Sicherheit der Kernanlagen (HSK). Interner Bericht, Institut für Geophysik, ETH Zürich, 1991.

Schwarz, G. F., Klingelé, E. E., Rybach, L.: Aeroradiometrische Messungen in der Umgebung der schweizerischen Kernanlagen. Bericht für das Jahr 1991 zuhanden der Hauptabteilung für die Sicherheit der Kernanlagen (HSK). Interner Bericht, Institut für Geophysik, ETH Zürich, 1992.

Schwarz, G. F., Klingelé, E. E., Rybach, L.: Aeroradiometrische Messungen in der Umgebung der schweizerischen Kernanlagen. Bericht für das Jahr 1992 zuhanden der Hauptabteilung für die Sicherheit der Kernanlagen (HSK). Interner Bericht, Institut für Geophysik, ETH Zürich, 1993.

Schwarz, G. F., Klingelé, E. E., Rybach, L.: Aeroradiometrische Messungen in der Umgebung der schweizerischen Kernanlagen. Bericht für das Jahr 1993 zuhanden der Hauptabteilung für die Sicherheit der Kernanlagen (HSK). Interner Bericht, Institut für Geophysik, ETH Zürich, 1994.

Schwarz, G. F., Rybach, L.: Aeroradiometrische Messungen im Rahmen der Übung ARM94. Bericht für das Jahr 1994 zuhanden der Fachgruppe Aeroradiometrie (FAR). Interner Bericht, Institut für Geophysik, ETH Zürich, 1995.

Schwarz, G. F., Rybach, L.: Aeroradiometrische Messungen im Rahmen der Übung ARM95. Bericht für das Jahr 1995 zuhanden der Fachgruppe Aeroradiometrie (FAR). Interner Bericht, Institut für Geophysik, ETH Zürich, 1996.

Schwarz, G. F., Rybach, L., Bärlocher, C.: Aeroradiometrische Messungen im Rahmen der Übung ARM96. Bericht für das Jahr 1996 zuhanden der Fachgruppe Aeroradiometrie (FAR). Interner Bericht, Institut für Geophysik, ETH Zürich, 1997.

Bucher, B., Rybach, L., Schwarz, G., Bärlocher, C.: Aeroradiometrische Messungen im Rahmen der Übung ARM97. Bericht für das Jahr 1997 zuhanden der Fachgruppe Aeroradiometrie (FAR). Interner Bericht, Institut für Geophysik, ETH Zürich, 1998.

Bucher, B., Rybach, L., Schwarz, G., Bärlocher, C.: Aeroradiometrische Messungen im Rahmen der Übung ARM98. Bericht für das Jahr 1998 zuhanden der Fachgruppe Aeroradiometrie (FAR). Interner Bericht, Institut für Geophysik, ETH Zürich, 1999.

Bucher, B., Rybach, L., Schwarz, G., Bärlocher, C.: Aeroradiometrische Messungen im Rahmen der Übung ARM99. Bericht für das Jahr 1999 zuhanden der Fachgruppe Aeroradiometrie (FAR). Interner Bericht, Institut für Geophysik, ETH Zürich, 2000.

Bucher, B., Rybach, L., Schwarz, G., Bärlocher, C.: Aeroradiometrische Messungen im Rahmen der Übung ARM00. Bericht für das Jahr 2000 zuhanden der Fachgruppe Aeroradiometrie (FAR). Interner Bericht, Institut für Geophysik, ETH Zürich, 2001.

Bucher, B., Rybach, L., Schwarz, G., Bärlocher, C.: Aeroradiometrische Messungen im Rahmen der Übung ARM01. Bericht für das Jahr 2001 zuhanden der Fachgruppe Aeroradiometrie (FAR). Interner Bericht, Paul Scherrer Institut, Villigen, Schweiz, 2002.

Bucher, B., Rybach, L., Schwarz, G., Bärlocher, C.: Aeroradiometrische Messungen im Rahmen der Übung ARM02. Bericht für das Jahr 2002 zuhanden der Fachgruppe Aeroradiometrie (FAR). Interner Bericht, Paul Scherrer Institut, Villigen, Schweiz, 2003.

Bucher, B., Rybach, L., Schwarz, G.: Aeroradiometrische Messungen im Rahmen der Übung ARM03. PSI-Bericht 04-14, ISSN 1019-0643, Paul Scherrer Institut, Villigen, Schweiz, 2004.

Bucher, B., Butterweck, G., Rybach, L., Schwarz, G.: Aeroradiometrische Messungen im Rahmen der Übung ARM04. PSI-Bericht 05-10, ISSN 1019-0643, Paul Scherrer Institut, Villigen, Schweiz, 2005.
DOI `https://doi.org/10.55402/psi:41689`

Bucher, B., Butterweck, G., Rybach, L., Schwarz, G.: Aeroradiometrische Messungen im Rahmen der Übung ARM05. PSI-Bericht 06-06, ISSN 1019-0643,Paul Scherrer Institut, Villigen, Schweiz, 2006.
DOI `https://doi.org/10.55402/psi:41685`

Bucher, B., Butterweck, G., Rybach, L., Schwarz, G.: Aeroradiometrische Messungen im Rahmen der Übung ARM06. PSI-Bericht 07-02, ISSN 1019-0643, Paul Scherrer Institut, Villigen, Schweiz, 2007.
DOI `https://doi.org/10.55402/psi:41681`

Bucher, B., Guillot, L., Strobl, C., Butterweck, G., Gutierrez, S., Thomas, M., Hohmann, C., Krol, I., Rybach, L., Schwarz, G.: International Intercomparison Exercise of Airborne Gammaspectrometric Systems of Germany, France and Switzerland in the Framework of the Swiss Exercise ARM07. PSI-Bericht Nr. 09-07, ISSN 1019-0643, Paul Scherrer Institut, Villigen, Schweiz, 2009.
DOI `https://doi.org/10.55402/psi:35550`

Bucher, B., Butterweck, G., Rybach, L., Schwarz, G.: Aeroradiometrische Messungen im Rahmen der Übung ARM08. PSI-Bericht Nr. 09-02, ISSN 1019-0643, Paul Scherrer Institut, Villigen, Schweiz, 2009.
DOI `https://doi.org/10.55402/psi:35550`

Bucher, B., Butterweck, G., Rybach, L., Schwarz, G., Strobl, C.: Aeroradiometrische Messungen im Rahmen der Übung ARM09. PSI-Bericht Nr. 10-01, ISSN 1019-0643, Paul Scherrer Institut, Villigen, Schweiz, 2010.
DOI `https://doi.org/10.55402/psi:35541`

Bucher, B., Butterweck, G., Rybach, L., Schwarz, G., Mayer, S.: Aeroradiometrische Messungen im Rahmen der Übung ARM10. PSI-Bericht Nr. 11-02, ISSN 1019-0643, Paul Scherrer Institut, Villigen, Schweiz, 2011.
DOI `https://doi.org/10.55402/psi:35201`

Bucher, B., Butterweck, G., Rybach, L., Schwarz, G., Mayer, S.: Aeroradiometric Measurements in the Framework of the Swiss Exercise ARM11. PSI-Report No. 12-04, ISSN 1019-0643, Paul Scherrer Institut, Villigen, Switzerland, 2012.
DOI `https://doi.org/10.55402/psi:35137`

Butterweck, G., Bucher, B., Rybach, L., Schwarz, G., Hödlmoser, H., Mayer, S., Danzi, C. Scharding, G.: Aeroradiometric Measurements in the Framework of the Swiss Exercise ARM12. PSI-Report No. 13-01, ISSN 1019-0643, Paul Scherrer Institut, Villigen, Switzerland, 2013.
DOI `https://doi.org/10.55402/psi:35134`

Butterweck, G., Bucher, B., Rybach, L., Schwarz, G., Hohmann, E., Mayer, S., Danzi, C. Scharding, G.: Aeroradiometric Measurements in the Framework of the Swiss Exercise ARM13. PSI-Report No. 15-01, ISSN 1019-0643, Paul Scherrer Institut, Villigen, Switzerland, 2015.
DOI `https://doi.org/10.55402/psi:35064`

Butterweck, G., Bucher, B., Rybach, L., Schwarz, G., Hohmann, E., Mayer, S., Danzi, C. Scharding, G.: Aeroradiometric Measurements in the Framework of the Swiss Exercises ARM14 and FTX14. PSI-Report No. 15-02, ISSN 1019-0643, Paul Scherrer Institut, Villigen, Switzerland, 2015.
DOI `https://doi.org/10.55402/psi:35062`

Butterweck, G., Bucher, B., Rybach, L., Schwarz, G., Hofstetter-Boillat, B., Hohmann, E., Mayer, S., Danzi, C. Scharding, G.: Aeroradiometric Measurements in the Framework of the Swiss Exercises ARM15, GNU15 and the International Exercise AGC15. PSI-Report No. 15-04, ISSN 1019-0643, Paul Scherrer Institut, Villigen, Switzerland, 2015.
DOI `https://doi.org/10.55402/psi:35047`

Butterweck, G., Bucher, B., Rybach, L., Poretti, C., Maillard, S., Schwarz, G., Hofstetter-Boillat, B., Hohmann, E., Mayer, S., Scharding, G.: Aeroradiometric Measurements in the Framework of the Swiss Exercises ARM16 and LAURA. PSI-Report No. 17-01, ISSN 1019-0643, Paul Scherrer Institut, Villigen, Switzerland, 2017.
DOI `https://doi.org/10.55402/psi:34988`

Butterweck, G., Bucher, B., Gryc, L., Debayle, C., Strobl, C., Maillard, S., Thomas, M., Helbig, A., Krol, I., Chuzel, S., Couvez, C., Ohera, M., Rybach, L., Poretti, C., Hofstetter-Boillat, B., Mayer, S., Scharding, G.: International Intercomparison Exercise of Airborne Gamma-Spectrometric Systems of the Czech Republic, France, Germany and Switzerland in the Framework of the Swiss Exercise ARM17. PSI-Report No. 18-04, ISSN 1019-0643, Paul Scherrer Institut, Villigen, Switzerland, 2018.
DOI `https://doi.org/10.55402/psi:34959`,

Butterweck, G., Bucher, B., Rybach, L., Poretti, C., Maillard, S., Schindler, M., Hofstetter-Boillat, B., Mayer, S., Scharding, G.: Aeroradiometric Measurements in the Framework of the Swiss Exercises ARM18 and the International Exercise CONTEX 2018. PSI-Report No. 19-01, ISSN 1019-0643, Paul Scherrer Institut, Villigen, Switzerland, 2019.
DOI `https://doi.org/10.55402/psi:34957`,

Butterweck, G., Bucher, B., Rybach, L., Poretti, C., Maillard, S., Schindler, M., Hofstetter-Boillat, B., Mayer, S., Scharding, G.: Aeroradiometric Measurements in the Framework of the Swiss Exercise ARM19. PSI-Report No. 20-01, ISSN 1019-0643, Paul Scherrer Institut, Villigen, Switzerland, 2020.
DOI `https://doi.org/10.55402/psi:44919`

Butterweck, G., Bucher, B., Breitenmoser, D., Rybach, L., Poretti, C., Maillard, S., Kasprzak, M., Ferreri, G., Gurtner, A., Astner, M., Hauenstein, F., Straub, M., Bucher, M., Harm, C., Scharding, G., Mayer, S.: Aeroradiometric Measurements in the Framework of the Swiss Exercise ARM20. PSI-Report No. 21-01, ISSN 1019-0643, Paul Scherrer Institut, Villigen, Switzerland, 2021.
DOI https://doi.org/10.13140/RG.2.2.15326.51526

Butterweck, G., Bucher, B., Breitenmoser, D., Rybach, L., Poretti, C., Maillard, S., Hess, A., Kasprzak, M., Scharding, G., Mayer, S.: Aeroradiometric Measurements in the Framework of the Swiss Exercise ARM21. PSI-Report No. 22-02, ISSN 1019-0643, Paul Scherrer Institut, Villigen, Switzerland, 2022.
DOI https://doi.org/10.55402/psi:44921

The reports since 1994 can be found and downloaded from the FAR website https://far.ensi.ch.

6 Evaluation parameters

The parameters used for data evaluation are stored in the header section of each generated ERS 2.0 file. The header sections used in the current exercise are listed below.

6.1 Detector RLL001

These evaluation parameters were used for the evaluation of exercise part ARM22c with detector RLL001.

```
V 2.0
HSW AGS_CH_V0.0
/* Parameters used for data evaluation---------------------------------------------------------------------
/* No data value;MND -999
/* Energy calibration;ISE0 0;ISE1 3;ISE2 0
/* Energy windows------------------------------------------------------------------------------------------
ISW Total;ISWE1_Total 401;ISWE2_Total 2997;ISWB_Total 139.7;ISWC_Total 6.02;ISWT_Total 0.006;ISWRA_Total 0;ISWRB_Total 0
ISW K-40;ISWE1_K-40 1369;ISWE2_K-40 1558;ISWB_K-40 8.6;ISWC_K-40 0.35;ISWT_K-40 0.008;ISWRA_K-40 0;ISWRB_K-40 0
ISW U-238;ISWE1_U-238 1664;ISWE2_U-238 1853;ISWB_U-238 6.7;ISWC_U-238 0.26;ISWT_U-238 0.0055;ISWRA_U-238 0;ISWRB_U-238 0
ISW Th-232;ISWE1_Th-232 2407;ISWE2_Th-232 2797;ISWB_Th-232 0.3;ISWC_Th-232 0.30;ISWT_Th-232 0.006;ISWRA_Th-232 0;ISWRB_Th-232 0
ISW Cs-137;ISWE1_Cs-137 600;ISWE2_Cs-137 720;ISWB_Cs-137 21.6;ISWC_Cs-137 0.70;ISWT_Cs-137 0.01;ISWRA_Cs-137 0;ISWRB_Cs-137 0
ISW Co-60;ISWE1_Co-60 1100;ISWE2_Co-60 1400;ISWB_Co-60 13.1;ISWC_Co-60 0.76;ISWT_Co-60 0.008;ISWRA_Co-60 0;ISWRB_Co-60 0
ISW MMGC1;ISWE1_MMGC1 400;ISWE2_MMGC1 1400;ISWB_MMGC1 0;ISWC_MMGC1 0;ISWT_MMGC1 0.006;ISWRA_MMGC1 0;ISWRB_MMGC1 0
ISW MMGC2;ISWE1_MMGC2 1400;ISWE2_MMGC2 2997;ISWB_MMGC2 0;ISWC_MMGC2 0;ISWT_MMGC2 0.0065;ISWRA_MMGC2 0;ISWRB_MMGC2 0
ISW LOW;ISWE1_LOW 100;ISWE2_LOW 400;ISWB_LOW 0;ISWC_LOW 0;ISWT_LOW 0.02;ISWRA_LOW 0;ISWRB_LOW 0
ISW MID;ISWE1_MID 720;ISWE2_MID 2997;ISWB_MID 0;ISWC_MID 0;ISWT_MID 0.015;ISWRA_MID 0;ISWRB_MID 0
ISW SDI;ISWE1_SDI 240;ISWE2_SDI 2997;ISWB_SDI 95.6;ISWC_SDI 4.49;ISWT_SDI 0.0053;ISWRA_SDI 0;ISWRB_SDI 0
/* Stripping factors---------------------------------------------------------------------------------------
ISWS_U-238_K-40 0.931
ISWS_Th-232_K-40 0.478
ISWS_Co-60_K-40 0.067
ISWS_Th-232_U-238 0.362
ISWS_U-238_Th-232 0.049
ISWS_K-40_Cs-137 0.450
```

```
ISWS_U-238_Cs-137 3.161
ISWS_Th-232_Cs-137 1.654
ISWS_Co-60_Cs-137 0.154
ISWS_K-40_Co-60 0.758
ISWS_U-238_Co-60 2.370
ISWS_Th-232_Co-60 0.684
/* Conversion factors-------------------------------------------------------------------------------------
ISWA_AW_K-40 5.58
ISWA_AW_U-238 3.57
ISWA_AW_Th-232 1.22
ISWA_AW_Cs-137 1.02
ISWA_AA_Cs-137 201
ISWA_AP_Cs-137 2511000
ISWA_AP_Co-60 1505000
ISD_SDI 5.65E-08
ISWD_K-40 0.000289
ISWD_U-238 0.00197
ISWD_Th-232 0.000971
ISWD_Cs-137 0.000191
/*
/* Corrections-------------------------------------------------------------------------------------
/* Definition of additional Identifiers for corrected altitude and ground clearance,
/* an indicator for a new flight and the factor for calculation of synthetic cosmic counts
/* Corrected altitude im m;DEFINE&PZ_korr
/* Corrected ground clearance in m; DEFINE&PH_korr
/* Switch for data composed of several flights;DEFINE&New_Flight
/* Factor for calculation of synthetic cosmic counts;DEFINE&Factor_COS
/* Factor for the calculation of synthetic cosmic counts;&Factor_COS 14.35
/* Topographic correction;MTC Y
/* Radon correction;MRC N
```

6.2 Detector RLL003

These evaluation parameters were used for the evaluation of exercise part ARM22m with detector RLL003.

```
V 2.0
HSW AGS_CH_V0.0
/* Parameters used for data evaluation---------------------------------------------------------------------
/* No data value;MND -999
/* Energy calibration;ISE0 0;ISE1 3;ISE2 0
/* Energy windows------------------------------------------------------------------------------------------
ISW Total;ISWE1_Total 401;ISWE2_Total 2997;ISWB_Total 105.1;ISWC_Total 6.02;ISWT_Total 0.006;ISWRA_Total 0;ISWRB_Total 0
ISW K-40;ISWE1_K-40 1369;ISWE2_K-40 1558;ISWB_K-40 7.0;ISWC_K-40 0.35;ISWT_K-40 0.008;ISWRA_K-40 0;ISWRB_K-40 0
ISW U-238;ISWE1_U-238 1664;ISWE2_U-238 1853;ISWB_U-238 5.2;ISWC_U-238 0.26;ISWT_U-238 0.0055;ISWRA_U-238 0;ISWRB_U-238 0
ISW Th-232;ISWE1_Th-232 2407;ISWE2_Th-232 2797;ISWB_Th-232 -0.7;ISWC_Th-232 0.30;ISWT_Th-232 0.006;ISWRA_Th-232 0;ISWRB_Th-232 0
ISW Cs-137;ISWE1_Cs-137 600;ISWE2_Cs-137 720;ISWB_Cs-137 17.4;ISWC_Cs-137 0.70;ISWT_Cs-137 0.01;ISWRA_Cs-137 0;ISWRB_Cs-137 0
ISW Co-60;ISWE1_Co-60 1100;ISWE2_Co-60 1400;ISWB_Co-60 9.0;ISWC_Co-60 0.76;ISWT_Co-60 0.008;ISWRA_Co-60 0;ISWRB_Co-60 0
ISW MMGC1;ISWE1_MMGC1 400;ISWE2_MMGC1 1400;ISWB_MMGC1 0;ISWC_MMGC1 0;ISWT_MMGC1 0.006;ISWRA_MMGC1 0;ISWRB_MMGC1 0
ISW MMGC2;ISWE1_MMGC2 1400;ISWE2_MMGC2 2997;ISWB_MMGC2 0;ISWC_MMGC2 0;ISWT_MMGC2 0.0065;ISWRA_MMGC2 0;ISWRB_MMGC2 0
ISW LOW;ISWE1_LOW 100;ISWE2_LOW 400;ISWB_LOW 0;ISWC_LOW 0;ISWT_LOW 0.02;ISWRA_LOW 0;ISWRB_LOW 0
ISW MID;ISWE1_MID 720;ISWE2_MID 2997;ISWB_MID 0;ISWC_MID 0;ISWT_MID 0.015;ISWRA_MID 0;ISWRB_MID 0
ISW SDI;ISWE1_SDI 240;ISWE2_SDI 2997;ISWB_SDI 69.6;ISWC_SDI 4.49;ISWT_SDI 0.0053;ISWRA_SDI 0;ISWRB_SDI 0
/* Stripping factors---------------------------------------------------------------------------------------
ISWS_U-238_K-40 0.980
ISWS_Th-232_K-40 0.503
ISWS_Co-60_K-40 0.052
ISWS_Th-232_U-238 0.344
ISWS_U-238_Th-232 0.061
ISWS_K-40_Cs-137 0.476
ISWS_U-238_Cs-137 3.184
ISWS_Th-232_Cs-137 1.639
ISWS_Co-60_Cs-137 0.133
ISWS_K-40_Co-60 0.788
ISWS_U-238_Co-60 2.320
ISWS_Th-232_Co-60 0.629
```

```
/* Conversion factors-------------------------------------------------------------------------------------
ISWA_AW_K-40 5.58
ISWA_AW_U-238 3.57
ISWA_AW_Th-232 1.22
ISWA_AW_Cs-137 1.02
ISWA_AA_Cs-137 201
ISWA_AP_Cs-137 2511000
ISWA_AP_Co-60 1505000
ISD_SDI 5.65E-08
ISWD_K-40 0.000289
ISWD_U-238 0.00197
ISWD_Th-232 0.000971
ISWD_Cs-137 0.000191
/* Corrections-------------------------------------------------------------------------------------
/* Definition of additional Identifiers for corrected altitude and ground clearance,
/* an indicator for a new flight and the factor for calculation of synthetic cosmic counts
/* Corrected altitude im m;DEFINE&PZ_korr
/* Corrected ground clearance in m; DEFINE&PH_korr
/* Switch for data composed of several flights;DEFINE&New_Flight
/* Factor for calculation of synthetic cosmic counts;DEFINE&Factor_COS
/* Factor for the calculation of synthetic cosmic counts;&Factor_COS 14.35
/* Topographic correction;MTC Y
/* Radon correction;MRC N
```

Paul Scherrer Institut :: Forschungsstrasse 111 :: 5232 Villigen PSI :: Switzerland :: Tel. +41 56 310 21 11 :: www.psi.ch